UNIVERSITY OF PORTSMOUTH

Doctoral Thesis

Numerical Modelling and Material Assessment in Thermal Energy Storage Systems

School of Mechanical and Design Engineering (SMDE)

Author: Law Torres Sevilla
Supervisor: Jovana Radulovic

This dissertation is submitted for the degree of
Doctor of Philosophy

University of Portsmouth March 2021

Copyright

Acknowledgements

I would like to take a moment to thank all the people that made this possible. My deepest gratitude to my supervisor, Jovana Radulovic, for encouraging me through this long and difficult journey. You have been my biggest support and inspiration, and I cannot thank you enough for all your help. A huge thank you to my parents (David and Yolanda), my incredible friends and flatmates (Manos, James and Rachel) and my best friend and partner (Sara). Thank you all for your reassurance and kind words.

Table of Contents

I. Introduction

The world is embarking into a fossil fuel free environment in which the predominant sources will be renewable and sustainable energies. Since renewable energy is usually associated with their intermittent nature, it is important to always have a backup source of energy in times of need and demand. For this, energy storage is an essential component of any renewable energy system. In times of high demand, where the sun is not shining and the wind is not blowing, the existence of a backup energy supply with easy and fast access is necessary. Thus, Thermal Energy Storage (TES) is one of the proposed solutions to aid in this mismatch in consumption and demand caused by the nature of the green technologies (Ali et al., 2020).

TES can be an accompaniment of systems such as a Joule-Brayton cycle, Rankine cycle, a heat pump or even solar collectors. Other applications include systems which focus on heat waste recovery, steam generation for turbines, domestic uses and household heating. Energy from TES can be stored daily, monthly or seasonally. This determines the type and size of the system and whether it is a smaller scale domestic or large scale industrial project (Fang et al., 2017). In all cases, however, its main potential to serve as a tool that saves energy and mitigates climate change, keeping CO_2 emissions minimized, and helping countries meet their established environmental goals. Low grade TES is in increasing importance and therefore remains the focus of this thesis.

1.1 Initial Aim and Objectives

The aim of this research project is to study the behaviour and effectiveness of different materials as both sensible and latent heat energy storage mediums in a single packed bed tank for the charging scenario only.

Following the literature review, the gap in the knowledge associated with this study's topic was evident. This has helped form the following research questions:

- How influential are specific thermal properties on heat absorption and heating dynamics?
- What is the most effective combination of thermal parameters for a low grade test application?
- Can the heating dynamics be accurately captured by a mathematical expression?

The general framework includes the following:

- Study the background research and science behind thermal energy
- Fulfil an extensive literature research on system designs and materials
- Select system type and design

- Construct and test the model using software, solving it numerically
- Analyse different types of materials based on the values typically reported in literature
- Evaluate the two outputs: temperature and heat absorption

1.2 Thesis Structure

The structure followed by this thesis is presented below:

Table 1.1: Thesis structure with its corresponding chapter, title, and summary of the content

Chapter	Title	Content
2	Theoretical Background	Explains the science behind thermal energy storage. This includes energy laws and equations, heat transfer methods (conduction, convection, radiation), fluid flow and behaviour, fluid and thermal boundary layers and TES types (sensible heat, latent heat) with material examples.
3	Literature Review	Publications by authors in the field are analysed and evaluated. It was conducted to investigate design types, commonly reported materials, applications and modelling approaches. From here, the research gap is found and redacted.
4	Methodology	This study's system is determined and the research methods are established. The initial modelling for sensible heat, further modelling with varied designs and latent heat, material construction and model validations are found. Assumptions, boundaries and any software used are all detailed.
5	Sensible Heat Results	Presents the sensible heat study findings. Eight sensible heat materials were studied and analysed. Heat absorption and charging temperature is recorded in three positions along the storage tank. Three different tank designs were evaluated and the effect of three inlet velocities was studied.
6	Phase Changing Materials (PCM) Results	Presents the phase changing materials study findings. Three latent heat materials were analysed. These were evaluated based on two different inlet designs, three positions along the tank and three different inlet velocities.
7	Material Construction Results	Presents the material construction results. Twenty eight user-defined materials were tested for heat absorbed per sphere and charging temperature as outputs. Regression analysis was used and equations that linked thermal parameters to the outputs were found.
8	Conclusions	Offers conclusions and contributions to literature. The summary of all the thesis' work is enumerated into comprehensive and effective bullet points. Furthermore, the future work is listed.

1.3 References for this section

Ali S., Deshmukh S.P. (2020) An overview: Applications of thermal energy storage using phase change materials. Materials today: preceedings, 26, 1231-1237. doi: 10.1016/j.matpr.2020.02.247

Fang, G., Lin, Y., & Alva, G. (2017). An overview of thermal energy storage systems. *Energy, 144*, 341-378. doi: 10.1016/j.energy.2017.12.037

II. Theoretical Background

2.1 Thermal Energy Storage (TES)

Thermal Energy Storage (TES) is a technology that can be used for storing energy for a defined period of time. This time period, depending on the system and the requirements can be daily, weekly, monthly or even seasonal.

Since ancient times, humans have been using thermal energy methods in applications such as, for example, harvesting ice for cooling and preserving food (Dinçer & Rosen, 2011). Nowadays, TES can be combined with renewable energy collection to become a powerful tool and solve the many intermittency issues that, for example, wind and solar energies face. However, they are not limited to renewables and are found in other applications such as air conditioning, indoor central heating, domestic or industrial water heating, heat waste recovery, refrigeration and more. Furthermore, it can contribute to settling any problems of high energy demand where peak shaving and load levelling issues arise.

2.2 Energy Conservation

The law of conservation of energy states that energy cannot be created or destroyed, rather converted into another form. Applied to a TES system, the energy conservation equation includes the heat sources and the heat accumulation:

Equation 2.1: $Energy\ out\ =\ Energy\ in\ +\ Heat\ Source\ -\ Stored\ Heat$

$$E_{out}\ =\ E_{in}\ +\ E_{source}\ -\ E_{stored}$$

The first law of thermodynamics is a variation of Equation 2.1, which applies to a closed system (fixed mass) or an open system (control volume) (Dinçer & Rosen, 2011).

Equation 2.2: $\Delta U\ =\ \Delta Q\ -\ \Delta W$

Where "*U*" is the internal energy of the system, "*Q*" is the amount of heat supplied to the system and "*W*" is the amount of work done by the system. Excluding any internal sources, the energy stored is the net difference between energy in and out. In TES, the net work exchange is normally zero, so the stored heat from Equation 2.1 is equal to ΔU. In this context, since ΔW = 0, ΔQ is the difference in the heat applied (energy in – energy out) in Equation 2.1. In order to calculate the energy stored in a TES system or the heat losses once the system reaches the desired temperature, more information about the heat transfer modes is needed.

2.3 Heat Transfer Modes

Heat transfer occurs in all bodies so long as there is a temperature difference. There must be an ideal isothermal system in order for the flow of heat to stop. Heat always flows from the hot body towards the cold one until thermal equilibrium or saturation are reached and heat transfer is no longer possible (Lienhard-IV & Lienhard-V, 2017).

In A TES system heat is transferred in three different modes: conduction, convection and radiation.

2.3.1 Conduction

Conduction is the transfer of heat between bodies by direct contact in rest, as the heat flows within and through the body itself. The bodies which are transferring heat do not flow and or mix whilst the transfer occurs (Levenspiel, 1984). The conduction happens at the microscale, where collisions of particles, molecules and electrons are what change the internal energy which is then transferred in the form of heat.

An example of a simple one dimensional (1D) conduction heat transfer in a rod is shown in Fig 2.1

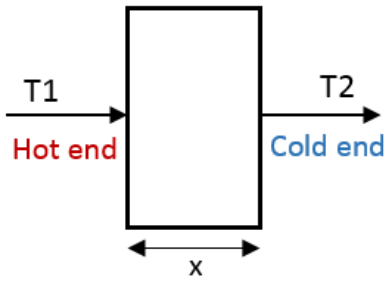

Figure 2.1: Example of simple conduction in 1D

If the temperatures T1 and T2 at the ends are unchanging, the heat transfer is a linear gradient (as the example is 1D). This situation is said to be steady-state conduction. Opposite to this, the temperature profile of each end can change in time whilst the heat transfer is happening and this is denoted transient conduction.

2.3.1.1 Steady-state Conduction

As cited earlier, steady-state occurs when the temperatures at the hot and cold ends of the body are fixed, there are no other heat sources, and the environmental temperature is not considered as an external factor (for example the system could be said to be perfectly insulated). Once the

equilibrium time is reached, where the heat transfer from point A to B finishes, the temperature of the body is either the same at all points in space or does not change any further due to saturation. In this scenario, the amount of heat absorbed and the amount of heat expelled by the system are equal (Ozisik, 1993).

In steady-state conduction, the relationship between the temperatures in space is expressed by "Fourier's Law".

2.3.1.2 Fourier's Law

The law of conduction was developed by the French mathematician and physicist Jean-Baptiste Joseph Fourier. The equation is known as Fourier's Law:

Equation 2.3: $$\dot{Q} = -k\left[\frac{dT}{dx}e_x + \frac{dT}{dy}e_y + \frac{dT}{dz}e_z\right] = -k \cdot \nabla T$$

Equation 2.4: $$\dot{Q} = -k \cdot dT/dx$$

Equation 2.3 is the original equation which is in vector form, taking into account area and direction. Equation 2.4 is the simplified version which only considers a one dimensional space (Taler & Duda, 2006). Each parameter is defined further in the following Table 2.2:

Table 2.2: Definitions of the parameters found in Equations 2.2 and 2.3 (Taler & Duda, 2006)

Symbol	Definition	Units
$\dot{Q}$	Heat flux	W/ m^2
k	Thermal conductivity	W/m · K
∇	Hamiltonian vectorial operator	m^{-1}
T	Temperature	°C or K
x	Distance	m

The heat flux is always perpendicular to the direction of heat transfer and proportional to the temperature gradient. The negative sign at the beginning of the equation represents the heat flowing from a higher temperature to a lower one. The thermal conductivity is a tensor and a property of the material. Therefore, it varies depending on the element, direction and temperature of the transfer. The highest thermal conductivity values are usually found in metals, whereas the lowest are in gases and vapours (Ozisik, 1993).

Taking the example of a 1D rod where the temperature at the ends is fixed is analysed, if the thermal conductivity is constant, the heat flux decreases when the distance between the ends

increases. However, if there is a fixed distance and conduction coefficient, the larger the temperature difference, the higher the heat flux. And vice versa.

Figure 2.2 is provided below for graphical representation of the rod example and to show the relationship between the parameters:

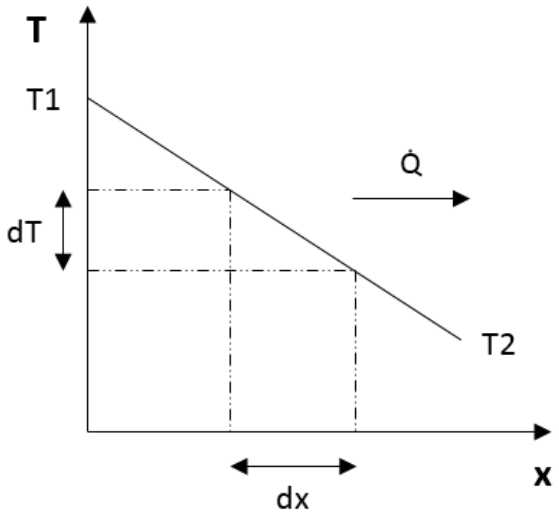

Figure 2.2: Graph demonstrating the linear temperature profile of simple conduction in 1D

2.3.1.3 Heat Diffusion

The thermal diffusivity is a property unique to conduction and specific to each material. Diffusivity expresses the ability a substance has to transmit heat and the larger the thermal diffusivity, the greater the rate of change in temperature. Materials which have a low thermal diffusivity are good for TES (Rolle, 2014). The thermal diffusivity formula (Equation 2.5) shows that α (thermal diffusivity) is a factor of ρ (density) and c_p (specific heat capacity). The heat equation (Equation 2.6) expresses temperature as a partial derivative over time:

Equation 2.5: $\alpha = k / \rho \cdot c_p$

Equation 2.6: $\partial T / \partial t = \alpha \cdot \nabla^2 \cdot T$

Density and specific heat capacity are properties unique to the material. Both of these change with temperature (Ozisik, 1993). Combining both equations forms Equation 2.7:

Equation 2.7: $\partial T / \partial t = k / \rho \cdot c_p \cdot \nabla^2 \cdot T$

Equation 2.7 is then combined with Fourier's Law (Equation 2.4) and the energy conservation equation (Equation 2.1) arranged for heat transfer, where the units are W/m^2 as it expresses the rate of energy by area. These craft the heat diffusion equation:

Equation 2.8: $\rho \cdot c_p \cdot (\partial T/\partial t) = k\,(\partial^2 T/\partial x^2) + \dot{Q}_{source}$

Equation 2.8 allows the heat source to be calculated analytically for a one dimensional system only.

Figure 2.3 shows correlation between the thermal conductivity and the thermal diffusivity properties for various material groups:

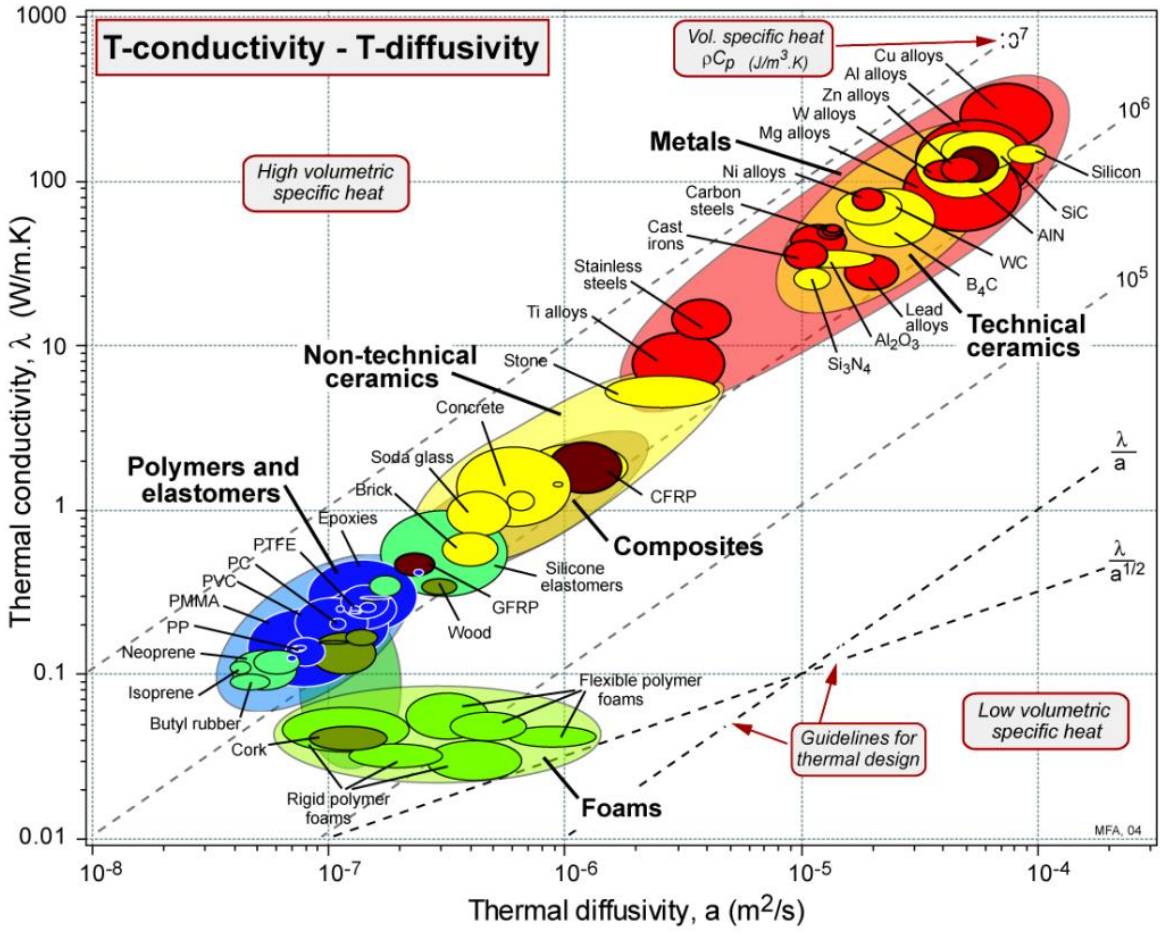

Figure 2.3: Thermal conductivity VS thermal diffusivity of certain material groups (GrantaDesign, 2010)

Fourier's Law and heat diffusion only work for steady-state conduction and should therefore not be used in a transient conduction.

2.3.1.4 Transient Conduction

During transient conduction, the temperature differences which lead the conduction are changing in time too. This is due to a new hot or cold source within the system or a change in the environment. The system oscillates towards equilibrium and once again the heat in equals the heat out. Since it is a much more complicated structure and especially if the geometry and temperature gradient of the object are complex, a numerical approach is necessary (Incropera, Dewitt, Bergman, & Lavine, 2013). Nevertheless, for specific situations, an analytical approach named the lump capacitance method is used.

2.3.1.5 Lump Capacitance Method

The system is modelled so that a body is submerged in an instant into a fluid at a different temperature. This method is applied under two assumptions. Firstly, the system's heat conduction transfer is outstanding and therefore there exists no temperature gradient, rather, the temperature is uniform. Secondly, the system is very small and the volume can be considered negligible, therefore considering that it is a function of temperature and time solely, eluding the space component. This provides a non-existent temperature gradient, meaning an unreal scenario of infinite thermal conductivity, and favouring a uniform temperature distribution (Rolle, 2014).

Comparing the heat transfer at the boundary, which is usually convection, to the conductive heat transfer is a necessary step as it provides a dimensionless parameter named the Biot number which measures the temperature change in the body relative to the temperature of the fluid.

Equation 2.9: $Bi = hA \cdot \Delta T \cdot L_c / kA \cdot \Delta T = hL_c / k$

Where *Bi* is the Biot number, *h* is the convection coefficient, *A* is the area, *ΔT* is the change in temperature, L_c is the characteristic length and *k* is the conduction coefficient. When the Biot number is higher than a 0.1 value, the lump capacitance method cannot be used in that particular system as a uniform temperature cannot be assumed (Incropera et al., 2013).

Once the Biot value is settled, the transient temperatures are determined using an equation derived from the energy balance. Equation 2.12 relates the rate of heat lost at the body's surface in contact with the fluid and the rate of internal energy change inside the body (Rolle, 2014). Equations 2.10 and 2.11 show the derivation:

Equation 2.10: $\dot{Q}_{boundary} = dE/dt = \rho Vcp \cdot dT/dt$

Equation 2.11: $dT/dt = \rho V c_p \cdot hAs\ (T - T_\infty)$

Equation 2.12: $\dot{Q}_{boundary} = \rho V c_p \cdot hAs\ (T - T_\infty)$

If T_∞ is constant, for simplification theta is equivalent to the temperature difference:

Equation 2.13: $\theta \equiv T - T_\infty$

Equation 2.14: $(\rho V cp / hAs) \cdot (d\theta/dt) = -\theta$

The integration of Equation 2.14 between initial time (zero) and a desired time allows the temperature "T" to be found. Vice versa, if the temperature is unknow, it can be input and found using the formula (Incropera et al., 2013).

2.3.2 Convection

Convection is heat transfer between a fluid and a stationary surface, alongside other thermal interactions between fluids. The heat transfer is caused by the movement of bulk fluids known as advection and the random motion of fluid molecules known as diffusion (conduction). When the displacement of molecules is in bulk and larger quantities, it is known to be on the macroscopic scale, whereas single molecular movement is microscopic (Rogers & Mayhew, 1992).

There are two types of convective heat transfer: free and forced. When the fluid motion happens naturally due to changes in temperature which affect density and therefore buoyancy, it is free convection. For forced convection, the fluid motion is imposed by external forces such as, for example, a fan. Depending on the type of convection, there is a difference in the convective heat transfer coefficient.

2.3.2.1 Newton's Law of Cooling

The rate of heat transfer during convection can be calculated using Newton's Law of Cooling, expressed as the following equation:

Equation 2.15: $q = hA \cdot \Delta T = hA \cdot (T_s - T_\infty)$

This formula states that the rate of the heat lost or gained by the body is proportional to the temperature difference between the fluid and the surface. On occasion, the temperature of the fluid is the environmental temperature and is therefore denoted with the infinity symbol. If the exchange

happened between a wall surface inside a pipe and the flowing fluid inside, it is denoted as T_f (Rolle, 2014). parameters are shown in the Table 2.3:

Table 2.3: Definitions of the parameters found in Equation 15 (Dinçer & Rosen, 2011)

Symbol	Definition	Units
q	Heat flux	W
h	Convective heat transfer coefficient	$W/m^2 \cdot K$
A	Transfer surface area	m^2
T_s	Surface temperature	°C or K
T_∞	Fluid temperature	°C or K

The temperature value for the surface is assumed to be uniform for the entire transfer area. Equally, the heat transfer coefficient calculated is usually a constant average value, whereas the reality is that both the temperature at the surface and the coefficient change in space and time.

The way the fluid travels over the surface can be illustrated to explain how certain parameters and their profiles change in such close proximity. This is because when a fluid flows over a surface a boundary layer is formed. There are two important boundary layers relevant to convective heat transfer: velocity and thermal.

2.3.2.2 Velocity Boundary Layer

The velocity boundary layer is a thin layer of fluid where in the closest proximity to the surface, the particle velocity of the fluid is approximated to zero due to viscous and compressible forces. The particles then slow down and delay the motion of the adjacent particle layers as they move away. The delay occurs until the velocity reaches its original stream velocity, where the retardation becomes negligible (Incropera et al., 2013). Figure 2.4 below illustrates the velocity boundary layer on a plate or wall:

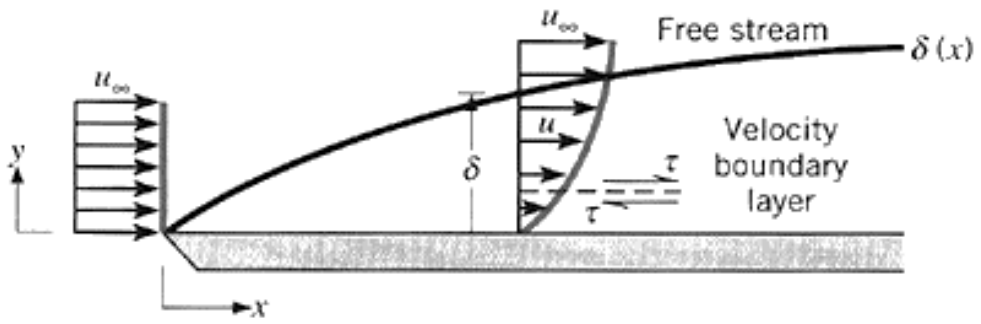

Figure 2.4: Velocity boundary layer development on a flat plate or wall (Incropera et al., 2013)

In this diagram, u_∞ is the free stream velocity. The distance at which the delay ceases is denoted by Equation 2.16:

Equation 2.16: $y = \delta$

Where *y* is the vertical distance from the surface and δ is the boundary layer thickness (both units in metres). The boundary layer thickness is usually defined as the *y* value for which the velocity *u* corresponds to the following:

Equation 2.17: $u = 0.99 \cdot u_\infty$

Inside the boundary layer there is a shear stress acting tangentially towards the surface of the plate or wall. It is greatest towards the boundary and equals zero outside of it. The relationship between the shear stress, velocity and distance is known as Newton's Law of Viscosity:

Equation 2.18: $\tau = \mu\,(du/dy) = \rho\nu\,(du/dy)$

Where τ is the shear stress, μ is the viscosity, ρ is density and ν is kinematic viscosity.

2.3.2.3 Thermal Boundary Layer

The thermal boundary layer develops if there is a difference between the stream and surface temperatures. The particles which are in close contact to the surface, will reach a thermal equilibrium and achieves the same temperature as the surface before the others.

Similar to the velocity boundary, the particles in contact will transfer the heat energy to other adjacent particle layers until the temperature reaches the stream temperature at a certain boundary layer thickness (Equation 2.16). Figure 2.5 illustrates the thermal boundary layer on a plate or wall:

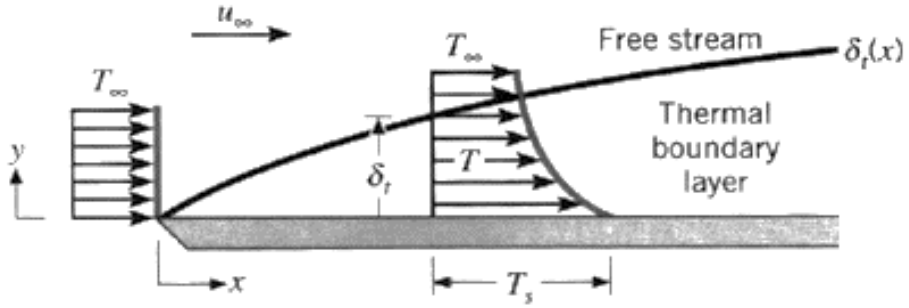

Figure 2.5: Thermal boundary layer development on an isothermal flat plate or wall (Incropera et al., 2013)

In this case, the vertical distance which becomes the boundary layer thickness has a different requirement, seen as Equation 2.19:

Equation 2.19: $[(T_s - T) / (T_s - T_\infty)] = 0.99$

At a distance y = 0, which would be when the fluid is in direct contact with the surface, there is no convection. In fact, the heat transfer method is only conduction and can be expressed as:

Equation 2.20: $\dot{Q}_s = -k_f(\partial T/\partial y)$ *, for y = 0*

Where the subscripts *s* and *f* refer to surface heat flux and conduction coefficient of the fluid, respectively. This equation combined with Newton's Law of Cooling (Equation 2.15) forms Equation 2.21 used to find the convective heat transfer coefficient *h*:

Equation 2.21: $h = \frac{-kf\ (\partial T/\partial y)}{Ts-T\infty}$ *, for y = 0*

Further to this, the fluid flows in two manners along the velocity boundary. One, known as laminar flow, occurs when the fluid flows in layers parallel to the surface where there is no disturbance or chaotic movement between them. The other, known as turbulent flow, takes place when the fluid flows in random patterns as opposed to straight lines, with the layers intermixing and forming many vortices (Rogers & Mayhew, 1992). The fluid flow regime affects greatly both the velocity and thermal boundary layers. This will be further explained in the following division.

2.3.2.4 Laminar and Turbulent Velocity & Thermal Boundary Layers

Laminar flow usually precedes turbulent flow and it is layered and structured. Initially the streamlines are gradients, as the flow at the inlet is not fully developed. Once this stage is reached, the streamlines along which the particles move can be identified easily. Subsequently, there is a transition region where the flow is both laminar and turbulent as the conversion from one to the other is happening. Lastly, the fully turbulent section is reached where all the vortices, irregular behaviour and random eddy motions happen. This region characterises from its three parts: turbulent region, buffer layer and viscous sub-layer.

In the viscous sub-layer the fluid sticks to the surface, allowing the velocity profile to be almost linear. Here the flow is dominated by small molecular movement or diffusion. At the buffer layer, simultaneously diffusion and turbulence are happening, so the start of eddy motion and mixing can be appreciated. Lastly, in the turbulent region the totality of the fluid moves in random turbulent mixing and there are no linear streamlines (Incropera et al., 2013). All these are illustrated in Figure 2.6 below:

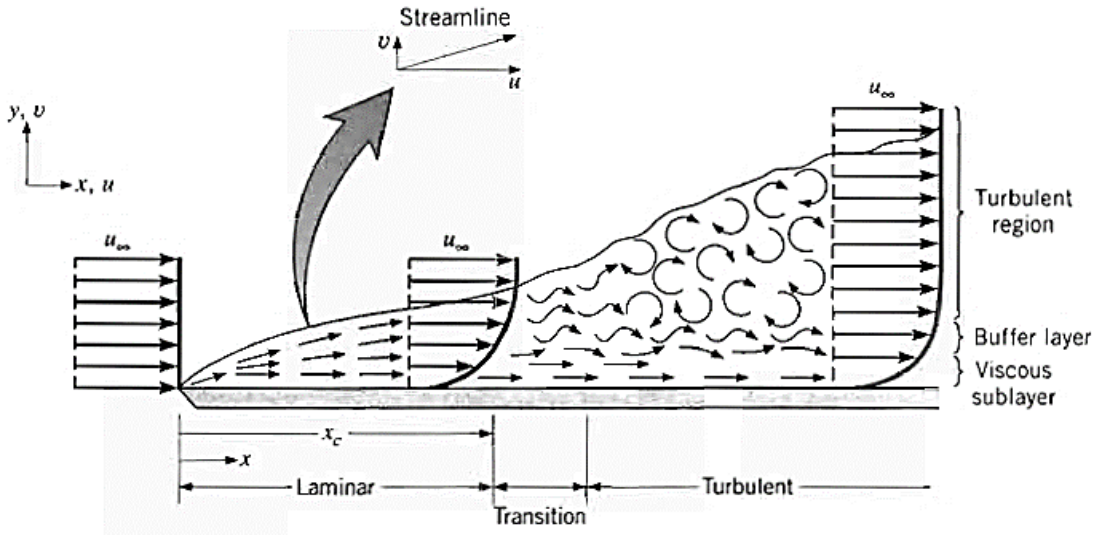

Figure 2.6: Velocity boundary layer development on a flat plate or wall (Incropera et al., 2013)

The primary flow characterisation parameter is the Reynolds number. This dimensionless quantity defines if the fluid is laminar or turbulent. The flow is laminar when the Reynolds number is lower than 2300, transient when it is between 2300 and 4000 and fully turbulent when it is over 4000 (approximately).

Equation 2.22: $Re = (\rho \cdot u_\infty \cdot x)/\mu$

Where *Re* is the Reynolds number, ρ is density, u_∞ is the free stream velocity, *x* is the characteristic length and μ is the viscosity (Incropera et al., 2013).

The thermal boundary layer depends greatly on the velocity boundary layer and its regions since it varies the heat transfer coefficient. The nature and velocity of the fluid flowing affects the heat transfer rate.

In the laminar region, the heat transfer decreases alongside the streamlines with an increasing distance *x*. In the transition region as turbulent mixing is just starting and the fluid carries more energy, the heat transfer coefficient increases greatly and steeply. Nevertheless, once in the fully turbulent region with all the layers intermixing and all the vortices being introduced, the heat transfer carries no conduction and again decreases (Incropera et al., 2013). This is all illustrated in the Figure 2.7 below:

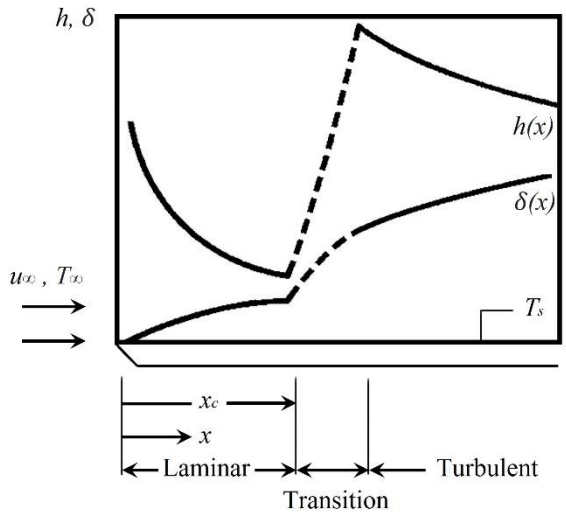

Figure 2.7: Variation of velocity boundary layer thickness and the local heat transfer coefficient for flow over an isothermal plate or wall (Incropera et al., 2013)

The convective heat transfer coefficient *h* is predicted using empirical correlation equations which depend on whether the flow is external or internal and what the geometry of the heat transfer body is.

2.3.2.5 External Convection

External flow is not confined and is assumed to continue without any constraints. These convection correlation equations differ depending on the flow type (free or forced), flow velocity (laminar or turbulent), phase-change (evaporation, condensation or fusion) and flow geometry (parallel, cross-flow or at an angle).

Equations 2.23 to 2.25 are related to forced convection. The main difference between free and forced convection is that the Nusselt number (Nu) will be a factor of the Prandtl number (Pr) and the Reynolds number (Re) for a forced situation. In free convection, the Nusselt number will be a factor of the Prandtl number and the Grashof number (Gr). All these are dimensionless parameters.

The Nusselt number conveys the ratio between the conductive thermal resistance and the convective thermal resistance. The Prandtl number is ratio of thermal diffusivity (Equation 2.5) and momentum diffusivity (seen below as Equation 2.23).

Equation 2.23: $\nu = \mu / \rho$

Equation 2.24: $Pr = \mu c_p / k$

Equation 2.25: $Nu = hL / k$

For most external flow correlation equations, the fluid properties must be taken at the film temperature (T_f). The film temperature is the average temperature between the two heat transfer bodies:

Equation 2.26: $T_f = (T_s + T_\infty)/2$

For other correlation equations, the fluid properties must be taken at the average fluid temperature, represented as $\overline{T}$.

Equation 2.27: $\overline{T} = (T_{inlet} + T_{outlet})/2$

Finding the average Nusselt number and the average value of the convective heat transfer coefficient is done using correlation equations. The table below shows some of the most common type of correlation equations used for certain geometries and fluid flows. The geometries that have an asterisk next to them show that these are using the average fluid temperature for the properties, rather than the film temperature.

Table 2.4: Examples of external correlation equations with its respective restrictions. C_1, C_2, m, j_h and j_m values can be found in the book 'Principles of Heat and Mass Transfer' (Incropera et al., 2013)

Geometry	Flow Type - Re Number	Flow Conditions	Average Nu Number	Restrictions	Equation
Flat Plate	Laminar	Parallel Flow	$\overline{Nu}_D = 0.644 Re_L^{1/2} Pr^{1/3}$	Pr ≥ 0.6	2.28
Flat Plate	Turbulent	Parallel Flow	$\overline{Nu}_D = (0.037 Re_L^{4/5} - A) Pr^{1/3}$ where: $A = 0.037 Re_{x,c}^{4/5} - 0.664 Re_{x,c}^{1/2}$	$0.6 \leq Pr \leq 60$ $Re_{x,c} \leq Re_L \leq 10^8$	2.29
Cylinder	0.4 ≤ Re ≤ 4	Cross Flow	$\overline{Nu}_D = 0.989 Re_D^{0.330} Pr^{1/3}$	Pr ≥ 0.7	2.30
Cylinder	4 ≤ Re ≤ 40	Cross Flow	$\overline{Nu}_D = 0.911 Re_D^{0.385} Pr^{1/3}$	Pr ≥ 0.7	2.31
Cylinder	40 ≤ Re ≤ 4,000	Cross Flow	$\overline{Nu}_D = 0.683 Re_D^{0.466} Pr^{1/3}$	Pr ≥ 0.7	2.32
Cylinder	4,000 ≤ Re ≤ 40,000	Cross Flow	$\overline{Nu}_D = 0.193 Re_D^{0.618} Pr^{1/3}$	Pr ≥ 0.7	2.33
Cylinder	40,000 ≤ Re ≤ 400,000	Cross Flow	$\overline{Nu}_D = 0.027 Re_D^{0.805} Pr^{1/3}$	Pr ≥ 0.7	2.34
Sphere	$3.5 \leq Re \leq 7.6 \times 10^4$	All Around	$\overline{Nu}_D = 2 + (0.4 Re_D^{1/2} + 0.06 Re_D^{1/2}) Pr^{0.4} (\mu/\mu_s)^{1/4}$	$0.71 \leq Pr \leq 380$ $1.0 \leq \mu/\mu_s \leq 3.2$	2.35
Tube Bank *	$10 \leq Re \leq 2 \times 10^6$	Cross Flow	$\overline{Nu}_D = C_1 C_2 Re_D^m Pr^{0.36} (Pr/Pr_s)^{1/2}$	$0.7 \leq Pr \leq 500$	2.36
Packed Bed *	90 ≤ Re ≤ 4,000	All Around	$\varepsilon \bar{j}_h = \varepsilon \bar{j}_m = 2.06 Re_D^{-0.575}$	Pr ≈ 0.7	2.37

The constants C_1, C_2 and m in the tube bank geometry vary with the configuration of the tubes and the Reynolds number (Incropera et al., 2013). Equally, the values of $\bar{j}_h$ and $\bar{j}_m$ are a function of the Prandtl and Reynolds numbers. The value ε is the porosity of the packed bed which depends on the material used for the spheres.

2.3.2.6 Internal Convection

Different to external flow, in internal convection the fluid is now confined, which means there are certain constraints. The totality of the equations which are to be listed will apply to cylindrical tubes, as it is the most common internal geometry in a TES system.

Internal correlation equations take into account the mass flow of the system and the mean velocity, therefore the Reynolds equation changes to incorporate this. The mass flow rate is calculated using the following equation:

Equation 2.38: $\dot{m} = \rho \cdot u_m \cdot A_c$

Where $\dot{m}$ is the mass flow rate, ρ is density, u_m is the mean velocity and Ac is the cross-sectional area.

Equation 2.39: $Re_D = 4\dot{m} / \pi D\mu$

Fluid enters the container through an inlet and leaves after travelling through an outlet. At the inlet, once the fluid makes contact with the surface of the body, the viscous effect starts to slow down the movement of the fluid at the contact and therefore the velocity profile stops being a straight line and acquires a parabolic shape; this is the fully developed region. Before the this, the fluid is considered to be at the hydrodynamic entrance region (Incropera et al., 2013).

It is extremely important to determine the extent of the entrance region. This is calculated differently depending if the fluid is laminar or turbulent:

Equation 2.40: $(x_{fd,h}/D)_{laminar} \approx 0.05 Re_D$

Where $x_{fd,h}$ is the hydrodynamic entry length, D is the diameter and Re_D is Reynolds number. This applies to laminar flow only, with a $Re_D \leq 2300$.

Equation 2.41: $(x_{fd,h}/D)_{turbulent} \approx 4.4\, Re_D^{1/6}$

This applies to turbulent flow only, with a $Re_D \geq 4000$. An illustration of the difference between the hydrodynamic and fully developed regions is shown in Figure 2.8:

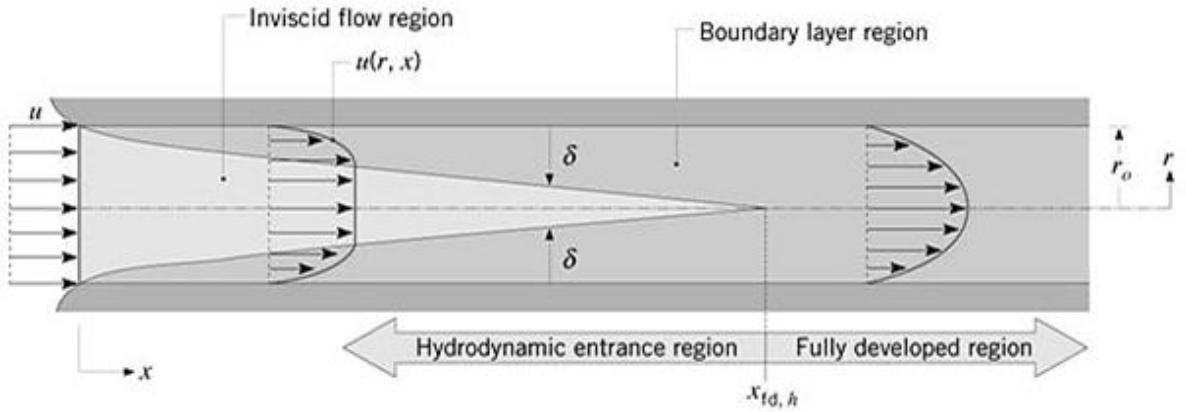

Figure 2.8: Laminar, hydrodynamic boundary layer development in a circular tube (Incropera et al., 2013)

The friction factor *f* which acts against the fluid at the surface of the geometry is an important parameter which is further used in calculating the pressure drop (Incropera et al., 2013).

Equation 2.42: $f_{laminar} = 64 / Re_D$

Equation 2.43: $f_{turbulent} = (0.790 ln Re_D - 1.64)^{-2}$, *for* $3000 \leq Re \leq 5x10^6$

2.3.3 Radiation

Different to conduction and convection, heat transfer by radiation does not need a body or matter. Energy is emitted from oscillations and are therefore transferred in waves or particles. These oscillations are sustained by the internal energy of the body, hence they depend on its temperature. Since it is considered to act as a wave, it is attributed its properties:

Equation 2.44: $\lambda = c/v$

Where λ is wavelength, v is frequency and c is the speed of light which corresponds to $2.988x10^8$ m/s^2 in a vacuum.

As the speed of light is approximately constant, the wavelength will vary depending almost exclusively on the frequency. Not all wavelengths emit thermal radiation, just a small portion which varies from approximately 0.1 to 100µm. This is shown in Figure 2.9 below:

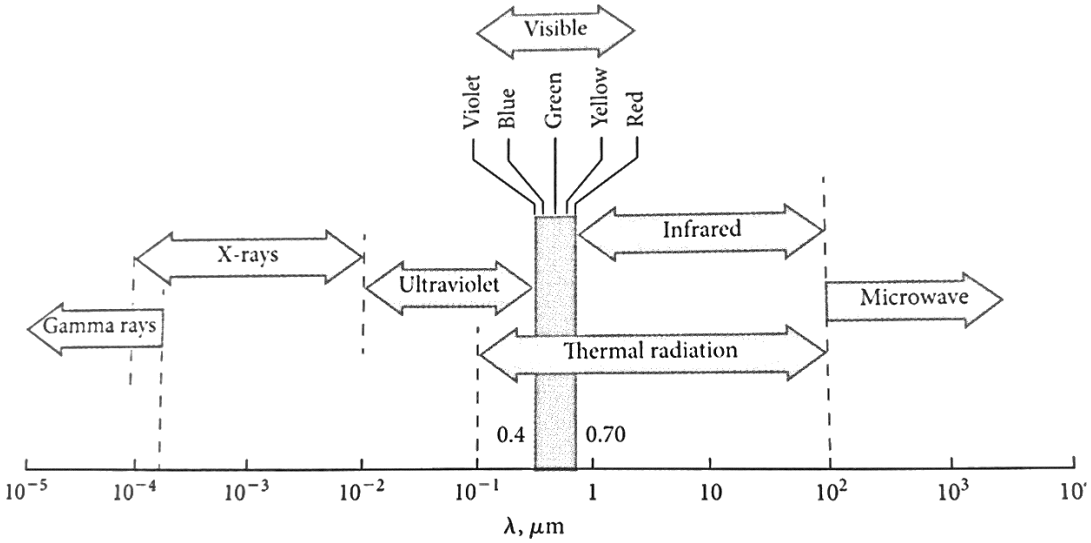

Figure 2.9: Thermal radiation portion of the electromagnetic spectrum (Rolle, 2014)

Therefore, the types of radiation valuable to the TES system are infrared, visible light and some ultraviolet light.

2.3.3.1 Emission, irradiation and radiosity

Once radiation is emitted, the waves or particles eventually irradiate a body or matter. Emission $\dot{E}$ is the rate at which the radiation leaves from a surface per unit area. Once the oscillations reach the body or matter irradiance $\dot{G}$ takes place, which is the rate at which radiation is incident upon a surface per unit area. Lastly, radiosity $\dot{J}$ will occur, which is the rate at which radiation is expelled in a surface per unit area. From these two parameters, $\dot{G}$ and $\dot{J}$, the net radiative flux can be calculated (Incropera et al., 2013).

Equation 2.45: $\dot{E} = \varepsilon\sigma T_s^4$

Where ε is emissivity which is the ratio of thermal radiation from a surface to the radiation of an ideal black body at the same temperature, σ is the Stefan Boltzmann constant, and T_s is the surface temperature.

Equation 2.46: $\dot{J} = \dot{E} + \rho\dot{G}$

Where ρ is density and this equation is applicable to an opaque surface.

Equation 2.47: $\dot{Q}_{rad} = \varepsilon\sigma T_s^4 - \alpha\dot{G}$

Where α is absorptivity and this equation is again applicable to opaque surfaces.

Irradiance depends on further properties. Irradiance can be totally or partially reflected, transmitted through the medium or absorbed. Therefore, the irradiance is the sum of the three:

Equation 2.48: $\dot{G} = \dot{G}_{ref} + \dot{G}_{abs} + \dot{G}_{tr}$

Furthermore, the ratio of reflected energy of reflectivity ρ, transmitted energy of transmissivity τ and absorbed energy or absorptivity α sums to a total of one.

Equation 2.49: $\rho + \tau + \alpha = 1$

A body or surface that has no transmission due to being opaque simplifies the equation to only reflectivity and absorptivity, as $\tau = 0$. A black body absorbs all radiation regardless of wavelength and direction and therefore $\alpha=1$.

2.4 TES System Types

There are three types of heat exchange relevant to TES: sensible heat, latent heat and thermo-chemical. Figure 2.10 shows a summary of the strengths and weaknesses of each type:

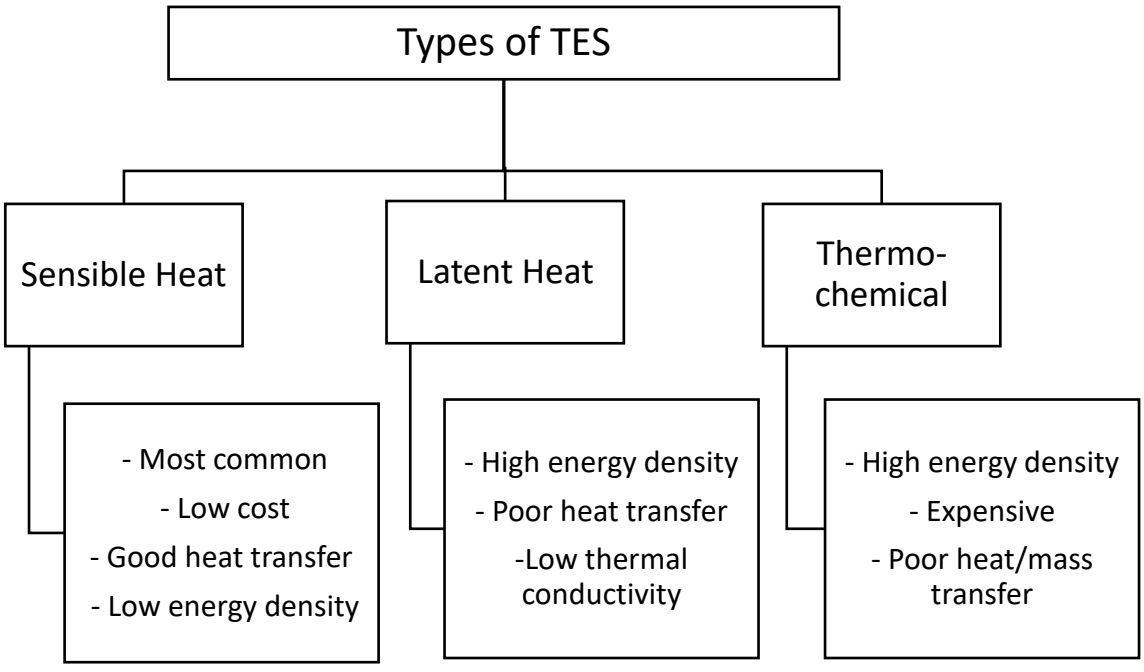

Figure 2.10: Chart showing the advantages and disadvantages of each TES system type (Fang, Lin, & Alva, 2017)

Using energy to change the temperature of a substance (heating/cooling) with no phase change is defined as sensible heat. A phase change is what occurs when a substance changes from a

solid to a liquid (melting) or a liquid to a gas (evaporation). Energy to change the phase of a substance without changing its temperature is known as latent heat.

In a non-ideal system, the system is heated sensibly and the temperature changes until the phase change temperature is reached. The sensible heating continues to ensure the whole contained volume of material reaches the phase change temperature and melts or evaporates fully (Dinçer & Rosen, 2011).

Lastly, thermo-chemical is using the energy given or taken in a chemical reaction to supply or remove heat. It is a promising technique which has not yet been implemented in any existing TES systems due to its cost and high instability (Riffat & Ding, 2012). Therefore, the focus of this section will remain in the other two types.

2.4.1 Sensible Heat

Sensible heat is a thermodynamic process in which the heat exchanged changes the temperature of the body or system. The amount of sensible heat $\dot{Q}$ depends on the mass flow rate $\dot{m}$, the specific heat capacity c_p and the change in temperature ΔT.

Equation 2.50: $\dot{Q} = \dot{m} \cdot c_p \cdot \Delta T$

The specific heat capacity of a material changes depending on the temperature of the substance. Ideally, the system is a closed one where the mass will therefore be constant. Materials with a larger the specific heat capacity and a large temperature difference between the bodies exchange higher amounts of heat.

2.4.1.1 Specific Heat Capacity

The specific heat capacity is the ratio between the amount of heat required to raise the temperature of a body by one degree, and the amount of heat necessary to raise the temperature of the same body and weight by one degree for water (Maxwell, 1872).

The degrees of freedom and the structure of the molecules also affect the heat capacity at a constant volume C_v of a substance, which then affect the specific heat capacity. In monatomic molecules, such as helium, the molecule is able to move everywhere in a 3-D space which comprises of translational motions. These elements have three translational motions where it can move in the x, y or z direction if using a Cartesian coordinate system. Monatomic molecules acquire kinetic energy by collisions.

Aside from translational motion, there are also another two forms in which energy can be stored: rotational energy and potential energy (vibrations). Diatomic molecules, such as hydrogen, have five degrees of freedom which are the three translational motions previously mentioned, plus two rotational degrees of freedom.

Polyatomic molecules have several more degrees of freedom. Some gases such as ammonia have six degrees of freedom, whereas the water molecule has nine. It depends on whether the molecule is linear, symmetric and how many bonds and atoms it has.

Table 2.4 shows common substances and their respective specific heat capacities used in TES systems. As the specific heat capacity changes with temperature, the values given are for ambient temperature unless specified otherwise:

Table 2.5: Relevant substances with their corresponding specific heat capacity values (Gonzalez-Roubaud, Perez-Osorio, & Prieto, 2017; Kumano, Hiroi, & Asaoka, 2017; PCM-Products-Ltd., 2013; Peng, Dong, & Ling, 2014; Sharma, Won, Buddhi, & Park, 2005; Tse, Lavine, Lakeh, & Wirz, 2015)

Substance @ 25°C	c_p [J/kgK]	Substance @ 25°C	c_p [J/kgK]
Hydrogen	14267	Fatty acids (@ 32 - 69°C)	2100 – 2800
Helium	5300	Naphthalene	2446
Argon	520	Paraffin	3260
Xenon	158	Calcium Chloride	1423
Air	1005	Molten Salt (@ 300°C)	1447 – 1560
Sulfur	730	Rubitherm (@ 340°C)	1531
Ammonia	2060	PlusICE	1630 – 2200
Steam (@ 100°C)	2010	Ice (@ 0°C)	2010
Ethyl	2460	Aluminium	896
Methyl	2530	Copper	383
Ethylene Glycol	2200	Stainless Steel	500
Isopentane	164	Glass	840
Therminol	1552 – 1801	Granite	790
Vegetable Oil	2000	Cement	1550
Silicon Oil	1510 – 1760	Concrete	880
Water	4184	Quartzite	730

2.4.2 Latent Heat

The most common forms of latent heat are fusion (melting) and vaporization (boiling). Latent heat of sublimation where the solid will phase change directly to a gas is not commonly used in TES systems due to the vast volume change. Furthermore, there is a type of latent heat known as solid to solid. These change their crystalline structure from one configuration to another, keeping the material as a solid whilst undergoing a change in the lattice (Mishra, Shukla, & Sharma, 2015). The most

commonly implemented in TES systems worldwide is the latent heat of fusion, where the material changes solid↔liquid.

Equation 2.51: $Q = m \cdot \Delta h$

Where Q is the amount of latent heat [kW], m is the mass [kg] and Δh is the change of enthalpy [kJ].

In a TES system the substance starts being heated sensibly in order to reach the phase change temperature. Once this temperature is reached, more sensible heat is transferred into the system to ensure that the whole tank is at the same temperature and there is no thermocline or temperature gradient. The opposite happens in cooling, where the substance releases energy when returning to its original phase.

This combination allows the material to store larger amounts of heat than if the material were just to be heated sensibly. This is demonstrated in the Figure 2.11 below:

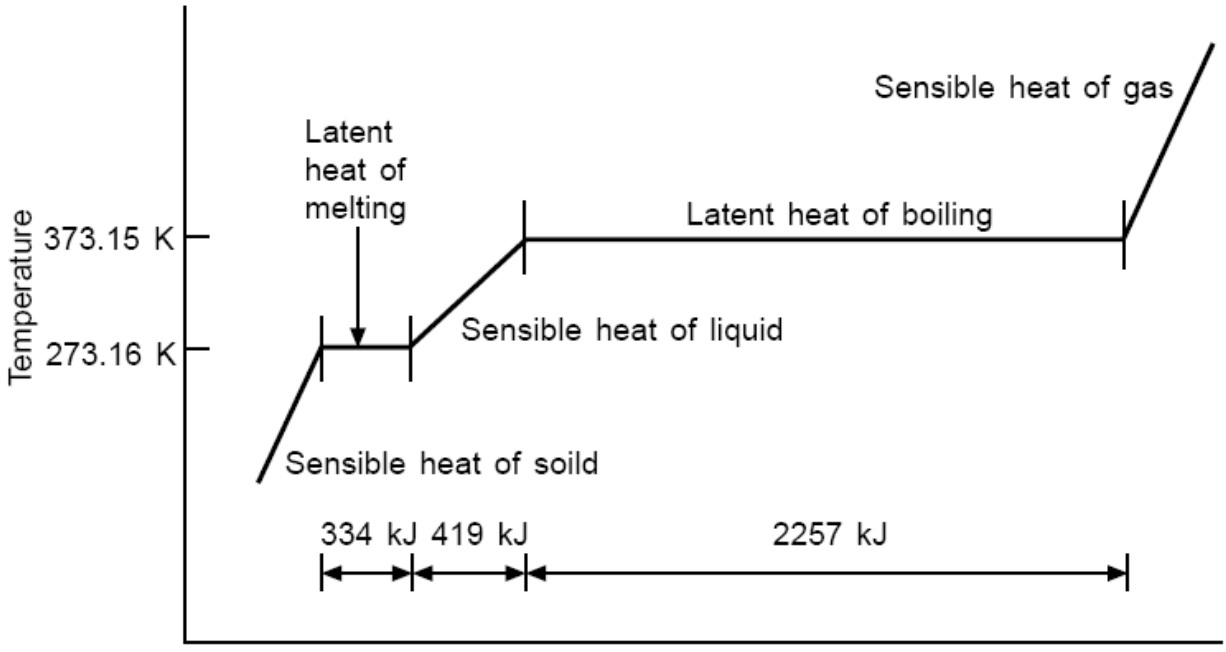

Figure 2.11: Change of temperature and state of water with enthalpy (Almenas, 2014)

The example in Fig 2.11 demonstrates the change of temperature and state of water. The gradient steep lines indicate sensible heating. These show that sensible heat exchanges energy and charges at a faster rate than latent heat, but as denoted from the bottom values in Kilo Joules, more energy can be stored in the phase change denoted by the straight lines.

2.4.2.1 Phase Change Material (PCM)

The material used in the TES system for latent heat is known as a phase change material or PCM. PCMs can be classified as organic, inorganic and eutectic. The hierarchy diagram below breaks down even further the types of PCMs that are used in solid↔liquid latent heat energy TES systems:

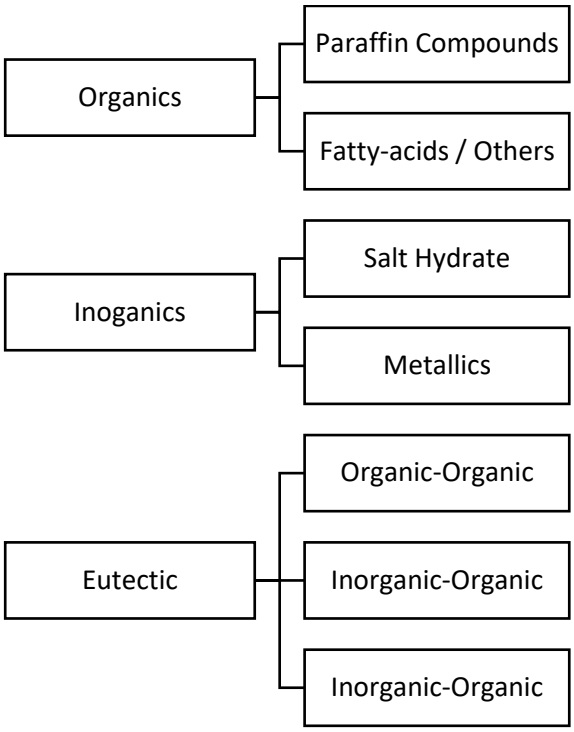

Figure 2.12: Classification of PCMs for TES applications (Sharma, Tyagi, Chen, & Buddhi, 2009)

Paraffin materials have a large temperature range and the melting point is quite flexible due to it varying by the length of the chain. They are inexpensive and non-corrosive materials, yet they have low thermal conductivity and are quite flammable. Non-paraffin organic materials include fatty acids, alcohols, glycols and esters. Except for the fatty acids, these have a low thermal conductivity, some level of toxicity and instability at high temperatures. Some are inflammable and have high heat of fusion which are great improvements to paraffin. Fatty acids also have a large heat of fusion and can freeze without a risk of supercooling, but they are almost two times more expensive than paraffin materials (Sharma et al., 2009).

Metallic materials have no supercooling issues and will not degrade with time after cycling. Salt hydrates have issues with dissimilar melting and the salt placing itself at the bottom of the vessel without dissolving. Additionally, these tend to supercool, meaning a nucleating agent would be required which adds to the total cost (Sharma et al., 2009).

Eutectics are combinations of materials in which the total melting point is less than the individual melting points of the separate elements. Mixtures, are again a combination of various elements where these are individually distinct, different from a compound.

Specific PCM examples are provided below in Table 2.5. The list contains materials applicable and/or used in TES systems and have been split into three main categories.

Table 2.6: Examples of some PCMs (Sharma et al., 2009)

Organic PCMs	Inorganic PCMs	Eutectic PCMs
Paraffin 6106	$CaCl_2 \cdot 12H_2O$	$CaCl_2 \cdot 6H_2O + CaBr_2 \cdot 6H_2O$
Paraffin P116	LiNO3 · 2H2O	$CaCl_2 + MgCl_2 \cdot 6H_2O$
Paraffin 5838	$KFe(SO_4)2 \cdot 12H_2O$	$C_{14}H_{28}O_2 + C_{10}H_{20}O_2$
Paraffin 6035	$FeCl_3 \cdot 6H_2O$	$CH_3CONH_2 + NH_2CONH_2$
Acetic Acid	$Na_2S_2O_3 \cdot 5H_2O$	$CH_3COONa \cdot 3H_2O + NH_2CONH_2$
Polyethylene Glycol	$Na_2CO_3 \cdot 10H_2O$	$Mg(NO_3)_3 \cdot 6H_2O$ + NH4NO3
Eladic Acid	$Na_2HPO_4 \cdot 12H_2O$	$Mg(NO_3)_2 \cdot 6H_2O + MgBr_2 \cdot 6H_2O$
Palmatic Acid	Gallium	$Mg(NO_3)_3 \cdot 6H_2O + MgCl_2 \cdot 6H_2O$
Stearic Acid	Aluminium	$Mg(NO_3)_3 \cdot 6H_2O + Al(NO_3)_2 \cdot 9H_2O$
Methyl Fumarate	Copper	Triethylolethane + water + urea
Lattic Acid	Iron	Triethylolethane + urea
Trimyristin	Titanium	Napthalene + benzoic acid
Bee Wax	Lead	$NH_2CONH_2 + NH_4Br$
Cyanamide	Lithium	$LiNO_3 + NH_4NO_3 + NaNO_3$
Methyl Palmitate	Zinc	$LiNO_3 + NH_4NO_3 + KNO_3$
Acetanilide	Water	$LiNO_3 + NH_4NO_3 + NH_4Cl$

2.5 References for this section

Almenas, K. (2014). Evaporation/Condensation of Water. Unresolved Issues. In F. C. o. t. t. K. a. s. o. w. w. enthalpy (Ed.). USA: Vytautas Magnus University.

Dinçer, I., & Rosen, M. A. (2011). *Thermal Energy Storage: Systems and Applications* (I. Dinçer & M. A. Rosen Eds. Second ed.). Ontario, Canada: John Wiley & Sons.

Fang, G., Lin, Y., & Alva, G. (2017). An overview of thermal energy storage systems. *Energy, 144*, 341-378. doi: 10.1016/j.energy.2017.12.037

Gonzalez-Roubaud, E., Perez-Osorio, D., & Prieto, C. (2017). Review of commercial thermal energy storage in concentrated solar power plants: Steam vs. molten salts. *Renewable and Sustainable Energy Reviews, 80*, 133 - 148.

GrantaDesign. (2010). Thermal conductivity VS thermal diffusivity *The CES EduPack Resource Booklet 2* (Vol. 1037 x 832). Online: Granta Design.

Incropera, F. P., Dewitt, D. P., Bergman, T. L., & Lavine, A. S. (2013). *Principles of Heat and Mass Transfer* (Seventh ed.). Europe: John Wiley & Sons.

Kumano, H., Hiroi, K., & Asaoka, T. (2017). Experimental study on flow and heat transfer characteristics of oil/water emulsions: Part II - Heat transfer characteristics. *Applied Thermal Engineering, 127*, 1555 - 1563.

Levenspiel, O. (1984). *Engineering Flow and Heat Exchange*. Oregon State University, Corvallis: Springer-Verlag.

Lienhard-IV, J. H., & Lienhard-V, J. H. (2017). *A Heat Transfer Textbook* (Fourth ed.). Cambridge, Masachusetts: Phlogiston Press.

Maxwell, J. C. (1872). *Theory of Heat* (Third ed.). London: Longmans, green and co.

Mishra, A., Shukla, A., & Sharma, A. (2015). Latent Heat Storage Through Phase Change Materials. *Indian Academy of Science*, 532 - 541.

Ozisik, M. N. (1993). *Heat Conduction* (Second ed.). United States: John Wiley & Sons.

PCM-Products-Ltd. (2013). PlusICE Phase Change Materials *PCM Summary*.

Peng, H., Dong, H., & Ling, X. (2014). Thermal investigation of PCM-based high temperature thermal energy storage in packed bed. *Energy Conversion and Management, 81*, 420- 427.

Riffat, S. B., & Ding, Y. (2012). Thermochemical energy storage technologies for building applications: a state-of-the-art review. *International Journal of Low-Carbon Technologies, 8*, 106-116.

Rogers, G., & Mayhew, Y. (1992). *Engineering Thermodynamics: Work & Heat Transfer* (Fourth ed.). United Kingdom: Pearson.

Rolle, K. C. (2014). *Heat & Mass Transfer* (K. McIver Ed. Second ed.). United States: Cengage Learning.

Sharma, A., Tyagi, V. V., Chen, C. R., & Buddhi, D. (2009). Review on thermal energy storage with phase change materials and applications. *Renewable and Sustainable Energy Reviews, 13*, 318-345. doi: 10.1016/j.rser.2007.10.005

Sharma, A., Won, L. D., Buddhi, D., & Park, J. U. (2005). Numerical heat transfer studies of the fatty acids for different heat exchanger materials on the performance of a latent heat storage system. *Renewable Energy, 30*, 2179 - 2187.

Taler, J., & Duda, P. (2006). *Solving Direct and Inverse Heat Conduction Problems* (First ed.): Springer-Verlag, Berlin, Heidelberg.

Tse, L. A., Lavine, A. S., Lakeh, R. B., & Wirz, R. E. (2015). Exergetic optimization and performance evaluation of multi-phase thermal energy storage systems. *Solar Energy, 122*, 396 - 408.

III. Literature Review

3.1 TES Systems

Thermal Energy Storage (TES) systems are composed of four essential parts: a storage container, a heat transfer mechanism (pump/exchanger), a heat transfer fluid (HTF) and a storage material.

In any TES system, the ultimate goal is to harvest heat energy to use it effectively in a time of need. This system allows heat to be transferred by conduction and/or convection from the HTF to the storage material, where it retains this heat for a determined time period and lastly transfers the heat back to the HTF for further use. During charging, the high temperature HTF is pumped in cycles across the low temperature storage which slowly increases in temperature. Equally, when the heat energy is being released from the storage into the HTF, it is known as discharging.

Different design types include a single tank or two tanks or heat exchangers. Furthermore, they can comprise of different numbers of pipes or arrays, flow directions and can or cannot be enhanced with metal fins or encapsulated PCMs in order to maximise heat transfer. A design is tailored to the limitations and applications of the system itself.

3.1.1 System design

The design of a TES system is invaluable. The design contributes towards the material selection and denote the operating temperature range of any system.

3.1.1.1 Single-tank

Recently, the most popular design in literature due to its economical aspect is a single-tank design. There are many variations in a single-tank which will contribute to analyse different aspects or fulfil certain functions. Furthermore, any tank design must take into account the aspect ratio as an important parameter, as it will affect the heat distribution of the system.

He et al. chose a vertical cylindrical tank which has a height of 12m and a radius of 2.45m. They argue that having one tank in such an arrangement can save approximately 35% of capital costs compared to a two-tank. Such tank is to be used for a PCM packed-bed system with a thermocline (Y.-L. He, Wu, & Xu, 2014). Ling et al also work with a PCM packed-bed system yet they use a smaller vertical cylindrical tank of height 5m and diameter 1m. In their findings, they conclude that a higher tank is beneficial for a higher charge efficiency (Ling, Peng, & Dong, 2014). Dai et al use a larger tank

of 14m in height and a 20m radius for a packed-bed system. They argue that a two-tank system carries a higher capital cost and lacks potential for cost reduction, making the single-tank a more cost-competitive alternative (Dai, Liu, Cheng, & Zhao, 2017).

Other authors, including Davenne et al, offer a comparison between a vertical cylindrical two-tank system and a single-tank with a thermocline. They conclude that the two-tank system adds to the total cost significantly but mention the thermocline affects the efficiency. In a tank with a height of 32m and a 5m radius, the thermocline is approximately 4-5m. A tank with a slider between hot and cold areas is provided as a solution (Davenne, Garvey, Cardenas, & Simpson, 2017). Manzolini et al also offer this same comparison and agree with the mentioned aspects. Furthermore, they expand that a single-tank system can reduce the cost of the system by up to 33% whilst keeping the same energy capacity. Nevertheless, a single-tank has a lower discharge efficiency. In their 14m height and 23.7m diameter tank design, they also found that stratification is improved in a high aspect ratio tank of height over diameter and that small tanks have high discharge but low collection efficiencies (Manzolini, Lucchini, & Angelini, 2013).

Garimella et al state cycle efficiency is improved with a larger length ratio and higher tanks, adding that the tank height will directly influence temperature transition and output temperatures. They comment a shorter tank will have a sharper temperature gradient and heat exchange zone compared to a taller tank. Moreover, they agree with He et al and support that a single-tank can save costs by 35% (Garimella & Yang, 2012).

Other authors also make use of the cylindrical single-tank for a packed-bed or a thermocline TES system, making it the outstandingly popular choice. Kousksou et al use that design with a tank of a 1.5m height and a 0.6m diameter (Kousksou, Strub, Lasvignottes, Jamil, & Bédécarrats, 2007), similar to Rodriguez et al which have a 1.5m high tank with a 1m diameter (Rodriguez, Rigola, Lehmkuhl, & Galione, 2011). Lastly, Cascetta et al selected a tank that had a larger height to diameter ratio with 1.8m height and 0.58m diameter (Cascetta, Cau, Puddu, & Serra, 2016), whereas Aldoss et al chose a smaller tank design in which height doubled the diameter (0.7m height and 0.35m diameter) (Aldoss & Rahman, 2014).

The vertical yet rectangular storage provided by Badia et al suggests having a number parallelepiped slabs distributed regularly at a studied distance to carry the PCM and enhance the heat transfer (Badia, Aghbalou, & Illa, 2005).

3.1.1.2 Two-tank

Research carried out by White et al shows a two-tank design combined with a reversible heat pump and a Joule Brayton cycle. Here, the tank is a cylindrical reservoir where one tank is used for the cold storage and the other for the hot. Both tanks have the same capacity and size (A. White, Parks, & Markides, 2012). Furthermore, in a later 2014 paper from White et al the same two-tank design is used except the tanks have two different dimensions. The hot store diameter is 4.5m and the cold store diameter is 5.3m, where the length to diameter ratio is one (L/D = 1) (A. J. White, McTigue, & Markides, 2014). Cabeza et al in an experimental setup use a pilot setup where the tanks are cylindrical and 0.5m in height and have a 1.2m in diameter (Cabeza et al., 2018). Desrues et al focus on the use of a rectangular tank for the cold and hot storage instead, where the total tank volume is 21,622m^3 as it is intended for large scale applications (Desrues, Ruer, Marty, & Fourmigué, 2009).

He et al propose a unique three-tank system to store three different types of PCMs, where each tank links directly to the solar collector and HTF (Y.-L. He, Xu, Li, & Song, 2015).

3.1.2.1 Heat exchangers

The most popular in literature related to TES systems is the shell and tube heat exchanger as it can operate in high temperature ranges and pressures.

Tse et al present a shell and tube heat exchanger where the HTF will flow encapsulated inside the cylindrical tubes. The length of the tubes is 12m and the optimized tube radius and pitch values. They mention that a larger tube radius and lower tube pitch decreases the pressure drop but results in a trade-off with heat transfer in terms of exergy destroyed (Tse, Lavine, Lakeh, & Wirz, 2015). Nithyanandam et al also have a shell and tube heat exchanger with the HTF flowing through cylindrical tubes. These are arranged in a triangular layout at 30° horizontally and are made of stainless steel 316. The paper mentions that tube diameter, tube pitch ratio and mass flow rate will affect greatly the storage capacity. For instance, a big pitch results in less tubes and hence less surface area for convective heat transfer. They conclude that the most favourable design in terms of storage capacity is a 1.2 tube pitch ratio and a 0.06m tube diameter (Nithyanandam, Shinn, Barde, & Wirz, 2017).

Bergman et al propose PCM-packed horizontal cylindrical pipes in a rectangular shell. These pipes are in a staggered arrangement and are gravity assisted. The authors note that there is an economical advantage in using heat pipes in a non-cascaded arrangement. The shell has a height of

0.15m, a width of 0.6m and a length of 2m. The pipes are 1m in total length, 0.02m in diameter and a have wall thickness of $2x10^{-3}$m. The pipe length which is exposed to the PCM is 0.684m and the length inside the top and bottom of the HTF channels is 0.15m. Furthermore, there is a wick structure incorporated which has a porosity of 0.7 and a thickness of $0.3x10^{-3}$m (Bergman, Faghri, Robak, & Shabgard, 2012).

He et al investigated the performance of four different tubes in a shell and tube heat exchanger. The study is composed of a smooth tube, a dimpled tube, a cone-finned tube and a helically-finned tube. All tubes have a length of 1.5m, an inner radius of 12.5mm and an outer shell radius of 25.0mm, where the tube thickness is neglected. The dimpled tube the angle between the dimples is 60°, the dimple longitudinal pitch is 15mm, the dimple height is 1.5mm, the major and minor axis of ellipsoidal dimples are 5mm and 3mm respectively. For the cone-finned tube there are three dimensionless parameters: cone height/the inner tube is 0.025, transverse cone pitch/cone height is 7.21 and longitudinal cone pitch/cone height is 3.95. Besides, the cone base diameter is 0.79mm and the cone top angle is 30°. Lastly, the helically-finned tube has two dimensionless parameters: fin height/tube diameter is 0.0244 and fin pitch/fin height is 2.577. In addition, the fin number is 45, the helix angle is 48°, the helix fin base thickness is 0.48mm and the helix fin tip thickness is 0.2mm. The authors agree that all enhancements improve PCM melting rate and that the pressure drop caused by them is not significant and can almost be neglected (Y. L. He, Tao, & Qu, 2012).

Seeniraj et al analyse an enhanced shell and tube heat exchanger. The tube has four equally spaced radial fins which separate the shell into five cells which carry five distinct PCMs. All non-dimensional parameters are as follows: length is 30, fin thickness is 0.25, radius of symmetry line is 1.5 and radius of tube wall is 0.575 (Seeniraj & Narasimhan, 2007). Tse et al have a cylindrical shell and tube heat exchanger suggesting this approach reduces the use of expensive pumps and external heat exchangers. The tube and tank length is 12m, the tube radius is 0.025m, the outer cylindrical control volume radius is 0.026m and the tube spacing is 0.001m (Tse, Ganapathi, Wirz, & Lavine, 2014). Agyenim et al also use a cylindrical shell and tube heat exchanger, except the single tube has longitudinal fins attached to enhance the heat transfer. The outer shell and tube are 1m in length, the outer shell diameter being 152mm and the inner tube diameter being 54mm. The fins have a length of 950mm, a width of 40mm and a thickness of 1mm. The fin pitch is 40mm and there is a 3mm gap between the fin tip and the outer cylinder (Agyenim, Eames, & Smyth, 2010).

Cabeza et al have a system with two heat exchangers for cooling and heating. The cooling system consists of a rectangular cross flow heat exchanger with a zing-zag arrangement of finned tubes. The

system has 700mm height, a 540mm width and a 440mm depth and a pipe inlet diameter if 3/8 inches. There are 56 pipes and 50 fins with a fin heat transfer surface of 15m^2. The heating heat exchanger is a purchased ALFANOVA 76-38H for its high thermal efficiency and its compactness. It has a 208mm length, 191mm width and 618mm height. There are 38 plates made of stainless steel alloy 316, each with a plate thickness of 0.40mm. There are 10 passes on both sides and the heat transfer area is 3.8m^2 (Cabeza et al., 2018).

3.1.2 System materials

Choosing the correct material for the system is challenging as there is always a trade-off between the total cost and the efficiency.

3.1.2.1 Phase-change storage material (PCM)

As mentioned previously, a PCM changes phase in order to absorb or release latent heat in a TES system. There is a wide selection of materials for such applications, each with their corresponding advantages and disadvantages.

An interesting material commonly used as the TES in systems is molten salt. The substance is a solid that changes phase once and will then be maintained above melting temperature where it stores heat sensibly. Molten salts in literature can usually be grouped into three major categories: carbonates, nitrates and metal halides.

Varol et al work with a $CaCl_2.6H_2O$ PCM for their single tank connected to a flat plate collector. This chemical arrangement has a melting point of 29°C and a latent heat fusion of 187.49kJ/kg (Varol, Koyun, Oztop, & Koca, 2007). Similarly, Badia et al use the same material and state the melting temperature to be 29.9°C (Badia et al., 2005). Zhou et al propose a eutectic composition of 87% LiNO3 and 13% NaCl. The melting temperature is 220°C and the latent heat fusion is 290kJ/kg. It operates at a temperature range of 120°C to 300°C (Zhou & Eames, 2017). Oliva et al suggest a molten salt mixture of 60% $NaNO_3$ and 40% KNO_3 as the PCM. The operating temperature for the system is 290°C to 565°C (Oliva, Rigola, Rodríguez, Pérez-Segarra, & Torras, 2014). He et al use a mixture of 80.5% LiF and 19.5% CaF_2 as the PCM for the shell and tube heat exchanger. This substance has a melting temperature of 1040K and a latent heat fusion of 816kJ/kg. The operating temperature of the system is 823K to 1090K (Y. L. He et al., 2012).

Dai et al use a three-layered tank system which has molten salt as the top (high temperature) and bottom (low temperature) layer. The chemical composition of the top layer is a mixture of 20% $LiCO_2$, 60% Na_2CO_3 and 20% K_2CO_3, whereas the bottom layer is simply $NaNO_3$. Melting temperatures of the top and bottom layer materials are 550°C (top) and 308°C (bottom) and latent heat fusion for both substances are 283kJ/kg (top) and 172kJ/kg (bottom). The operating temperature range of the system is between 288°C and 570°C (Dai et al., 2017).

He et al use a cascading three tank system with three PCM, each one placed in an individual tank which connects to the solar collector. PCM1 is composed of 46.6% Li_2CO_3 and 53.4% K_2CO_3, has a melting temperature of 761K and a latent heat fusion of 342kJ/kg. PCM2 is $NaNO_3$, which has a melting temperature of 580K and a latent heat fusion of 177kJ/kg. PCM3 is a mixture of 60% NaNO3 and 40% KNO3, with a melting point of 493K and a latent heat fusion of 161kJ/kg. All three tanks have different operating temperatures. PCM1 ranges from 750K to 850K, PCM2 operates from 550K to 600K and lastly PCM3 works from 450K to 500K (Y.-L. He et al., 2015). Bergman et al use a very similar approach and also have a cascaded TES with three PCMs. PCM1 is composed of 73.3% NaOH and 26.7% NaCl, has a melting temperature of 370°C and a latent heat fusion of 370kJ/kg. PCM2 is a mixture of 22.9% KCl, 60.6% $MnCl_2$ and 16.5% NaCl, with a melting point of 350°C and a latent heat fusion of 215kJ/kg. PCM3 is formed of 65.2% NaOH, 20% NaCl and 14.8% Na_2CO_3, with a melting point of 318°C and a latent heat fusion of 290 kJ/kg. The system operates at a temperature range of 280°C to 390°C (Bergman et al., 2012).

Seeniraj et al propose a system with five PCMs, each one separated in cells denoted by fins in a heat exchanger. The first material, PCM1, is a mixture of 80.5% LiF and 19.5% CaF_2 with a melting point of 1040K. The following PCMs are all eutectic mixtures of the same chemistry and are assumed to have the same properties except the melting points which decrease along the exchanger. Therefore, PCM2 has a melting point of 1008K, PCM3 melts at 973K, PCM4 melts at 923K and PCM5 melts at 873K. The operating temperature of the system is therefore 863K to 1373K (Seeniraj & Narasimhan, 2007).

Roubaud et al analyse in a review various TES technologies which are being used around the world. These work with three molten salt compositions which are being used currently in Italy, Spain, USA and France. The first one is 60% NaNO3 and 40% KNO3 which has a melting point of 220°C and a maximum operating temperature of 585°C. Secondly, there is 7% $NaNO_3$, 53% KNO_3 and 40% $NaNO_2$ with a melting point of 142°C and a maximum operating temperature of 450°C-538°C. Lastly, the composition of 45% KNO_3, 7% $NaNO_2$ and 48% $Ca(NaNO_3)_2$ is mentioned, with a melting point of 120°C

and a maximum operating temperature of 480°C-505°C (González-Roubaud, Pérez-Osorio, & Prieto, 2017).

Paraffin is another material for TES used extensively in literature. He et al use Paraffin wax as their encapsulated PCM in a packed-bed design. It has a melting temperature of 330°C and a latent heat fusion of 226kJ/kg. The system has an operating temperature of 290°C to 390°C (Y.-L. He et al., 2014). Aldoss et al compare a single PCM design to a multi PCM one in the study. Here, they analyse three types of Paraffins which they name PCM40, PCM50 and PCM60. PCM40 has a melting temperature of 42°C to 44°C and a latent heat fusion of 168kJ/kg. PCM50 has a melting temperature of 50°C to 52°C and a latent heat fusion of 200kJ/kg. PCM60 has a melting temperature of 60°C to 62°C and a latent heat fusion of 209kJ/kg. To ensure that all the PCMs arrive to the phase-change, the operating temperature of the system is 30°C to 70°C (Aldoss & Rahman, 2014). Rodriguez et al also use Paraffin wax for their numerical simulation. It has a melting temperature of 59.9°C and a latent heat fusion of 190kJ/kg. The temperature range the system works at is 50°C to 70°C (Rodriguez et al., 2011).

Kousksou et al provide a list of six different type of Paraffins which can be used as PCM materials for TES, particularly for solar applications. These are the following: Hexadecane, Heptadecane, Octadecane, Nonadecane, Eicosane and Heneicosane. The melting points of the substances are 291.25°C, 295.05°C, 301.25°C, 301.25°C, 309.75°C and 311.25°C, respectively. Their latent heat fusions are 236kJ/kg, 214kJ/kg, 244kJ/kg, 222kJ/kg, 248kJ/kg and 213 kJ/kg, respectively (Kousksou et al., 2007).

Rubitherm is a manufactured PCM which are also favourably used in TES systems. Ling et al use Rubitherm as the PCM for their high temperature packed bed TES. It has a melting point of 227.32°C to 303.65°C and a latent heat fusion of 199.6kJ/kg (Ling et al., 2014). Izquierdo-Barrientos et al use two types of Rubitherm GR50 for their fluidized bed system. One is fine and the other is coarse, making them have slight differences in the melting temperature. Fine GR50 melts at 49.8°C and coarse GR50 melts at 50.0°C. Their latent heat fusion temperatures are 52.050kJ/kg (fine) and 54.379°C (coarse). The operating temperature of the systems are 39.4°C to 54.3°C (fine) and 38.6°C to 56.2°C (coarse) (Izquierdo-Barrientos, Sorbino, & Almendros-Ibáñez, 2013).

Lastly, fatty acids are used as an alternative to Paraffins in low heat TES applications with PCMs. Sharma et al provide a study of the various types of fatty acids commonly used in storage applications. The analysed ones are: capric acid, lauric acid, myristic acid, palmitic acid and stearic acid. The melting points of the substances are 32°C, 44°C, 58°C, 64°C and 69°C, respectively. Their latent heat fusions

are 152.7kJ/kg, 177.4kJ/kg, 186.6kJ/kg, 185.4kJ/kg and 202.5kJ/kg, respectively (Sharma, Won, Buddhi, & Park, 2005). Fauzi et al propose to have two mixtures of various fatty acids as the PCMs for TES systems. The mixtures are myristic acid/palmitic acid/sodium myristate (MA/PA/SM) and myristic acid/palmitic acid/sodium palmitate (MA/PA/SP). The melting point of these are 41.36°C and 41.58°C, respectively. Their latent heat fusions are 176.26kJ/kg and 184.06kJ/kg, respetivley. The operating temperature for the system is 40°C to 45°C (Fauzi, Metselaar, Mahlia, Silakhori, & Ong, 2015). Fauzi et al studied the eutectic mixture of Myristic acid with Palmitic acid (70% MA/30% PA). The melting temperature of the mixture is 42.6°C and the latent heat fusion is 169.7kJ/kg. They also found that adding 5% of surfactants can increase the thermal conductivity of the substance. This chemistry has a melting point of 42.36°C and a latent heat fusion of 179.12kJ/kg (Fauzi, Metselaar, Mahlia, Silakhori, & Nur, 2013).

3.1.2.2 Other storage materials

White et al chose magnetite (Fe_3O_4) as the material for the packed bed storage. This is due to is high heat capacity per unit volume and its low fractional variation of heat capacity over the temperature ranges of interest. The magnetite takes the form of spherical capsules with a void fraction of 0.35 in the packed bed (A. J. White et al., 2014). McTigue et al similarly use spherically shaped magnetite particles for a packed bed TES system. These spheres are used in two different setups and have a diameter of 20mm for axial flow, and 16mm for radial flow (McTigue & White, 2017).

Abarr et al selected concrete as the storage material. They took a different approach and used a tube-in-concrete solid structure with holes for the HTF with dimensions 0.1m x 0.1m x 0.2m. It is mentioned that concrete was a favourable option due to being reliable, robust and cost effective. Further to this, it showed no degradation in performance even after being tested for 13,000h between temperatures of 473-673K (Abarr, Geels, Hertzberg, & Montoya, 2016; Abarr, Hertzberg, & Montoya, 2016). Davenne et al also state that granite, alongside concrete, would be the most viable options for a packed bed due to being the most economical options (Davenne et al., 2017).

Quartzite is a favourite material in terms of spherical filler materials in a packed-bed storage. Dai et al use in their TES system a mix of quartzite rocks and sand with a mass ratio of 2:1 respectively. The diameter of the spheres is 19.05 and the porosity is 0.22 (Dai et al., 2017). Manzolini et al also provide a mixture of Quartzite and silica sand for a thermocline TES system, explaining how it is cheap to have it act as the primary energy storage (Manzolini et al., 2013). Garimella et al add to this, expressing how Quartzite is an inexpensive material which is also quite compatible with molten salts

as the HTF. They tested spherical particles which are 0.2m and 0.1m in diameter and settled that the cycle efficiency increases as the particle diameter decreases (Garimella & Yang, 2012). Aside from the Quartzite and sand mixtures, some authors decide to use sand by itself as a filler material. Izquierdo-Barrientos et al use sand as a filler, stating it is a typical material for such systems (Izquierdo-Barrientos et al., 2013) (Izquierdo-Barrientos, Sobrino, & Almendros-Ibáñez, 2014).

The majority of storage materials which have been used sensible TES systems are metals or rocks. White et al used gravel as the material for the packed bed storage (A. White et al., 2012). Chen et al use granite only as the storage material for the randomly placed particles inside the packed bed analysed in the paper (Chen et al., 2014). Alumina is the chosen material for the beads in the packed bed investigated by Cascetta et al. It was selected for its great heat capacity and its stability at high temperatures (Cascetta et al., 2016). Yin et al chose two materials for the storage and compared them. The first material is a 12mm diameter Zirconium ball consisting of Al_2O_3, Fe_2O_3 and 28% Zr. The second is Silicon carbide foam, composed of 80% SiC and 13% SiO2 (Yin, Ding, Jiang, & Yang, 2016).

An uncommon material for storage was analysed by Nithyanandam et al. Sulfur was used as the storage material for a high temperature TES due to its properties. These include high energy density, moderate vapour pressure, high thermal stability and low cost. Also it does not exhibit thermal degradation, unlike molten salts (Nithyanandam et al., 2017).

3.1.2.3 Heat transfer fluid (HTF)

Argon is one of the noble gases commonly chosen as a heat transfer fluid. White et al expresses the preference of Argon over Air as a HTF due to its ability to achieve the same temperature ratio at a lower pressure ratio due to Argon's higher isentropic index (A. White et al., 2012) (A. J. White et al., 2014). Furthermore, McTigue et al investigate the comparison of axial or radial packed beds for TES in which the HTF was Argon. There is a mention about how critical it is for Argon to work at a low pressure, as this will decrease the storage cost of the tank(s) as a pressurized storage would be necessary for high pressure gases (A. White et al., 2012) (McTigue & White, 2017). Desrues et al mentions specifically that the use of Argon as a low heat thermal energy storage (LHTES) will yield very small head losses due to the low velocity of the fluid creating a quasi-uniform pressure in the tank (Desrues et al., 2009).

Other gases, such as Nitrogen and Air, are also a common HTF in TES related papers. Davenne et al suggest using nitrogen in their TES work as it is a dry gas at atmospheric pressure with an effective thermal diffusivity which has the property of maintaining an almost constant specific heat capacity

across a good temperature range (Davenne et al., 2017), which Cascetta et al find Air also has in their paper. Cascetta et al advise Air as a HTF for a sensible heat storage as it can be applied without limits in the temperature range. Besides, it combines Air with a packed bed which allows contact between the storage material, enhancing the heat transfer. The authors mention that Air suffers no degradation or chemical instability and is economical (Cascetta et al., 2016). Chen et al advocate for Air as a HTF for similar reasons; low expense and high reliability as there is no risk of corrosion or blockage under low temperatures (Chen et al., 2014). Nithyanandam et al also express their interest in Air due to its inexpensive material cost, hence why it was chosen over molten salts as a HTF (Nithyanandam et al., 2017). In other sources Air is the HTF simply due to its availability and its easy combination with solar collectors (Ünalan & Özrahat, 2017) (Kousksou et al., 2007).

There are two substances which have been used as heat transfer fluids in TES systems as both gases and liquids and these are Water (or Steam) and Ammonia. Ammonia gas was chosen by Abarr et al as the HTF because it is a high density fluid with good thermodynamic properties. Furthermore, it has a relatively high specific heat ratio compared to refrigerants for a LHTES bottoming a gas cycle and results in higher power density and a cheaper system (Abarr, Geels, et al., 2016; Abarr, Hertzberg, et al., 2016). Jiang et al, alternatively, uses Ammonia as a HTF on its liquid phase as opposed to water as a means of seasonal storage due to being its temperature range and capability of working for low temperature systems that go below 0°C without solidifying (Jiang, Wang, Wang, & Roskilly, 2017).

Many of the TES studies show water as a HTF in the system. Silva et al argue that supercritical water is an excellent HTF because it has favourable properties such as very high energy density (which can be easily predicted to a relative accuracy), high power density, inexpensive cost and high specific heat capacity (Silva & Hobold, 2017). Numerous authors have decided to use water as the working fluid for a TES system that has a phase-change material (PCM) as the storage medium (Ma, Li, & Li, 2017) (Badia et al., 2005) (Aldoss & Rahman, 2014) (Bergman et al., 2012) (Rodriguez et al., 2011) (Fauzi et al., 2015). It is known water is a popular choice HTF due to its well-known thermodynamic and transport properties.

Expanding on liquids that have been used as HTF, some papers show the use of synthetic oils and silicone fluids as part of TES systems. Mobiltherm (Varol et al., 2007), Therminol (Bergman et al., 2012) (Cabeza et al., 2018) and Syltherm (Cabeza et al., 2018) are some examples used due to their high thermal resistance, thermal stability, good heat transfer efficiency and wide operating temperatures. Tse et al published systems featuring other oils, where Naphthalene and Paraxylene are employed instead (Tse et al., 2015) (Tse et al., 2014).

Many authors have investigated the use of molten salts as a HTF instead of the storage material. Molten salt as a HTF allows the fluid to be circulated during the day and stored in the tank at night, where the tank is kept at atmospheric pressure reducing costs. A popular chemical composition which appears repeatedly in literature is Sodium Nitrate combined with Potassium Nitrate ($NaNO_3$+KNO_3).

He et al use a combination of 60% $NaNO_3$ and 40% KNO_3 for their PCM capsule packed-bed HTF on a temperature range of 290°C to 390°C (Y.-L. He et al., 2014). Equally, Ling et al use the same composition and use a wider temperature range of 250°C to 400°C (Ling et al., 2014). Dai et al prefer working on a higher temperature range for that chemical composition and have the HTF operate from 288°C to 570°C (Dai et al., 2017). Pitchumani et al likewise study a system which operated with a temperature range of 290°C to 574°C, however using a mixture between a solar salt and a eutectic. The solar salt has the common percentage of 60% $NaNO_3$ and 40% KNO_3 and the eutectic has 20% Li_2CO_3, 60% Na_2CO_3 and 20% K_2CO_3 (Pitchumani, Nithyanandam, & Mathur, 2013). Garimella et al use a eutectic combination of 53% KNO_3, 40% $NaNO_2$ and 7% $NaNO_3$ as the HTF, which has a melting point of 149°C. They further state that molten salts are cheaper and more environmentally friendly than many of the currently used synthetic oils (Garimella & Yang, 2012). Yin et al provide another eutectic mixture similar to the prior but with added chlorides that bring the melting point down to 140°C. The molten salt is a combination of 50.5% KNO_3, 38.1% $NaNO_2$, 6.7% $NaNO_3$ and 4.7% additive chlorides, and works in a temperature range of 290°C to 370°C (Yin et al., 2016).

Other uncommon molten salts that are presented in literature are liquid Sodium, by Seeniraj et al, and hydrated Lithium Bromide ($LiBr.H_2O$) by Agyenim et al. Liquid Sodium works with extremely high temperatures of 590°C to 1100°C (Seeniraj & Narasimhan, 2007), whereas LiBr.H2O works with low temperatures of approximately 70/90°C to 140°C (Agyenim et al., 2010). This really shows the flexibility and how versatile molten salts are over other HTFs when working in TES systems.

3.1.3 System applications

3.1.3.1 Joule-Brayton cycle, Rankine cycles and Heat Pumps

In TES systems that use gases as a HTF, it is very common that they are combined with a Joule-Brayton or Rankine cycle.

White et al combine a two-tank packed bed with a heat engine, a heat pump, a compressor, an expander and a reversible Joule-Brayton cycle (A. White et al., 2012). This same system is later

used with the addition of a buffer vessel (A. J. White et al., 2014). Desrues et al follow a similar pattern and have a system consisting of a two-tank packed bed with four turbomachines (two compressor/turbine pairs for charging and discharging) and two heat exchangers. These again follow a Joule-Brayton cycle and allow the system to take/generate electricity (Desrues et al., 2009).

Tse et al study a shell and tube heat exchanger with the addition of a steam Rankine cycle for the discharging loop only (Tse et al., 2014). The same design is proposed in another study which focuses on a parametric investigation to optimise the system (Tse et al., 2015). Roubaud et al focus in the comparison of a TES system with a combined Rankine cycle with different plant configurations, and storage concepts and sizes (González-Roubaud et al., 2017). Ma et al discuss the performance of an organic Rankine cycle (ORC) with a TES system. They state an ORC shows great flexibility, high safety, good reliability and simplicity (Ma et al., 2017).

Abarr et al works with a reversible heat pump combined with a thermal engine which contains two compressors/expanders. It is modelled to become a bottoming TES system in an air-cooled evaporator/condenser which exchanges heat with ambient air (Abarr, Geels, et al., 2016; Abarr, Hertzberg, et al., 2016).

3.1.3.2 Thermal solar collectors

Luo et al propose a system composed of four main elements: a solar concentrator, a high temperature solar receiver, a TES fluid transport system and a power generation bloc to provide electricity. They show four main types of collectors: parabolic trough collectors (PTC), linear Fresnel reflectors (LFR), solar power towers (SPT) and parabolic dish collectors (PDC). PTC has operating temperatures of 20°C-400°C with plenty experimental data available and low installation costs. LFR has operating temperatures of 50°C to 300°C with low installation costs. SPT have very high operating temperatures of 300°C to 1000°C and high thermodynamic efficiencies. They show a great potential for low cost storage, but have a high installation cost. PDC has the widest temperature range with an operating temperature of 120°C to 1500°C. Nevertheless, the integration of a TES is difficult (Luo, Pelay, Fan, Stitou, & Rood, 2017). Roubaud et al state that concentrating solar power is an exceptional resource and powerful tool among renewable energy generation due to it being easily combined with a TES system. They reinforce that the main four CSP technologies are the four stated by Lingai et al (González-Roubaud et al., 2017). Cabeza et al investigate the performance of a test experimental setup alongside Abengoa Reserch for the startup and operation of a CSP with TES system. They state the most accomplished collectors are the parabolic trough and the solar tower designs, where the

operating temperatures in real built facilities range from 293°C to 400°C and 250°C to 550°C, respectively (Cabeza et al., 2018).

Nithyanandam et al mentions that coupling CSP with TES will aid during intermittency times and will negate the use of fuel based backup systems which produce greenhouse gases (Nithyanandam et al., 2017). Ma et al reinforce this by suggesting TES can achieve peak load shifting which allows energy stored during the day to be released at night or during cloudy days in times of demand (Ma et al., 2017). He et al propose a numerical study in a TES system which uses a solar dish in CSP generation systems (Y. L. He et al., 2012). Bergman et al work with operating temperatures which correspond to the ones in parabolic trough solar power plants which are currently in use (Bergman et al., 2012). Garimella et al consider the single-tank thermocline to be charged by a parabolic trough collector field which offers the possibility to feed electricity without using fossil-fuels (Garimella & Yang, 2012).

Dai investigate the thermal performance of a 100MW CSP plant integrated with a packed-bed TES over a 14-day study (Dai et al., 2017). Manzolini et al model a CSP and TES single tank with a thermocline combination. They use real data extracted from a 50MW two-tank system Andasol CSP power plant for the study (Manzolini et al., 2013).

3.1.4 System modelling

The study takes a numerical approach to solve the thermal equations in the TES. General approaches reported in literature include CFD software such as ANSYS and COMSOL, or solving numerical problems through MATLAB.

Talukdar et al model a finned heat exchanger TES, using PCM, in an energy backup system. They investigate several thicknesses (4.5cm, 5.0cm, 5.5cm, 6.0cm, 6.5cm and 7.0cm) for the PCM pack and the model is a 3D computational fluid dynamics (CFD) simulation for both charging and discharging. They employed the enthalpy-porosity technique that is present in the ANSYS Fluent 15.0 package to model the solidification and melting and develop the 3D simulation model (Talukdar et al., 2019).

Equally, Mahdi et al also numerically model a shell-and-tube heat exchanger using paraffin wax as the storage material. They test finned and non-finned vertical configurations and compare them to their experimental setup. The numerical 3D CFD model is configured in ANSYS Fluent R.15 and they use the enthalpy-porosity method to simulate the phase change phenomena (Mahdi et al., 2019).

Lin et al study experimentally and numerically the thermal performance of a novel spiral tube heat exchanger latent heat TES system. They investigate the phase change behaviour of the PCM (sodium acetate trihydrate) using a mathematical model based on the enthalpy-porosity method solved in ANSYS Fluent. The cylindrical system was built using Solidworks (Lin et al., 2021).

Kant et al study the performance of five different fatty acids (Capric acid, Lauric acid, Myristic acid, Palmitic acid and Stearic acid) in a 2D latent heat TES system. The numerical simulation of heating and cooling of the materials is evaluated using finite element analysis (FEM) in the software COMSOL Multiphysics 5.0. The time-dependent study was carried out by Newtonian iteration techniques with backward differentiation formula time stepping methods (Kant et al., 2016).

Likewise, Akhmetov et al study a 3D latent heat TES using two materials based on paraffin waxes (PW-L and PW-H) with different phase change temperature ranges, numerically solved using CFD in the software COMSOL Multiphysics 5.2. The melting point of the PW-L is 44–48 °C approximately and consist of a mixture of various low melting point paraffin wax components. The melting point of PW-H is 64–66 °C approximately and its composition is mostly C18-C40 carbon atoms (Akhmetov et al., 2019).

Siyabi et al numerically analyse a shell and tube heat exchanger for charging and discharging, employing the multiple PCM technique. The three PCM investigated are Rubitherm, with three different low melting temperatures (27°C, 33°C and 41°C). They use COMSOL Multiphysics, specifically the “Heat Transfer” physics for modelling the heat transfer in the solid, fluids and phase change materials and the “Fluid Flow” physics was to model the HTF flow and PCM during the melting and solidification (Siyabi et al., 2021).

Fernandes et al opted for using a combination of TRNSYS and MATLAB to optimise and assess their TES system. The system integrates the adsorption heat storage unit in a hot water storage tank which has silica gel as its storage material and water as the HTF. The solar system is modelled using TRNSYS, the model for the absorption module (absorber, condenser, secondary water tank and evaporator) was built in MATLAB, and the TRNSYS hot water storage was modified to integrate the absorber, taking advantage of the interactions of both software packages (Fernandes et al., 2018).

Furthermore, Ismaeel et al model an underground TES tank charged by solar energy to be used for wheat drying for long-term storage that is solved using a MATLAB code. The code is developed to evaluate the performance of the parameters (water temperature in the tank, Coefficient of

Performances for the heat pump and system, Specific Moisture Evaporation Rate, and energy fractions) each hour for years (Ismaeel et al., 2020).

Eppinger et al work on finding optimal fluids and operating parameters for a combined Pumped TES and an Organic Rankine Cycle (ORC). The use of an ORC for heat to power conversion increases the cost efficiency of the storage, yet requires both cycles to run on the same fluid. Therefore, they analyse both latent and sensible storage systems for a variety of fluids, which are assessed based on their suitability for a range of operating conditions. The simulations are performed using a custom MATLAB model, with the fluid data provided by REFPROP (Eppinger et al., 2020).

3.2 System Selection

From this literature, an informed decision can be reached regrading system selection. Finding a system application is the first step, as from there materials and other parameters are chosen. A plethora of literature sources focus on solar collectors and high grade systems, with large scale projects for steam and electricity generation. This application was discarded, yet realizing that research on small scale domestic applications was more limited. The aim of this study focuses on low grade TES applications, such as heat waste recovery, water heating, central heating etc.

Deciding on a design was the natural following step. Single tank was chosen, as they are cost effective, as confirmed in many studies, and can save space, both exceptionally beneficial for domestic users. A ratio of 1/1 on the height/diameter of the tank was chosen due to limited research focusing on the benefits or drawbacks of this design. Therefore, here resides a gap in the literature.

From the literature review, gases work with high pressure and therefore increased the cost for having to pressurize the tank and solids had very poor specific heat capacities, so liquid mediums were decided upon. Since the system is low grade and single tank, materials that function in low temperatures are required. The most suitable liquid materials at low temperature are oils, paraffin types, organic types and fatty acids. Advantages of these are that they can be used in both sensible and latent heat systems, depending on their melting points.

Papers which focused on 3D models commonly used ANSYS Fluent. Ones using COMSOL worked in 2D or 2D axisymmetrical spaces, which were equally as effective whilst saving computational cost and time (Akhmetov et al., 2019). Furthermore, the COMSOL papers found investigated operating temperatures which were on the low temperature spectrum, and utilised materials that had lower melting temperatures which combined well with water as the HTF. Therefore,

ultimately the most effective choice for the study was to establish COMSOL as the software for solving the heat transfer problems in a 2D space.

There is a gap in the literature regarding how encapsulated liquid mediums (especially organics, paraffins and acids) perform as sensible heat materials in low grade TES systems and the tank design chosen is poorly understood. Furthermore, in latent heat storage systems, there is a huge selection of materials to choose from, yet there is no clear correlation between how specific thermal properties affect certain outputs, such as temperature dynamics or heat absorption, in encapsulated and packed single tank systems.

This study's goal and the gap in literature, therefore, is to inform and inspire into looking at the relationship between thermal parameters and the analysed outputs for low grade and low temperature materials. There is limited research on how these parameters affect the system performance and to which extent (quantitative effect). This will allow an easier and faster material selection, and opens the door to designing new materials based on beneficial thermal parameters.

3.3 References for this section

Abarr, M., Geels, B., Hertzberg, J., & Montoya, L. D. (2016). Pumped thermal energy storage and bottoming system part A - Concept and model. *Energy, 120*, 320-331. doi: 10.1016/j.energy.2016.11.089

Abarr, M., Hertzberg, J., & Montoya, L. D. (2016). Pumped thermal energy storage and bottoming system part B - Sensitivity analysis and performance. *Energy, 119*, 601-611. doi: 10.1016/j.energy.2016.11.028

Agyenim, F., Eames, P., & Smyth, M. (2010). Experimental study on the melting and solidification behaviour of a medium temperature phase change storage material (Erythritol) system augmented with fins to power a LiBr/H2O absorption cooling system. *Renewable Energy, 36*, 108-117. doi: 10.1016/j.renene.2010.06.005

Akhmetov B., Navarro M.E., Seitov A., Kaltayev A., Bakenov Z., Ding Y. (2019). Numerical study of integrated latent heat thermal energy storage devices using nanoparticle-enhanced phase change materials. Solar Energy 194: 724-741. doi: 10.1016/j.solener.2019.10.015.

Aldoss, T. K., & Rahman, M. M. (2014). Comparison between the single-PCM and multi-PCM thermal energy storage design. *Energy Conversion and Management, 83*, 79-87. doi: 10.1016/j.enconman.2014.03.047

Badia, F., Aghbalou, F., & Illa, J. (2005). Exergetic optimization of solar collector and thermal energy storage system. *International Journal of Heat and Mass Transfer, 49*, 1255-1263. doi: 10.1016/j.ijheatmasstransfer.2005.10.014

Bergman, T. L., Faghri, A., Robak, C. W., & Shabgard, H. (2012). Heat transfer and exergy analysis of cascaded latent heat storage with gravity-assisted heat pipes for concentrating solar power applications. *Solar Energy, 86*, 816-830. doi: 10.1016/j.solener.2011.12.008

Cabeza, L. F., Miró, L., Jové, A., Gasia, J., Prieto, C., & Peiró, G. (2018). Two tank molten salts thermal energy storage system for solar power plants at pilot plant scale: lessons learnt and recommendations for its design, start-up and operation. *Renewable Energy, 121*, 236-248. doi: 10.1016/j.renene.2018.01.026

Cascetta, M., Cau, G., Puddu, P., & Serra, F. (2016). A comparison between CFD simulation and experimental investigation of a packed-bed thermal energy storage system. *Applied Thermal Engineering, 98*, 1263-1272. doi: 10.1016/j.applthermaleng.2016.01.019

Chen, H., Tan, C., Yang, L., Liu, J., Wang, L., & Chai, L. (2014). Performance study of a packed bed in a closed loop thermal energy storage system. *Energy, 77*, 871-879. doi: 10.1016/j.energy.2014.09.073

Dai, Z.-m., Liu, C., Cheng, M.-s., & Zhao, B.-c. (2017). Cyclic thermal characterization of a molten-salt packed-bed thermal energy storage for concentrating solar power. *Applied Energy, 195*, 761-773. doi: 10.1016/j.apenergy.2017.03.110

Davenne, T. R., Garvey, S. D., Cardenas, B., & Simpson, M. C. (2017). The cold store for a pumped thermal energy storage system. *Journal of Energy Storage, 14*, 295-310. doi: 10.1016/j.est.2017.03.009

Desrues, T., Ruer, J., Marty, P., & Fourmigué, J. F. (2009). A thermal energy storage process for large scale electric applications. *Applied Thermal Engineering, 30*, 425-432. doi: 10.1016/j.applthermaleng.2009.10.002

Eppinger B., Zigan L., Karl J., Will S. (2020). Pumped thermal energy storage with heat pump-ORC-systems: Comparison of latent and sensible thermal storages for various fluids. Applied Energy, 280, 115940. doi: 10.1016/j.apenergy.2020.115940

Fauzi, H., Metselaar, H. S. C., Mahlia, T. M. I., Silakhori, M., & Nur, H. (2013). Phase change material: Optimizing the thermal properties and thermal conductivity of myristic acid/palmitic acid eutectic mixture with acid-based surfactants. *Applied Thermal Engineering, 60*, 261-265. doi: 10.1016/j.applthermaleng.2013.06.050

Fauzi, H., Metselaar, H. S. C., Mahlia, T. M. I., Silakhori, M., & Ong, H. C. (2015). Thermal characteristic reliability of fatty acid binary mixtures as phase change materials (PCMs) for thermal energy storage applications. *Applied Thermal Engineering, 80*, 127-131. doi: 10.1016/j.applthermaleng.2015.01.047

Fernandes M.S., Gaspar A.R., Costa V.A.F., Costa J.J., Brites G.J.V.N. (2018). Optimization of a thermal energy storage system provided with an adsorption module – A GenOpt application in a TRNSYS/MATLAB model. Energy Conversion and Management 162: 90-97. doi: 10.1016/j.enconman.2018.02.027

Garimella, S. V., & Yang, Z. (2012). Cyclic operation of molten-salt thermal energy storage in thermoclines for solar power plants. *Applied Energy, 103*, 256-265. doi: 10.1016/j.apenergy.2012.09.043

González-Roubaud, E., Pérez-Osorio, D., & Prieto, C. (2017). Review of commercial thermal energy storage in concentrated solar power plants- Steam vs. molten salts. *Renewable and Sustainable Energy Reviews, 80*, 133-148. doi: 10.1016/j.rser.2017.05.084

He, Y.-L., Wu, M., & Xu, C. (2014). Dynamic thermal performance analysis of a molten-salt packed-bed thermal energy storage system using PCM capsules. *Applied Energy, 121*, 184-195. doi: 10.1016/j.apenergy.2014.01.085

He, Y.-L., Xu, Y., Li, Y.-Q., & Song, H.-J. (2015). Exergy analysis and optimization of charging–discharging processes of latent heat thermal energy storage system with three phase change materials. *Solar Energy, 123*, 206-216. doi: 10.1016/j.solener.2015.09.021

He, Y. L., Tao, Y. B., & Qu, Z. G. (2012). Numerical study on performance of molten salt phase change thermal energy storage system with enhanced tubes. *Solar Energy, 86*, 1155-1163. doi: 10.1016/j.solener.2012.01.004

Ismaeel H.H., Yumrutaş R. (2020). Investigation of a solar assisted heat pump wheat drying system with underground thermal energy storage tank. Solar Energy, 199, 538-551. doi: 10.1016/j.solener.2020.02.022

Izquierdo-Barrientos, M. A., Sobrino, C., & Almendros-Ibáñez, J. A. (2014). Energy storage with PCM in fluidized beds: Modeling and experiments. *Chemical Engineering Journal, 264*, 497-505. doi: 10.1016/j.cej.2014.11.107

Izquierdo-Barrientos, M. A., Sorbino, C., & Almendros-Ibáñez, J. A. (2013). Thermal energy storage in a fluidized bed of PCM. *Chemical Engineering Journal, 230*, 573-583. doi: 10.1016/j.cej.2013.06.112

Jiang, L., Wang, R. Z., Wang, L. W., & Roskilly, A. P. (2017). Investigation on an innovative resorption system for seasonal thermal energy storage. *Energy Conversion and Management, 149*, 129-139. doi: 10.1016/j.enconman.2017.07.018

Kousksou, T., Strub, F., Lasvignottes, J. C., Jamil, A., & Bédécarrats, J. P. (2007). Second law analysis of latent thermal storage for solar system. *Solar Energy Materials and Solar Cells, 91*, 1275-1281. doi: 10.1016/j.solmat.2007.04.029

Kant K., Shukla A., Sharma A. (2016). Performance evaluation of fatty acids as phase change material for thermal energy storage. *Journal of Energy Storage* 6: 153-162. doi: 10.1016/j.est.2016.04.002

Lin W., Ling Z., Fang X., Zhang Z. (2021). Experimental and numerical research on thermal performance of a novel thermal energy storage unit with phase change material. Applied Thermal Engineering, 186, 116493. doi: 10.1016/j.applthermaleng.2020.116493

Ling, X., Peng, H., & Dong, H. (2014). Thermal investigation of PCM-based high temperature thermal energy storage in packed bed. *Energy Conversion and Management, 81*, 420-427. doi: 10.1016/j.enconman.2014.02.052

Luo, L., Pelay, U., Fan, Y., Stitou, D., & Rood, M. (2017). Thermal energy storage systems for concentrated solar power plants. *Renewable and Sustainable Energy Reviews, 79*, 82-100. doi: 10.1016/j.rser.2017.03.139

Ma, H., Li, W., & Li, S. (2017). Dynamic performance analysis of solar organic Rankine cycle with thermal energy storage. *Applied Thermal Engineering, 129*, 155-164. doi: 10.1016/j.applthermaleng.2017.10.021

Manzolini, G., Lucchini, A., & Angelini, G. (2013). Comparison of Thermocline Molten Salt Storage Performances to Commercial Two-tank Configuration. *Energy Procedia, 49*, 694-704. doi: 10.1016/j.egypro.2014.03.075

McTigue, J., & White, A. (2017). A Comparison of Radial-flow and Axial-flow Packed Beds for Thermal Energy Storage. *Energy Procedia, 105*, 4192-4197. doi: 10.1016/j.egypro.2017.03.893

Mustafa S. Mahdi, Ahmed F. Hasan, Hameed B. Mahood, Alasdair N. Campbell, Anees A. Khadom, Abdul Mun'em A. Karim, Adel O.Sharif (2019). Numerical study and experimental validation of the effects of orientation and configuration on melting in a latent heat thermal storage unit. Journal of Energy Storage 23: 456-468. doi: 10.1016/j.est.2019.04.013

Nithyanandam, K., Shinn, M., Barde, A., & Wirz, R. E. (2017). Sulfur-based thermal energy storage system using intermodal containment- Design and performance analysis. *Applied Thermal Engineering, 128*, 1009-1021. doi: 10.1016/j.applthermaleng.2017.08.167

Oliva, A., Rigola, J., Rodríguez, I., Pérez-Segarra, C. D., & Torras, S. (2014). Parametric study of two-tank TES system for CSP plants. *Energy Procedia, 69*, 1049-1058. doi: 10.1016/j.egypro.2015.03.206

Pitchumani, R., Nithyanandam, K., & Mathur, A. (2013). Analysis of a latent thermocline storage system with encapsulated phase change materials for concentration solar power. *Applied Energy, 113*, 1446-1460. doi: 10.1016/j.apenergy.2013.08.053

Rodriguez, I., Rigola, J., Lehmkuhl, O., & Galione, P. A. (2011). *Numerical simulations of thermal energy storage systems with phase change materials*. Paper presented at the ISES Solar World Congress, , Kassel, Germany.

Seeniraj, R. V., & Narasimhan, N. L. (2007). Performance enhancement of a solar dynamic LHTS module having both fins and multiple PCMs. *Solar Energy, 82*, 535-542. doi: 10.1016/j.solener.2007.11.001

Sharma, A., Won, L. D., Buddhi, D., & Park, J. U. (2005). Numerical heat transfer studies of the fatty acids for different heat exchanger materials on the performance of a latent heat storage system. *Renewable Energy, 30*, 2179-2187. doi: 10.1016/j.renene.2005.01.014

Siyabi I.A., Khanna S., Mallick T., Sundaram S. (2021). Experimental and numerical study on the effect of multiple phase change materials thermal energy storage system. Journal of Energy Storage, 36, 102226. doi: 10.1016/j.est.2020.102226

Silva, A. K. d., & Hobold, G. M. (2017). Critical phenomena and their effect on thermal energy storage in supercritical fluids. *Applied Energy, 205*, 1447-1458. doi: 10.1016/j.apenergy.2017.09.081

S. Talukdar, H. M. M. Afroz, M. A. Hossain, M.A. Aziz. (2019). Heat transfer enhancement of charging and discharging of phase change materials and size optimisation of a latent thermal energy storage system for solar cold storage application. *Journal of Energy Storage* 24: 100797. doi: 10.1016/j.est.2019.100797

Tse, L. A., Ganapathi, G. B., Wirz, R. E., & Lavine, A. S. (2014). Spatial and temporal modeling of sub- and supercritical thermal energy storage. *Solar Energy, 103*, 402-410. doi: 10.1016/j.solener.2014.02.040

Tse, L. A., Lavine, A. S., Lakeh, R. B., & Wirz, R. E. (2015). Exergetic optimization and performance evaluation of multi-phase thermal energy storage systems. *Solar Energy, 122*, 396-408. doi: 10.1016/j.solener.2015.08.026

Ünalan, S., & Özrahat, E. (2017). Thermal performance of a concrete column as a sensible thermal energy storage medium and a heater. *Renewable Energy, 111*, 561-579. doi: 10.1016/j.renene.2017.04.046

Varol, Y., Koyun, T., Oztop, H. F., & Koca, A. (2007). Energy and exergy analysis of a latent heat storage system with phase change material for a solar collector. *Renewable Energy, 33*, 567-574. doi: 10.1016/j.renene.2007.03.012

White, A., Parks, G., & Markides, C. N. (2012). Thermodynamic analysis of pumped thermal electricity storage. *Applied Thermal Engineering, 53*, 291-298. doi: 10.1016/j.applthermaleng.2012.03.030

White, A. J., McTigue, J. D., & Markides, C. N. (2014). Parametric studies and optimisation of pumped thermal electricity storage. *Applied Energy, 137*, 800-811. doi: 10.1016/j.apenergy.2014.08.039

Yin, H., Ding, J., Jiang, R., & Yang, X. (2016). Thermocline characteristics of molten-salt thermal energy storage in porous packed-bed tank. *Applied Thermal Engineering, 110*, 855-863. doi: 10.1016/j.applthermaleng.2016.08.214

Zhou, D., & Eames, P. (2017). A study of a eutectic salt of lithium nitrate and sodium chloride (87–13%) for latent heat storage. *Solar Energy Materials and Solar Cells, 167*, 157-161. doi: 10.1016/j.solmat.2017.04.016

IV. Methodology

4.1 Initial modelling (sensible heat)

An extensive analysis of various systems and the work of other authors helped to clarify the type of system that was going to be modelled first. The software for the initial setup is COMSOL Multiphysics, version 5.3, with the aid of the heat transfer package which allows an analysis of temperature in space and time. The process to determining the parameters and variables in this selected system is summarised in a flow chart:

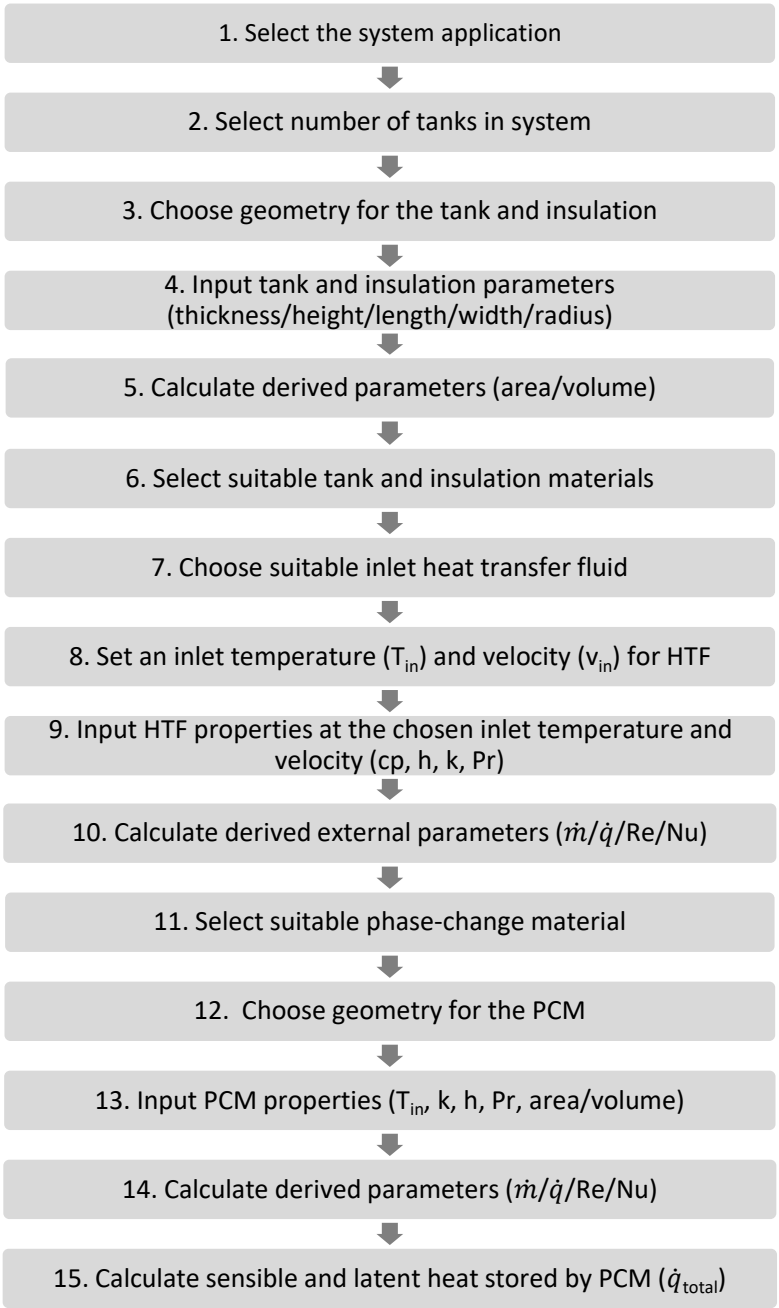

Figure 4.1: Step by step flow chart of methodology process

The system modelled was determined as a single cylindrical tank with packed bed and encapsulated material connected to a solar collector. This is chosen as a single tank with a packed bed helps reduce the system cost yet provides good heat absorption, especially if the material absorbs latent heat. Modelling the complete system takes time and computational power, therefore the initial simulations are tests which provide insight on how the software behaves.

4.1.1 System Design and Mesh

A 2D model of the tank was constructed using the geometry tools in COMSOL Multiphysics. The tank, excluding the frame, was square with 0.5m x 0.5m dimensions (L/D = 1). The Aluminium frame is 0.025m thick and has two voids of 0.16m which represent the inlet (top) and outlet (bottom). There are 25 spheres inside the tank with a 0.025m radius, each one encapsulated in a frame with 0.005m thickness. Each sphere, without the capsule thickness, has a volume of $7x10^{-5}$ m^3. The space where the spheres reside is filled with still water. Figure 4.2 shows the full design:

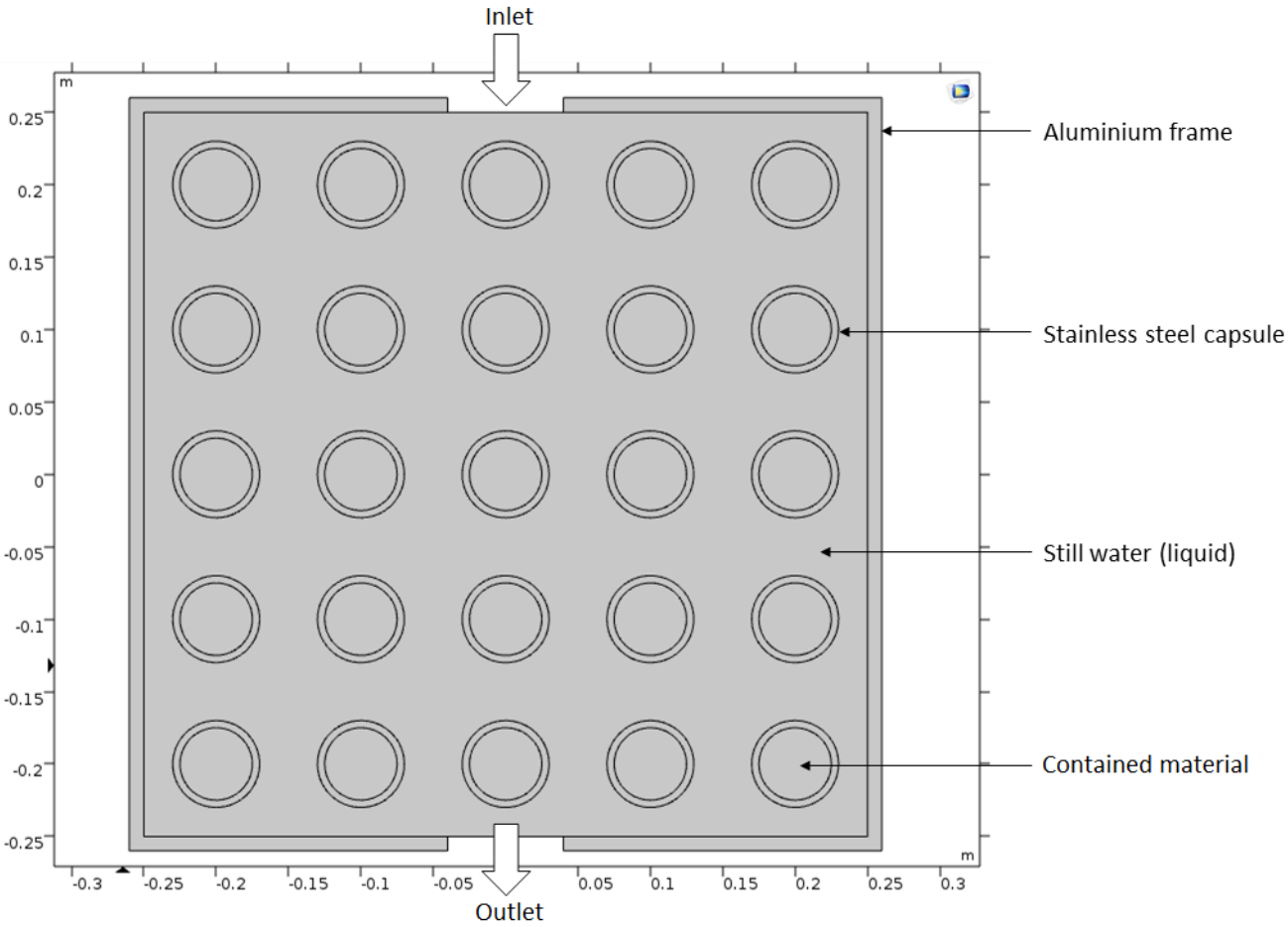

Figure 4.2: System modelled in COMSOL Multiphysics

Initially, the focus of these simulations resides in experimenting with different materials to find out which one absorbs most heat and which parameters accentuate this. The whole system is at

293.15K and is being heated up sensibly by water (heat transfer fluid) entering the inlet as laminar flow at a velocity of 0.1m/s at 363.15K. Therefore, the operating temperature is 293.15K to 363.15K. Phase-change and latent heat will be implemented at subsequent simulations.

The system was completely insulated outside the Aluminium frame, so no heat was lost into the environment. The areas which are insulated are denoted in blue in the figure below:

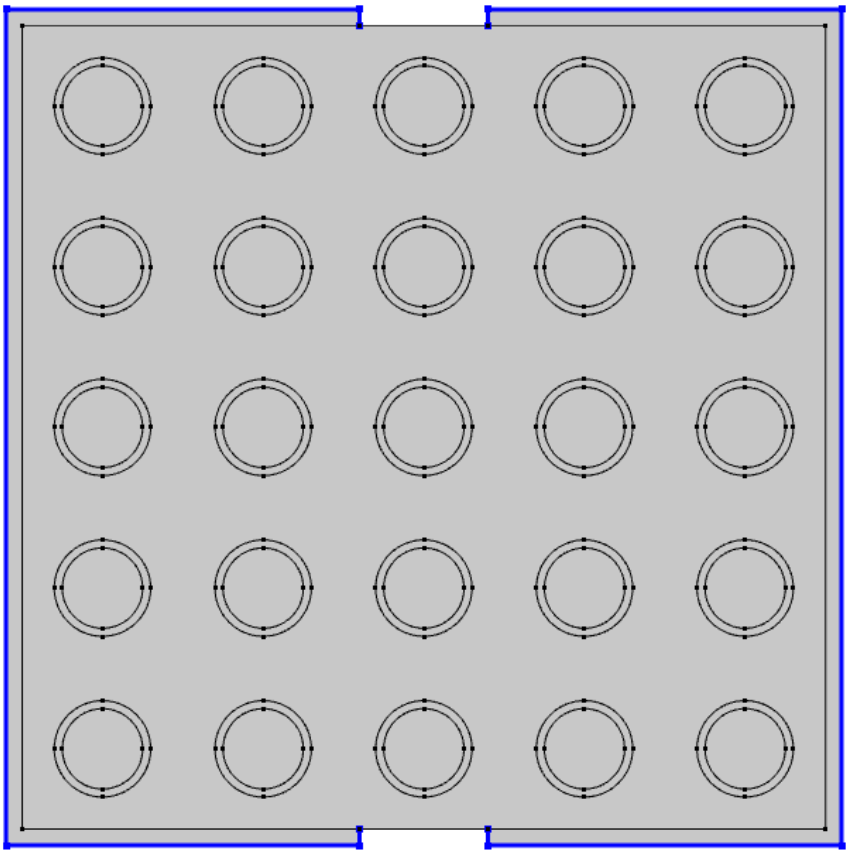

Figure 4.3: System clearly denoting the areas which are insulated (blue lines)

COMSOL Multiphysics uses solvers known as “Physics” to compute its solutions. At this initial stage, two Physics models were being used: “Heat transfer in fluids” and “Laminar Flow”.

For the first Physics model, the software requires the difference between what is solid and what is a fluid. COMSOL can gather the properties for each material and calculate the conjugate heat transfer if each boundary and domain was linked to the correct material accordingly. Further to this, once the temperature inlet and an outflow are set, COMSOL requires some initial conditions (initial temperatures). Figure 4.4 shows these:

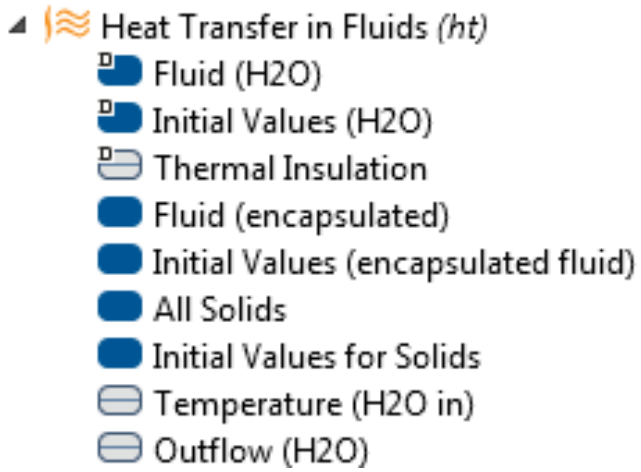

Figure 4.4: Heat transfer in fluids physics model used in the initial modelling

For the second Physics model, the software needs to know what the HTF is and what are its initial conditions, where the inlet and outlet are, and which boundaries are walls. The walls are set to no slip and have a tangential velocity of zero. The boundary condition at the inlet is set to velocity and at the outlet it is set to pressure that suppresses backflow. The fluid was set as incompressible flow and the overall system pressure was set to 1atm. More information in Table 4.1:

Table 4.1: Boundary conditions set for COMSOL simulations

Conditions	Value	Units
Initial Temperature	20 / 293	°C / K
Heat Transfer Fluid Temperature	90 / 363	°C / K
Simulation Time / Intervals	40 / 0.1	hours
Heat Transfer Fluid Velocity	0.1	m/s

Figure 4.5 shows the Laminar Physics setup:

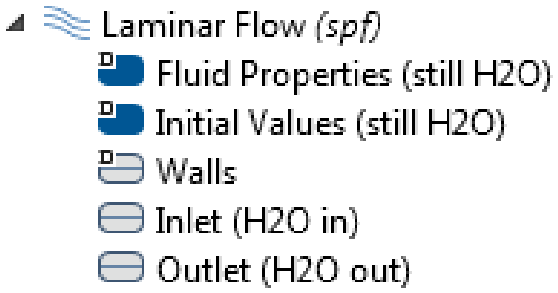

Figure 4.5: Laminar flow physics model used in the initial modelling

The mesh of the system was done automatically by COMSOL and set to extremely coarse, where the number of mesh elements were approximately 10,752 and mostly triangular prisms. Figure 4.6 below shows the mesh:

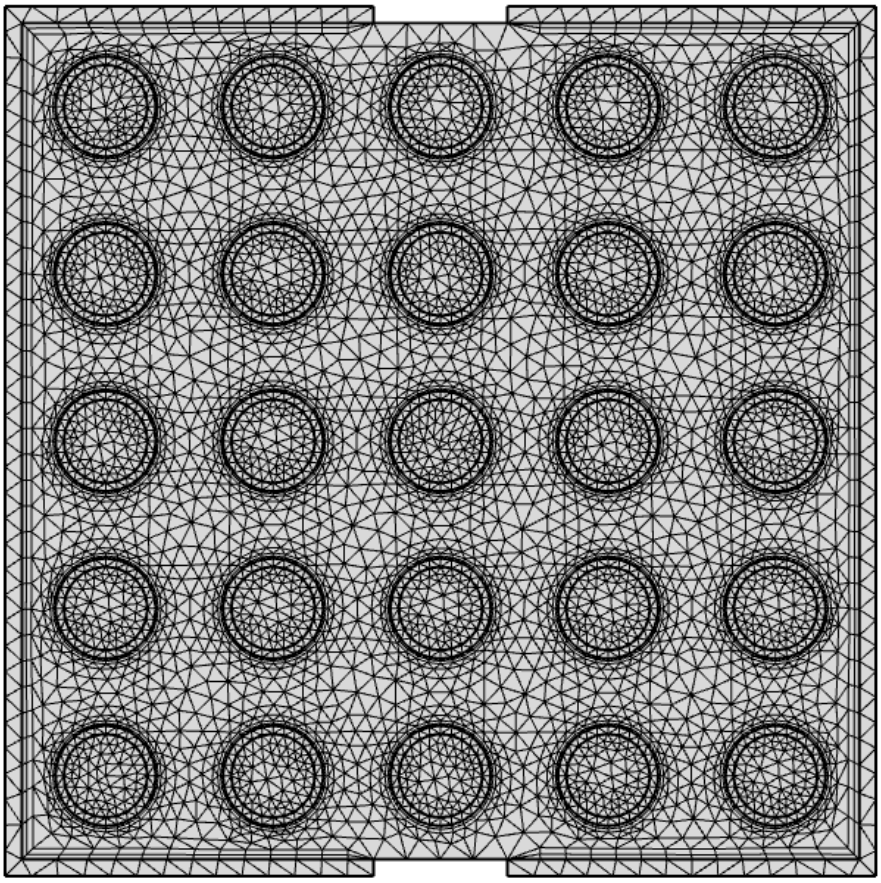

Figure 4.6: Mesh for the initial simulations

The heat transfer problem was solved numerically by COMSOL using the heat equation for non-uniform isotropic mediums and Fourier's law:

Equation 4.1: $\rho C_p \frac{\partial T}{\partial t} + \rho C_p u \cdot \nabla T + \nabla \cdot q = Q + Q_p + Q_{vd}$

Equation 4.2: $q = k \nabla T$

Where ρ is density, Cp is heat capacity at constant pressure, T is temperature, t is time, u is velocity, q is heat flux, Q is the heat source, Qp is heat pressure work, Qvd is heat viscous dissipation and k is thermal conductivity.

4.1.2 Materials and variables

The encapsulated material and its properties are the system's variable. The properties of the aluminium tank and frame, and the stainless-steel capsule remain the same for all tests and the properties were acquired from the COMSOL library (MatWeb, 2018) (MatWeb, 2018).

The selection process for the materials was based on their operating temperature range in the liquid phase and their suitability as low temperature sensible heat storage. In order to assess

different performances, the following nine were chosen: Water, Glycerol, Engine Oil, Transformer Oil, MDM, MD2M, MD3M, n-Hexadecane and Acetic Acid.

The properties were varied and covered a wide range. Water and Glycerol were different from the rest and had distinct specific heat capacity and thermal conductivity values. MDM, MD2M and MD3M had similar properties for density and specific heat and the intent was to see how those similarities affected the results. Engine Oil and Transformer Oil had the same density, yet different specific heat and thermal conductivity, which would help seeing what those parameters' effect is. N-Hexadecane had high specific heat capacity but poor density, as opposed to Glycerol. Acetic Acid had excellent density, but poor specific heat, as opposed to Water.

For all simulations, water was the HTF. Properties, taken at the average temperature of 55°C, can be found below in Table 4.2:

Table 4.2: Thermal properties of selected sensible heat materials taken at 55°C (Lemmon, Huber, & McLinden, 2018) (Glycerine-Producers-Association, 1963) (Bentilla et al.,1965) (T.M. Aminabhavi and B. Gopalkrishna,1994) (National Oceanic and Atmospheric Administration's Office of Response and Restoration,1999)(Hardy, 1958)

Storage Material	Specific Heat Capacity [kJ/kgK]	Density [kg/m3]	Thermal Conductivity [mW/mK]
Water	4.183	985.69	646.02
Glycerol	2.4262	1239.7	284.7
Engine Oil	2.100	888.00	147.0
Transformer Oil	1.860	880.00	370.0
MDM	1.8721	785.36	93.66
MD2M	1.7042	819.01	102.28
MD3M	1.7633	841.24	107.65
n-Hexadecane	2.110	776.00	125.00
Acetic Acid	1.203	1012.14	182.82

The simulation was running for 40 simulation hours at intervals of 0.1 hours. The temperature at the centre point for three spheres was recorded. These were coordinates (0,0) for the central sphere, coordinates (-0.2,0.2) for the top left sphere and coordinates (-0.2,-0.2) for the bottom left sphere. Since the design was symmetrical along the x-axis, the spheres at the right were assumed to have the same temperature profiles as those analysed.

4.2 Further Modelling (tank shape)

Three different designs have been simulated in COMSOL for the materials: no dome, 1 dome and 2 domes. The materials tested are now four: water, glycerol, MDM and MD3M. The focus now will reside primarily on the top and bottom spheres, as the centre one followed a different heating dynamic and is difficult to fit and compare due to the initial lag.

The three new designs can be seen below in Figure 4.7, where the red lines represent inlet/outlets for the HTF and the blue arrows represent the direction of flow.

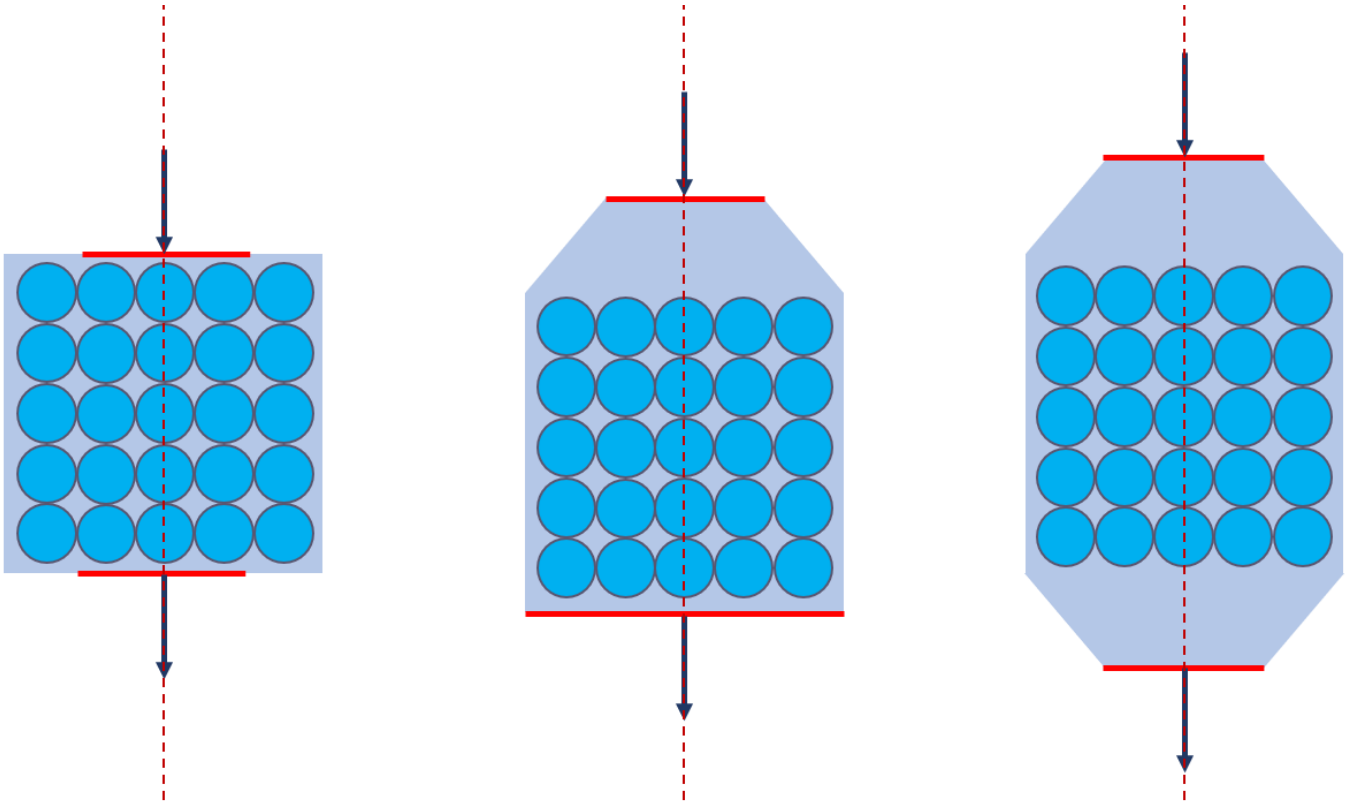

Figure 4.7: Three tank designs for the COMSOL simulations (not drawn to scale)

The results for the no dome simulations were analysed in the Section 5.1 (initial results). The three designs were simulated under the same conditions: initial temperature of 20°C, water inlet temperature of 90°C. Again, an array of 5x5 spheres with the same dimensions and the same encapsulation material. The red lines are 0.16m in size except for the outlet in design with 1 dome, where the outlet is the diameter of the tank, i.e. 0.5m.

The simulation ran for 40h and the final temperatures at the centre of three spheres (in three different positions) were recorded. This time the right side was used, as opposed to the left side in the no dome design, the coordinates were (0.2,0.2), (0,0) and (0.2,-0.2). These correspond to top right, centre and bottom right spheres, respectively.

4.3 Further Modelling (latent heat)

After modelling several materials that were heated up sensibly, the main focus of the study shifted to PCMs and latent heating. This coincided with the newly released version of COMSOL Multiphysics 5.4, which featured new content and a friendlier user interface. Therefore, the new version was used in further analysing the upcoming results. Version 5.4 offered more software stability and less errors compared to the previous one. This has not led to any changes in the results.

4.3.1 System Design and Boundary

The system consists of the same symmetrical and cylindrical tank of 0.5m in height and length, with the same 0.025m tank frame thickness. Nevertheless, this time it is packed with a set of 19x17 encapsulated spheres containing the selected PCM. These smaller spheres, with a radius of 0.0125m, are assumed to have a thin outer coating holding the PCM together that acts as a capsule which has negligible thickness. The ambient temperature, inlet temperature and boundary conditions remain the same, except this time the velocity at the inlet varies. The inlet velocities studied were 0.1m/s, 0.05m/s and 0.01m/s.

Since the effect of the dome was small and lengthened the simulation time, for this section, domes were excluded from the study. The two designs, named A and B, have different inlets but the same outlet. Design A is the same as the first design in Figure 4.7 at section 4.2. Design B consists of two inlets and a single outlet, all with dimensions 0.12m.

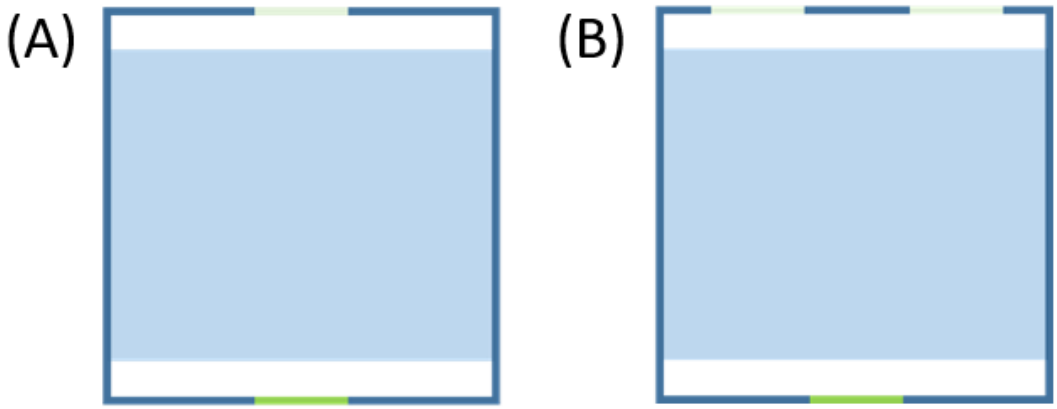

Figure 4.8: Two design types which are analysed

The temperature will be monitored at the same three selected positions which include the top left, bottom left and centre sphere, in a similar arrangement to the previous initial results.

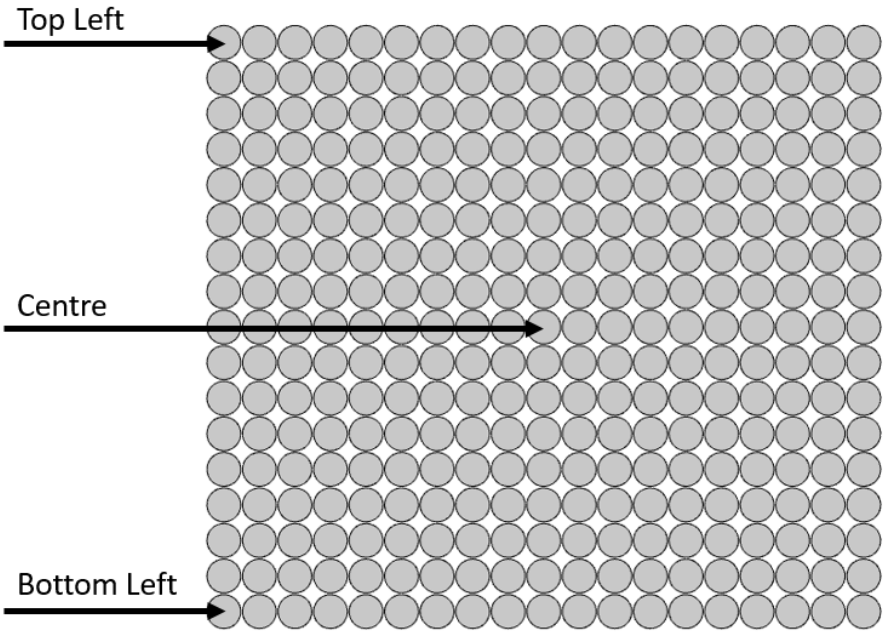

Figure 4.9: New system positions and PCM arrangement where the temperature will be recorded

The 2D simulation is run in COMSOL Multiphysics for 5 simulation minutes at 1 second intervals. The model uses the "Laminar Flow" and "Heat Transfer in Fluids" physics, alongside the addition of the "Nonisothermal Flow" multi-physics. The mesh was approximately 140,000 mesh elements, mostly triangular prisms. The heat transfer problem was again solved using the heat equation for non-uniform isotropic mediums (Equation 4.1) and Fourier's law (Equation 4.2).

4.3.2 Selected PCMs

The focus for the material testing remained on paraffins and fatty acids, mainly for their low melting points which and their suitability as low temperature storage mediums. The three selected materials are listed with their relevant properties in Table 4.3:

Table 4.3: Selected PCMs and their relevant properties (Fang, Lin and Alva,2017)

Phase Changing Material (PCM)	Melting point (Tm) [°C]	Transition interval between phase 1 and 2 (Tint) [K]	Latent Heat of Fusion (L) [kJ/kg]	Density Solid / Liquid (ρ_s/ρ_l) [kg/m3]	Thermal Conductivity Solid / Liquid (k_s/k_l) [W/mK]	Specific Heat Capacity Solid / Liquid (c_{ps}/c_{pl}) [J/kgK]
Paraffin Wax	55.55	8.7	190.0	825/755	0.230/0.200	2200/2100
nOctadecane	25.10	1.4	243.5	776/776	0.358/0.130	1934/2196
Capric Acid	31.85	1.8	152.7	878/878	0.372/0.141	475.59/475.59

4.4 Final Model – Material Construction

4.4.1 Gap and Revised Aim

While analysing the results, it was very difficult to determine the extent to which material properties were influencing the performance of the system in terms of the outputs. The gap in research was that there is no clear literature on how thermal parameters quantitatively affect the system outputs. Therefore, the idea of constructing a "perfect" material catered to the system using "user-defined" phase changing materials arose.

The revised aim of this study is, therefore, to assess the suitability and relevance of thermal parameters using user defined phase changing materials (PCM) to be implemented into encapsulated spheres in a packed bed, in a square and single tank design. These PCM still consisted of solid to liquid and were encapsulated, except for in these simulations, the capsule holding the PCM together was a theoretical membrane with no material assigned with negligible thickness.

4.4.2 Tested Cases

For these series of tests, Design (A) from Figure 4.8 from section 4.3.1 was used. From the three velocities evaluated before, the lowest velocity was selected (v = 0.01m/s). All other parameters, such as inlet temperature, system boundaries, physics modules, HTF temperature, etc. were kept the same. The simulation time was 60 minutes, with 1minute intervals.

In order to determine how material properties dictated the system outputs, a base case with fixed thermal parameters was created. From here, one material property was varied at a time, whilst all the others remained fixed. These variations were based on existing materials (such as paraffin) and values previously reported by multiple authors in literature. The varying parameters for the material construction were melting temperature, latent heat and specific heat capacity (solid and liquid), density and thermal conductivity (solid and liquid).

Material codes were given to every case to help keep track of the simulations. The base case was given the code "C1" and had the following parameters:

- Melting temperature: 45°C
- Latent heat: 200 kJ/kg
- Density: 800 kg/m3
- Thermal conductivity:
    - Solid: 0.4 W/mK // Liquid: 0.2 W/mK
- Specific Heat Capacity:
    - Solid: 2000 J/kgK // Liquid: 2200 J/kgK

The other variations were given codes too, found in the following tables:

Table 4.4: Material codes and their relevant properties

Material Code	Melting point (Tm) [°C]	Density (ρ) [kg/m3]	Latent Heat of Fusion (L) [kJ/kg]
CL1	45	800	10
CL2	45	800	500
CTM1	25	800	200
CTM2	65	800	200
CD1	45	600	200
CD2	45	1000	200
CE1	45	600	10
CE2	45	1000	10
CE3	45	600	500
CE4	45	1000	500

Table 4.5: Material codes for specific heat capacity combinations only

Material Code	Specific Heat Capacity Solid (c_{ps}) [J/kgK]	Specific Heat Capacity Liquid (c_{pl}) [J/kgK]
CCP1	1000	2200
CCP2	2200	1000
CCP3	2000	2000
CCP4	2000	1000
CCP5	2200	2200
CCP6	1000	1000
CCP7	2200	2000

Table 4.6: Material codes for thermal conductivity combinations only

Material Code	Thermal Conductivity (k_s) [W/mK]	Thermal Conductivity (k_l) [W/mK]
CK1	0.2	0.2
CK2	0.4	0.4
CK3	0.2	0.1
CK4	0.2	0.4
CK5	0.1	0.2
CK6	0.1	0.1
CK7	0.1	0.4
CK8	0.4	0.1
CK9	0.3	0.3
CK10	0.2	0.3
CK11	0.3	0.2

4.5 Model Validations

4.5.1 Latent heat validation

The latent heat model validation was carried out using the paper by Tay et al. (2015) which focuses on a single tank latent heat 2D system. It is a symmetrical tank of dimensions: 0.15m x 1m, with an inner pipe carrying the HTF (Therminol VP1) of diameter 12.70mm and length of 1m. The PCM is a stationary $NaNO_3$ and it wraps around the pipe with diameter of 0.15m and length of 1m, shown in Figure 4.10.

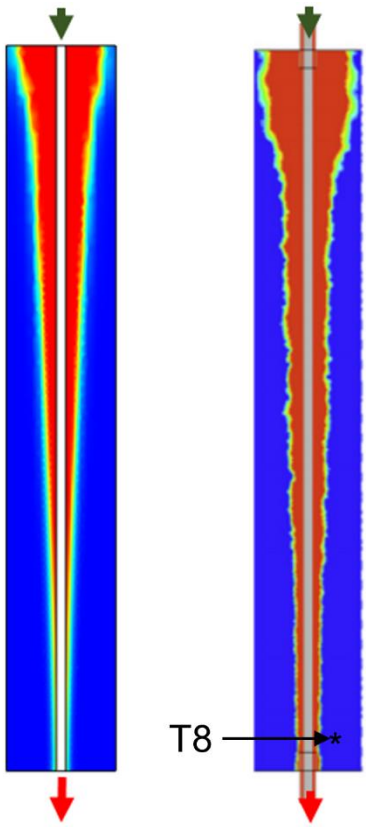

Figure 4.10: This study' results vs the original paper results thermal profile at time 10 hours

The system starts off at an initial temperature of 250°C, and the Therminol VP1 enters the top of the pipe at a mass flow rate of 0.01kg/s, at a temperature of 350°C. The simulation time was 40h and the time intervals were 0.1h.

The original paper had some points throughout the length of the tank where the temperature was going to be extracted. The point selected for the validation was T8 (see in Figure 4.10), and the same model was run in 2D in Comsol Multiphysics. The following graph shows a comparison of this study's results vs the original paper's results.

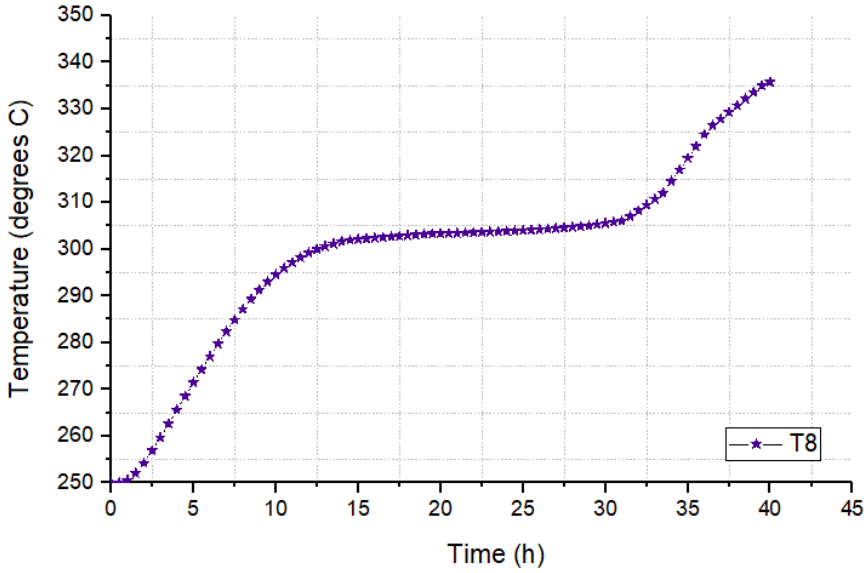

Figure 4.11: This study's results of the temperature vs time

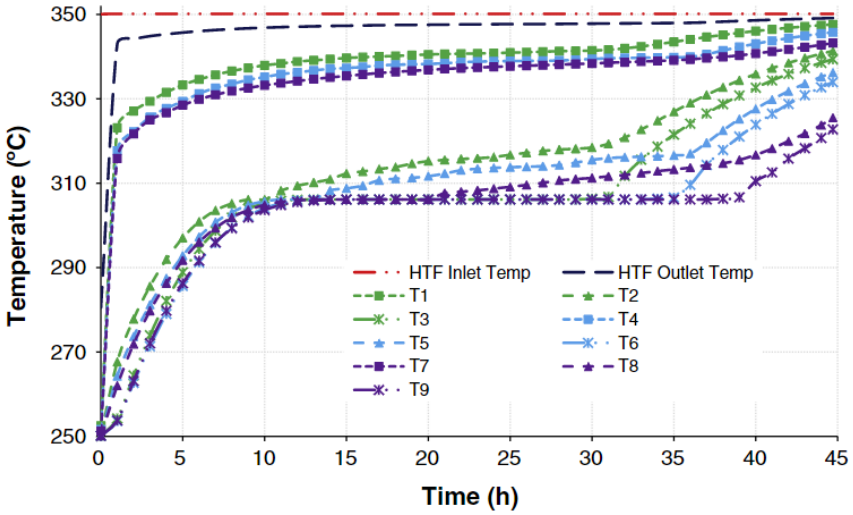

Figure 4.12: The Author paper's results of the temperature vs time

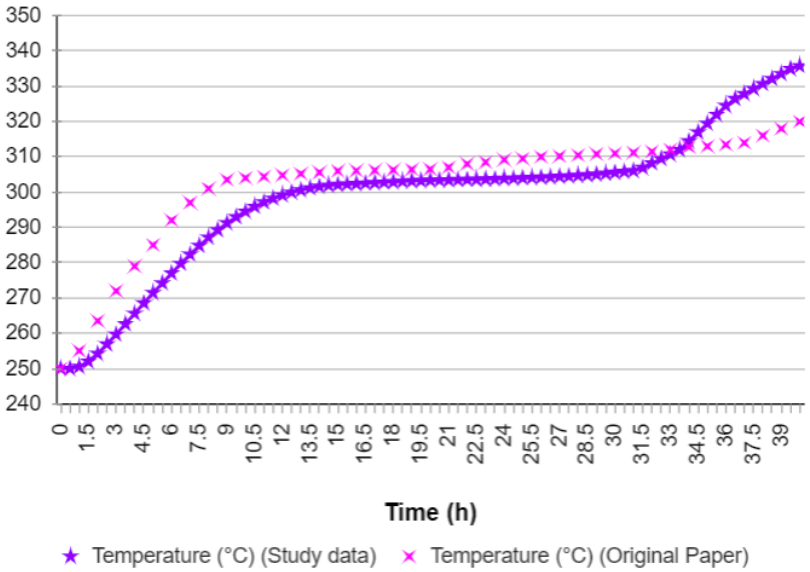

Figure 4.13: Superimposed image of both this paper and Author paper's results

It is seen that the shape and heating dynamics are the same and follow the normal phase change trend. Up to point t = 10h, thermal profile follows the same heating pattern and reaching just below the original peak, demonstrating that the results are in good agreeance with the published data and confirming the expected latent heat transfer behavior. However, there is some dissonance in the furthest part towards the end of the graph, where the results produced differ and follow a pattern more similar to point T2. This is probably due to the fact that in our system, the heat absorption and phase change indicated by the horizontal line was shorter, quicker melting process, which in turn sped up the second phase of sensible heating of the liquid part. Overall, our model captures the dynamics and extent of the full heating process well.

4.5.2 Sensible heat validation

The sensible heat model validation was validated based on numerical results from Elouali et al. (2019) for a 2D single tank packed bed. They test four different models: single phase model, continuous solid model, Schumann's model and model with thermal gradient within the solid particles. The validated model for this study is the single phase model which works well when considering the porous media as a homogeneous system. This numerical work is verified on the experimental and physical data by Meier et al. (1991).

The tank is spherical and has a height of 1.2m, a diameter of 0.148m, a sphere particle diameter of 0.02m and a ratio of the tank diameter to solid particles diameter of 7.4. The bed porosity was a value of 0.4. The storage materials are rock pebbles at an initial temperature of 20°C and the HTF is air, entering the system from the top of the tank (h = 1.2m) at a temperature of 550°C with a mass flow rate of 0.112 kg/s. The charging time was a total of 3 hours, and the simulation ran at 0.1h time intervals.

The full tank and mesh from the Comsol experiment are presented in Figure 4.14.

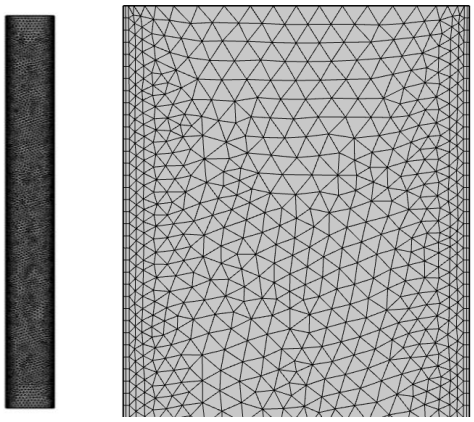

Figure 4.14: Comsol generated mesh of simulated tank for model validation (zoom out and zoom in)

Figure 4.15 below shows the temperature vs height of the system during charging for 3h. The Comsol data (solid lines) are in excellent agreement with experimentally reported values, especially at shorter time-scales. Simulation results slightly overestimated the temperatures reached across the pebble bed, but modestly so, no more than 15°C (roughly 5%).

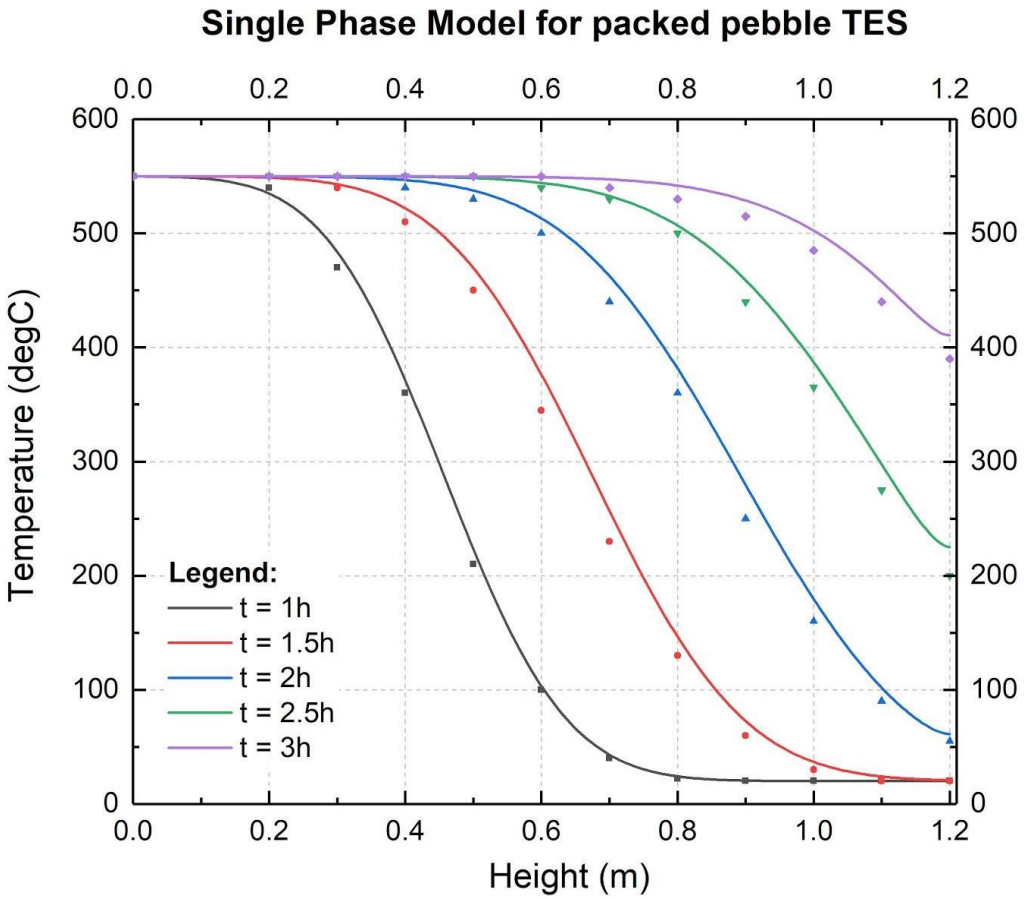

Figure 4.15: Comparison of this paper's results (solid lines) against single phase validated model (Elouali et al., 2019)

4.5.3 Mesh validation

The quality of the mesh for all results presented in this thesis was verified. For all tests, the mesh quality was set to "fine", which allowed the number of mesh elements to be automated by the software COMSOL, which depended on the physics modules selected. All mesh validations proved that the fine mesh quality was sufficiently accurate since increasing it only changed the value of the temperature by a value of less than 1K, and that any further accuracy unnecessarily increased the simulation time.

Furthermore, the sensitivity of the time intervals chosen for all models did not affect the sensitivity of the temperature results. Simulations were ran at different time intervals and the temperature results were the same or similar to less than 1K.

4.6 References for this section:

A. Elouali, T. Kousksou, T. El Rhafiki, S. Hamdaoui, M. Mahdaoui, A. Allouhi, Y. Zeraouli. (2019). Physical models for packed bed: Sensible heat storage systems. *Journal of Energy Storage*, *23*, 69-78. doi: 10.1016/j.est.2019.03.004

E.W. Bentilla and A. Shlosinger. (1965). Research and development study on thermal control by use of fusible materials - Interim report. NASA Technical Reports Server. url: https://ntrs.nasa.gov/citations/19660001339

E. W. Lemmon and and Ian H. Bell and M. L. Huber and M. O. McLinden. (2018). NIST Standard Reference Database 23: Reference Fluid Thermodynamic and Transport Properties-REFPROP, Version 10.0, National Institute of Standards and Technology. doi: https://doi.org/10.18434/T4/1502528. url:https://www.nist.gov/srd/refprop

Fang, G., Lin, Y., & Alva, G. (2017). An overview of thermal energy storage systems. Energy, 144, 341-378. doi: 10.1016/j.energy.2017.12.037

Glycerine-Producers-Association. (1963). *Physical properties of glycerine and its solutions*. New York: Glycerine Producers' Association.

Hardy C.R. (1958). Viscosity of n-Hexadecane. Journal of Research of the National Bureau of Standards 61, 433-436.

MatWeb. (2018, October 1). *MatWeb Material Property Data*. Retrieved from Aluminium, Al, Properties: http://www.matweb.com/search/DataSheet.aspx?MatGUID=0cd1edf33ac145ee93a0aa6fc666c0e0

MatWeb. (2018, October 1). MatWeb Material Property Data. Retrieved from 304 Stainless Steel, Properties: http://www.matweb.com/search/datasheet.aspx?MatGUID=abc4415b0f8b490387e3c922237098da

Meier A., Winkler C., Wuillemin D. (1991). Experiment for modelling high temperature rock bed storage. Solar Energy Materials 24, 255-264. doi: 10.1016/0165-1633(91)90066-T

National Oceanic and Atmospheric Administration's Office of Response and Restoration (1999). Acetic Acid Information. CAMEO Chemicals version 2.7.1. url: https://cameochemicals.noaa.gov/chris/AAC.pdf

N.H.S. Tay, M. Belusko, M. Liu, F. Bruno (2015). Investigation of the effect of dynamic melting in a tube-in-tank PCM system using a CFD model. Applied Energy 137, 738-747. doi: 10.1016/j.apenergy.2014.06.060

T.M. Aminabhavi, B. Gopalkrishna (1994). Densities, Viscosities, Refractive Indices, and Speeds of Sound of the Binary Mixtures of Bis-(2-methoxyethyl) Ether with Nonane, Decane,

Dodecane, Tetradecane, and Hexadecane at 298.15, 308.15, and 318.15 K. *Journal of Chememical Engineering 39*, 529-534. doi: 10.1021/je00015a029

V. Sensible Heat Results

5.1 Initial Results

The output temperature data from COMSOL was collected, specifically the final temperatures after 40 simulation hours for the nine materials initially analysed. These are presented in Table 5.1:

Table 5.1: Final temperatures recorded after 40h using COMSOL

Material	Final Temperature (K)
Water	336.97
Glycerol	338.03
Engine Oil	340.20
Transformer Oil	340.31
MDM	340.57
MD2M	340.78
MD3M	343.73
n-Hexadecane	340.47
Acetic-Acid	343.61

Further analysis was done on a reduced number of materials. This made it easier to relate the results and any trends to specific material thermal properties. The relevant properties for each material studied are in Table 5.2. The selection was made based on thermal properties.

Again, each value was taken at the average temperature of 328.15K (55°C) and 1atm pressure. Using the output temperature data from COMSOL, the heat absorbed by one sphere was approximately calculated for each different position after the established time frame. These are provided in Table 5.4.

Table 5.2: Properties for the tested materials taken at a reference temperature of 55°C (Lemmon, Huber, & McLinden, 2018) (Glycerine-Producers-Association, 1963)

Material	Specific Heat Capacity (kJ/kg·K)	Density (kg/m^3)	Dynamic Viscosity (µPa·s)	Kinematic Viscosity (µPa·s)	Thermal Conductivity (cm^2/s)	Thermal Diffusivity (m^2/s)
Water	4.1830	985.69	503.62	0.005109	646.02	0.00156680
Glycerol	2.4262	1239.70	108740.00	0.877400	284.70	0.09465515
MDM	1.8721	785.36	575.73	0.007331	93.66	0.00063704
MD2M	1.7042	819.01	870.42	0.010628	102.28	0.00073276
MD3M	1.7633	841.24	1178.50	0.014010	107.65	0.00072575

Table 5.3: Key for the colours presented in Table 5.4

Key		Colour
Least Heat Absorbed	Lowest Temperature	
↓	↓	
Most Heat Absorbed	Highest Temperature	

Table 5.4: Heat absorbed and final temperature after 40h of simulation for three different points for five materials

	Middle Sphere (0,0)		Top Left Sphere (-0.2,0.2)		Bottom Left Sphere (-0.2,-0.2)	
Material	**Final Temperature (K)**	**Heat Absorbed (kJ)**	**Final Temperature (K)**	**Heat Absorbed (kJ)**	**Final Temperature (K)**	**Heat Absorbed (kJ)**
Water	336.97	11.8252	355.21	16.7474	345.82	14.2135
Glycerol	338.03	8.8350	355.43	12.2603	346.36	10.4748
MDM	340.57	4.5632	356.36	6.0826	348.34	5.3109
MD2M	340.78	4.3511	356.43	5.7808	348.47	5.0536
MD3M	343.73	4.9106	357.30	6.2280	350.37	5.5552

The heat absorbed was calculated using equation:

Equation 5.1: $$Q = cp \cdot m\,(T_{final} - T_{initial})$$

5.2 Discussion

5.1.2 Materials

From the information collected above, the following data can be extracted:

- MD3M reaches the highest final temperature (336.97K)
- Water reaches the lowest final temperature (336.97K)
- Water absorbs the highest amount of heat (11.83kJ)
- MD2M absorbs the lowest amount of heat (4.35kJ)
- Water has the largest specific heat capacity (4.1830 J/kg·K)
- MD2M has the lowest specific heat capacity (1.7042 J/kg·K)
- Glycerol has the highest density (1239.70 kg/m^3)
- MDM has the lowest density (785.36 kg/m^3)

This information is consistent across the tank, as the three different points in space taken for the analysis share this result. This suggests that the density and c_p are determining factors in the heat absorption, as glycerol and water have great heat absorption per sphere.

Further to this, for MDM to MD3M demonstrate that there is a trade-off between which one of these two properties is more dominant over the heat absorption. MDM has the highest c_p, but lowest density of the three, yet achieves an average heat absorption. MD2M has the lowest c_p and an average density of the three, yet it has the lowest heat absorption. MD3M has an average c_p, but the highest density of the three and lastly, the highest heat absorption. The differences between materials in percentages was collected in Table 5.5, where again red is lowest and green is highest:

Table 5.5: Percentage differences between the MDM, MD2M and MD3M

Materials	Specific Heat Capacity differences	Materials	Density differences
MDM - MD2M	8.97%	MD2M - MDM	4.11%
MDM - MD3M	5.81%	MD3M - MDM	6.64%
MD3M - MD2M	3.35%	MD3M – MD2M	2.64%

Since the c_p difference MDM and MD2M is much larger (8.97%) than the density difference (4.11%), this suggests that c_p was much more of an influential factor than density. On the other hand, between MD3M and MDM, the density difference (6.64%) is larger than the c_p difference, meaning the density was the highest influence and therefore allowing MD3M to absorb the largest amount of heat.

The same analysis with the cp and densities using MDM, MD2M and MD3M suggests the c_p of the substance does not influence the charging speed as the final temperatures do not follow a pattern. Other relevant parameters, such as dynamic viscosity, kinematic viscosity, thermal conductivity and thermal diffusivity do not have a discernible pattern and do not impact the final temperature and heat absorption.

5.1.3 Positions

To understand better how heat distribution throughout the tank, three different spheres were analysed for all five materials. The top sphere was closest to the inlet of the HTF and absorbed the most heat and reached the highest final temperature. The bottom sphere followed, leaving the centre sphere last. The centre sphere had poor heat absorption and the lowest final temperature.

Temperature versus time graphs were plotted in the software OriginPro for the five materials in order to see the temperature profiles and the charging dynamics for each one. These can be found below as Figures 5.1 – 5.3:

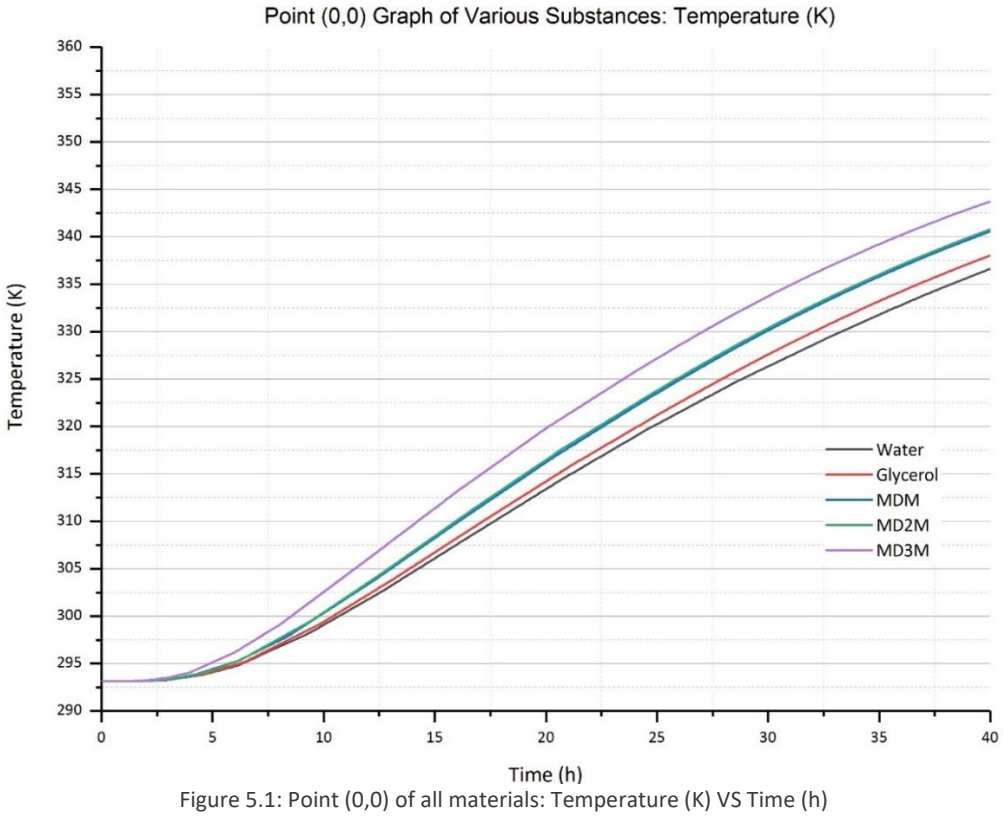

Figure 5.1: Point (0,0) of all materials: Temperature (K) VS Time (h)

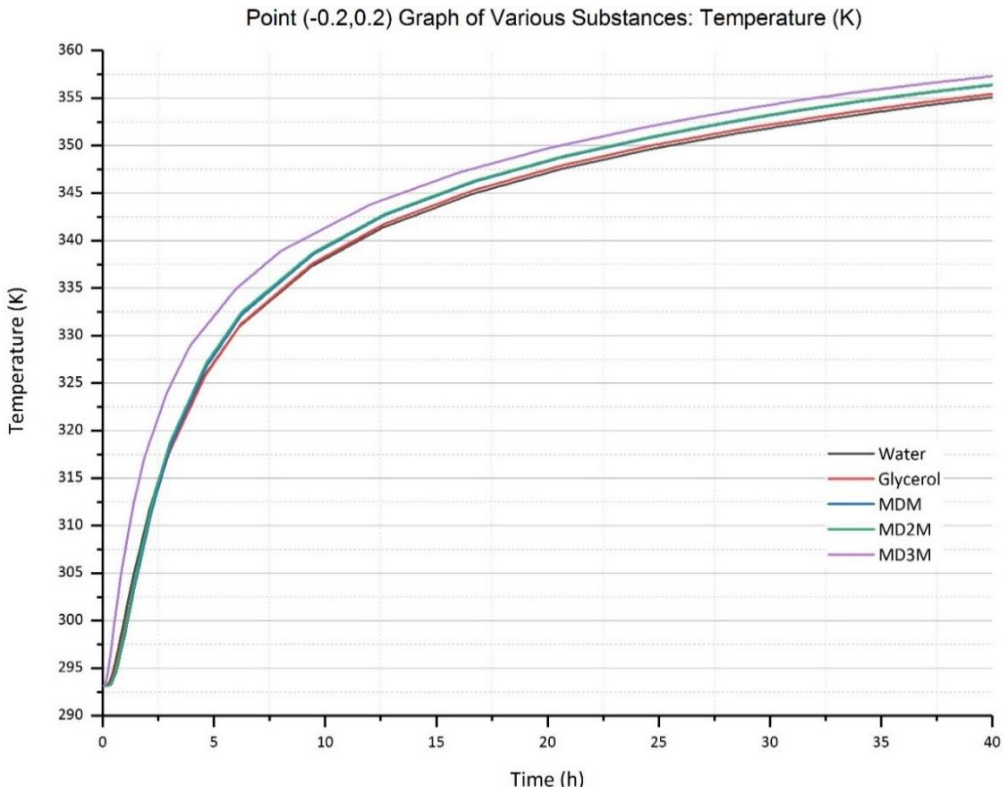

Figure 5.2: Point (-0.2,0.2) of all materials: Temperature (K) VS Time (h)

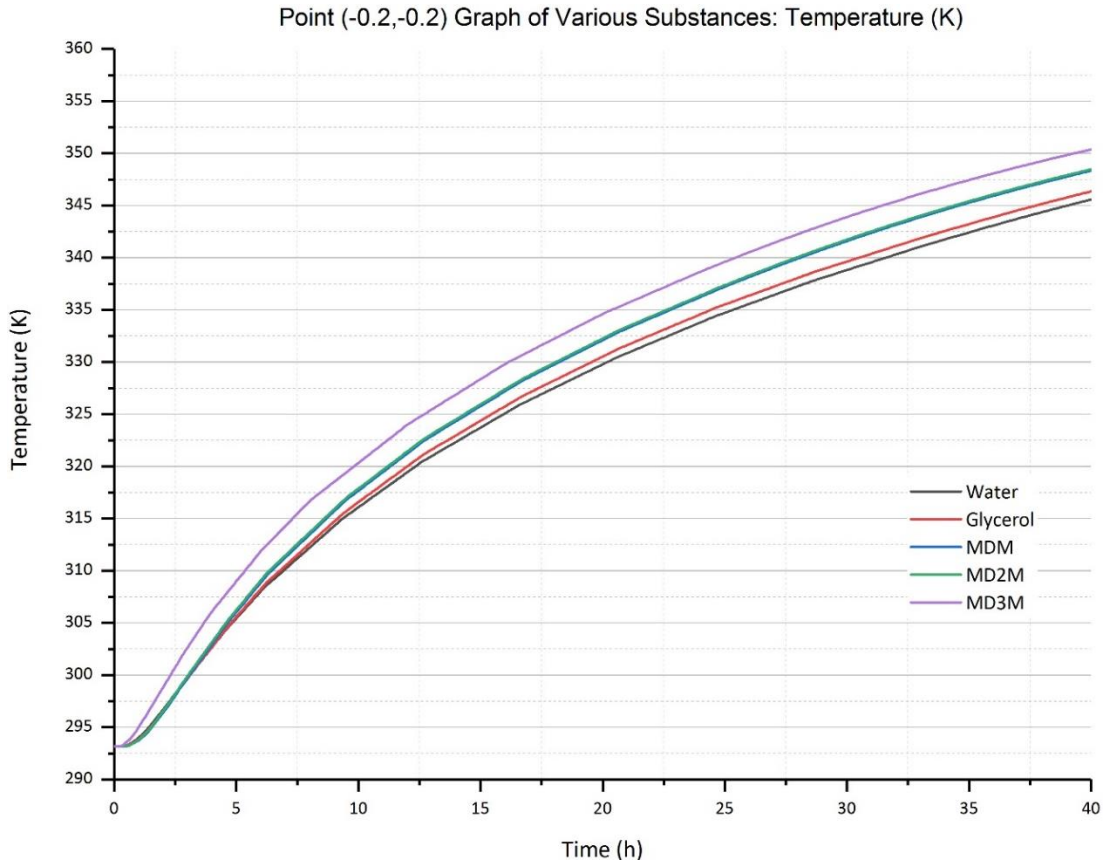

Figure 5.3: Point (-0.2,-0.2) of all materials: Temperature (K) VS Time (h)

The gradient and charging dynamics of the top sphere are much faster than the other two. The top sphere curves to approach the final temperature at approximately 15h, whereas the bottom and centre sphere have a slower approach and gently climb towards the final temperature. On top of that, the centre sphere has an initial lag of approximately 5h. Even though the HTF took longer to reach the bottom sphere than the centre sphere, it heated up faster and was able to absorb more heat. This could be due to the fact that there is some recirculation in the tank and that inlet and outlet are positioned in the centre of the tank, not permitting the fast flowing HTF enough contact time to allow an effective heat transfer.

Since the differences between the three spheres are significantly large, the exact percentages were calculated and put into Table 5.6.

Table 5.6: Percentage difference for final temperature and heat absorption for three positions

	Percentage difference (Temperature)			**Percentage difference (Heat Absorbed)**		
Material	**(-0.2,0.2) & (0,0)**	**(-0.2,0.2) & (-0.2,-0.2)**	**(0,0) & (-0.2,-0.2)**	**(-0.2,0.2) & (0,0)**	**(-0.2,0.2) & (-0.2,-0.2)**	**(0,0) & (-0.2,-0.2)**
Water	5.13%	2.64%	2.56%	29.39%	15.13%	16.80%
Glycerol	4.90%	2.55%	2.41%	27.94%	14.56%	15.65%
MDM	4.43%	2.25%	2.23%	24.98%	12.69%	14.08%
MD2M	4.39%	2.23%	2.21%	24.73%	12.58%	13.90%
MD3M	3.80%	1.94%	1.90%	21.15%	10.80%	11.60%

The temperature differences are moderate, the highest difference being 5% and the lowest 2% (approximately). Nevertheless, the differences between the heat absorption from the best performing and the worst performing is extremely large. On average, 25% more heat is absorbed by the top sphere which is very significant to the performance of the storage system.

This calls for further exploration of the tank design and finding an effective way of fixing this disproportion in the heat absorption between the spheres.

5.3 Final Temperature and Heat Absorbed

Once the results were compiled, again temperature versus time graphs were plotted in the software OriginPro for the four materials in order to see the temperature profiles and the charging dynamics for each one. These can be found below as Figures 5.4 – 5.7:

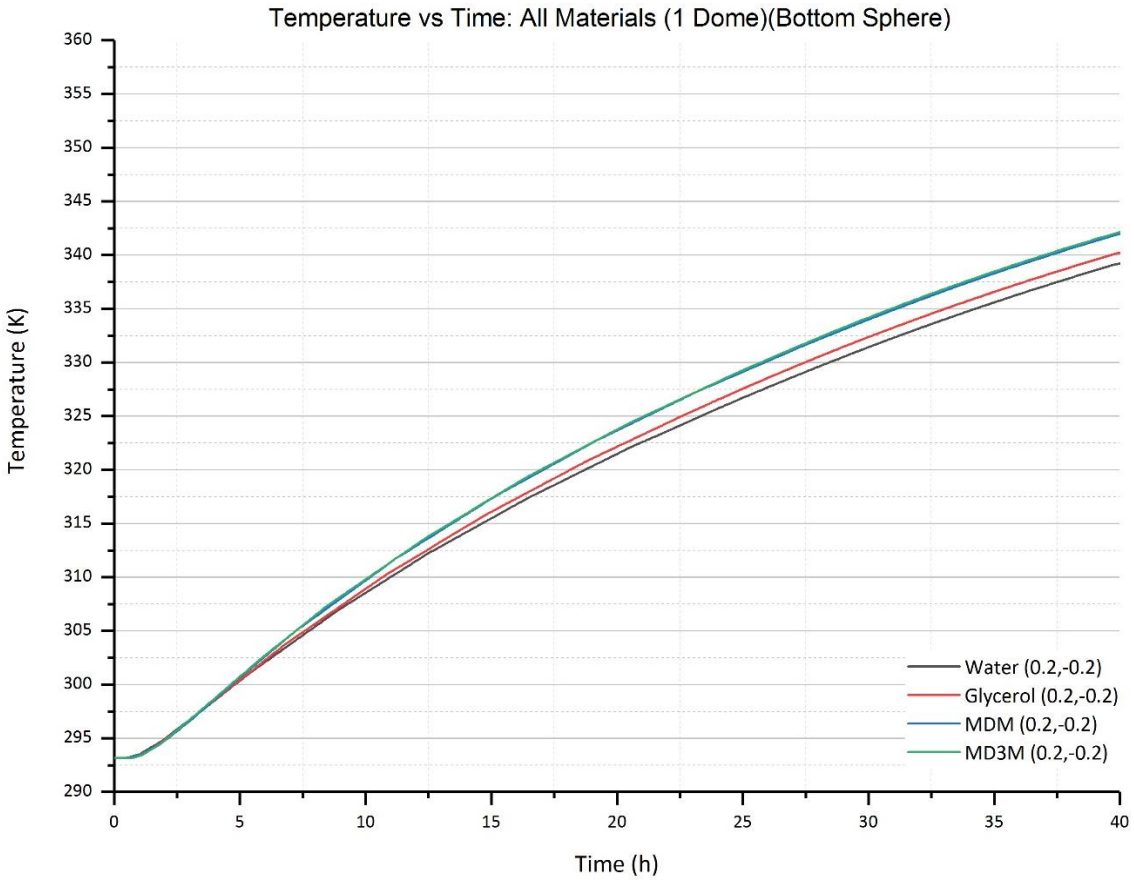

Figure 5.4: Temperature (K) vs time (h) graph for all materials, 1 dome, bottom sphere

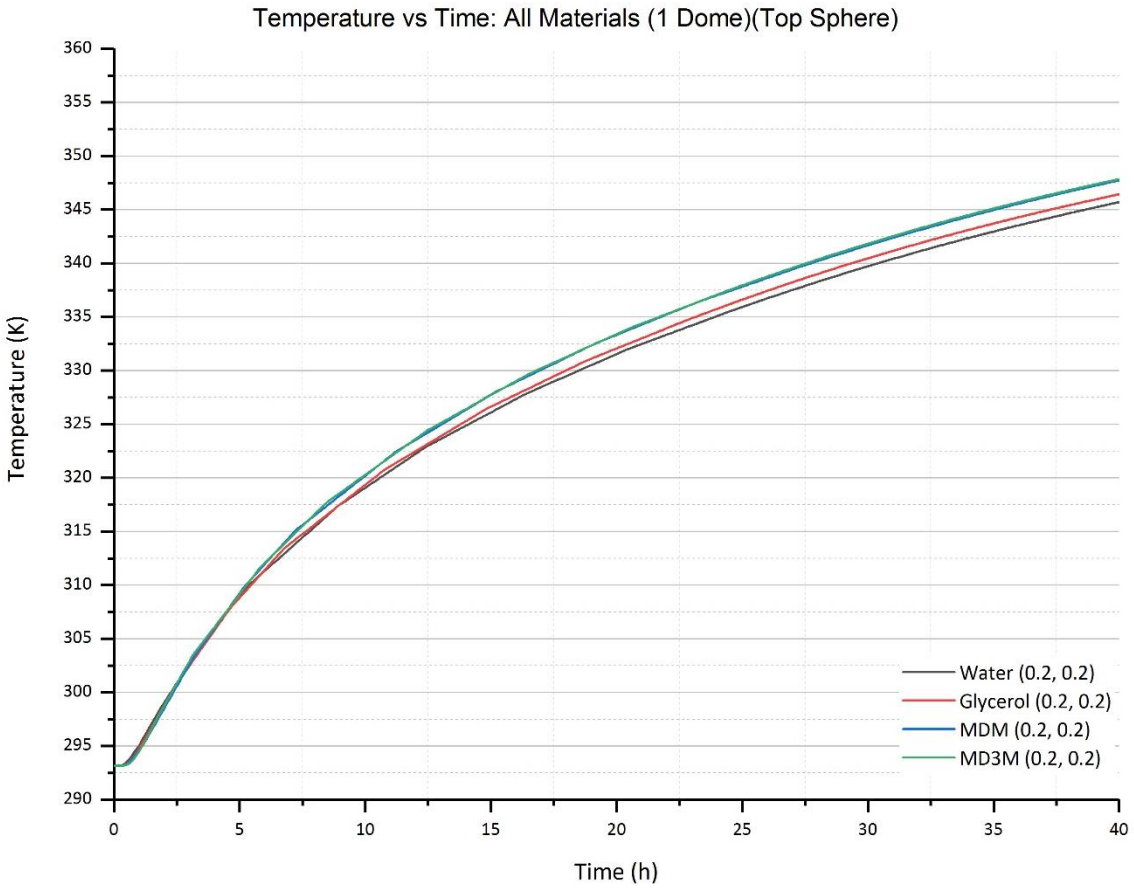

Figure 5.5: Temperature (K) vs time (h) graph for all materials, 1 dome, top sphere

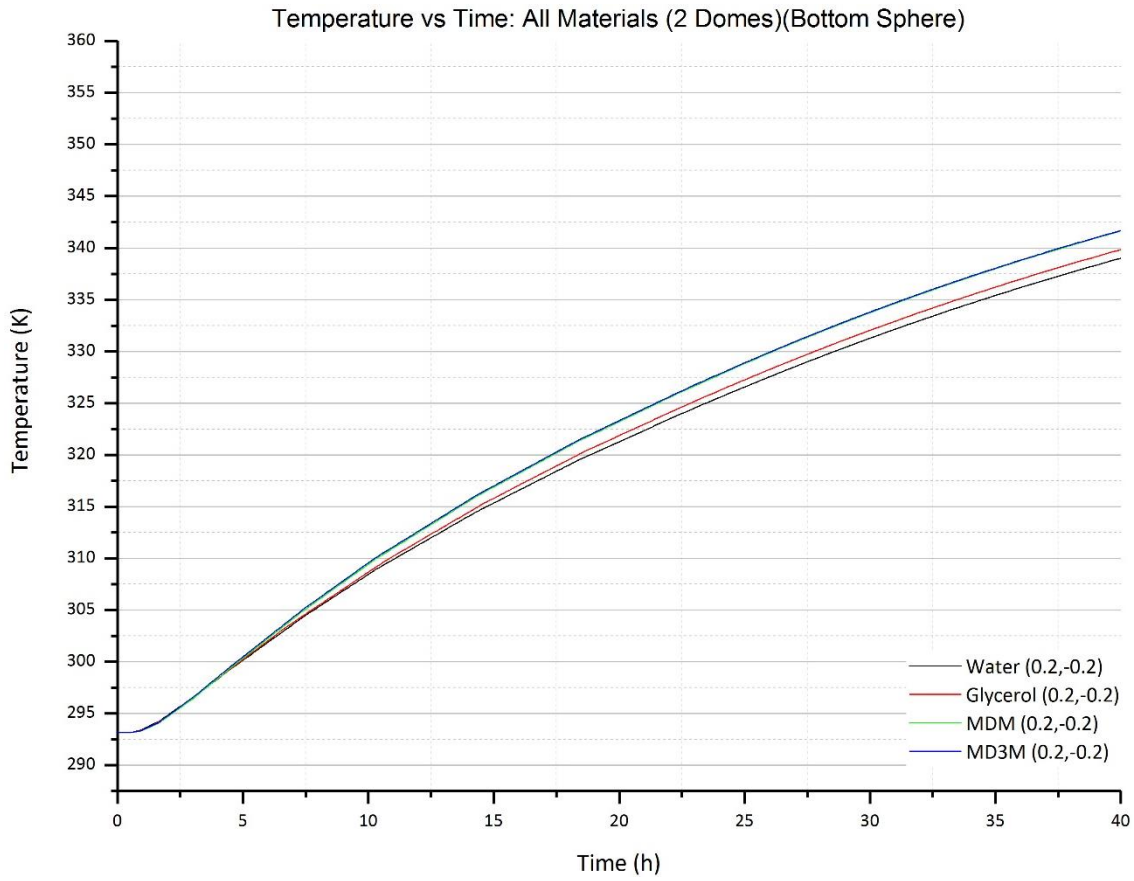

Figure 5.6: Temperature (K) vs time (h) graph for all materials, 2 domes, bottom sphere

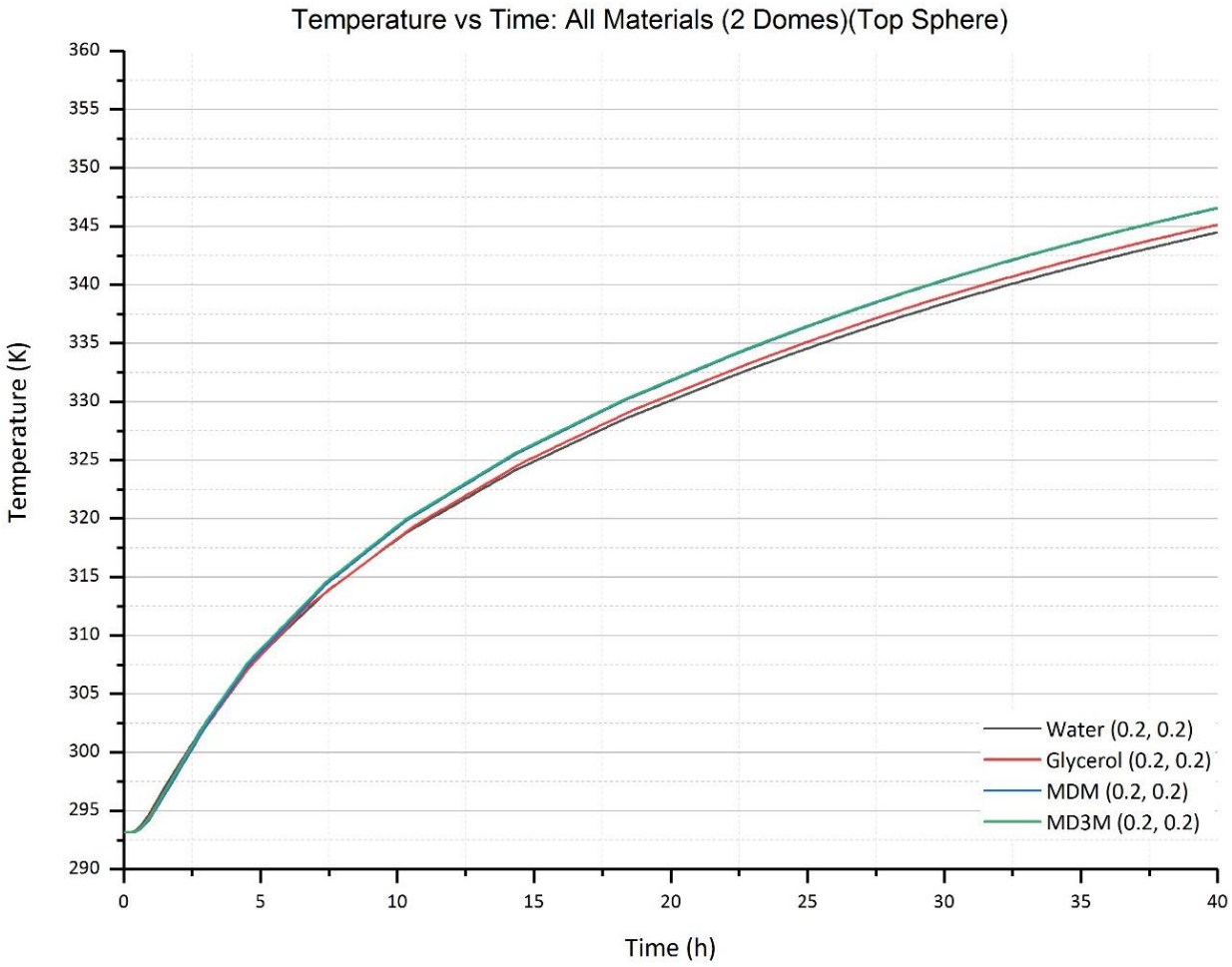

Figure 5.7: Temperature (K) vs time (h) graph for all materials, 2 domes, top sphere

As mentioned above, the analysis is now limited to the top and bottom spheres. The final temperatures and heat absorbed values for the three tank designs, for two positions for four materials are shown in Table 5.7 and Table 5.8:

Table 5.7: Final temperatures and heat absorption values for all three designs, two positions and four materials

	Top Spheres					
	No Dome		1 Dome		2 Domes	
Material	Final Temperature (K)	Heat Absorbed (kJ)	Final Temperature (K)	Heat Absorbed (kJ)	Final Temperature (K)	Heat Absorbed (kJ)
Water	336.97	11.8252	345.71	14.1838	344.49	13.8546
Glycerol	338.03	8.8350	346.45	10.4925	345.14	10.2346
MDM	340.57	4.5632	347.74	5.2531	346.55	5.1386
MD3M	343.73	4.9106	347.85	5.3106	346.59	5.1883

Table 5.8: Final temperatures and heat absorption values for all three designs, two positions and four materials

	Bottom Spheres					
	No Dome		1 Dome		2 Domes	
Material	**Final Temperature (K)**	**Heat Absorbed (kJ)**	**Final Temperature (K)**	**Heat Absorbed (kJ)**	**Final Temperature (K)**	**Heat Absorbed (kJ)**
Water	345.58	14.1486	339.25	12.4405	339.02	12.3784
Glycerol	346.36	10.4748	340.23	9.2680	339.84	9.1913
MDM	348.34	5.3112	342.00	4.7008	341.64	4.6661
MD3M	350.37	5.5553	342.15	4.7572	341.69	4.7125

The results show that the differences between 1 dome and 2 domes, in terms of temperature and heat absorbed are almost negligible for these two positions (top and bottom). Therefore, it can be concluded that the parameter which affects the output the most is the tank design for the entry of the HTF.

There is still a difference in final temperature and heat absorbed between the top and bottom spheres, but again the most noticeable changes here come from the materials and its relevant properties.

5.4 Graph Fittings

The results of temperature against time for the tested materials were again plotted in OriginPro, this time for the three tank designs. Following this, equations of the lines found for all three designs, for two positions, for the four materials using the software's fitting tool.

All the exponential and power fits were tried, yet only the ones which matched more accurately were considered. After various elimination processes, the one fit which worked best for the three designs was the ExpGro1. ExpGro1 is a one-phase exponential growth function with time constant parameter.

The equation is presented below:

Equation 5.4 (ExpGro1): $$y = y0 + A1 \cdot e^{(-\alpha t)}$$

The exponential basic model is $y = A\, e^{\alpha t}$, where y is the temperature present at time t. The A1 constant is the amplitude, t is the time, α is the rate of growth (if positive) or the rate of decay (if negative). Y0 is the final temperature approached by the horizontal asymptote.

Furthermore, Equation 5.5 was then derived from Equation 5.4. Equation 5.5 was used to present one set of results (for the material water only) in a linear equation, where the gradient was extracted and then further discussed.

Equation 5.5: $\ln(y - y0) = \ln(A1) - \alpha t$

The OriginPro website provides a diagram for the ExpGro1 mode:

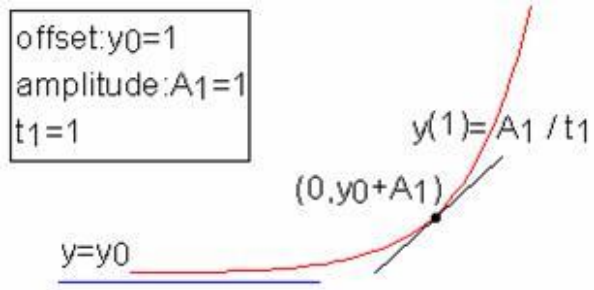

Figure 5.8: ExpGro1 sample curve

5.4.1 Top Sphere Fittings (Equation 5.4)

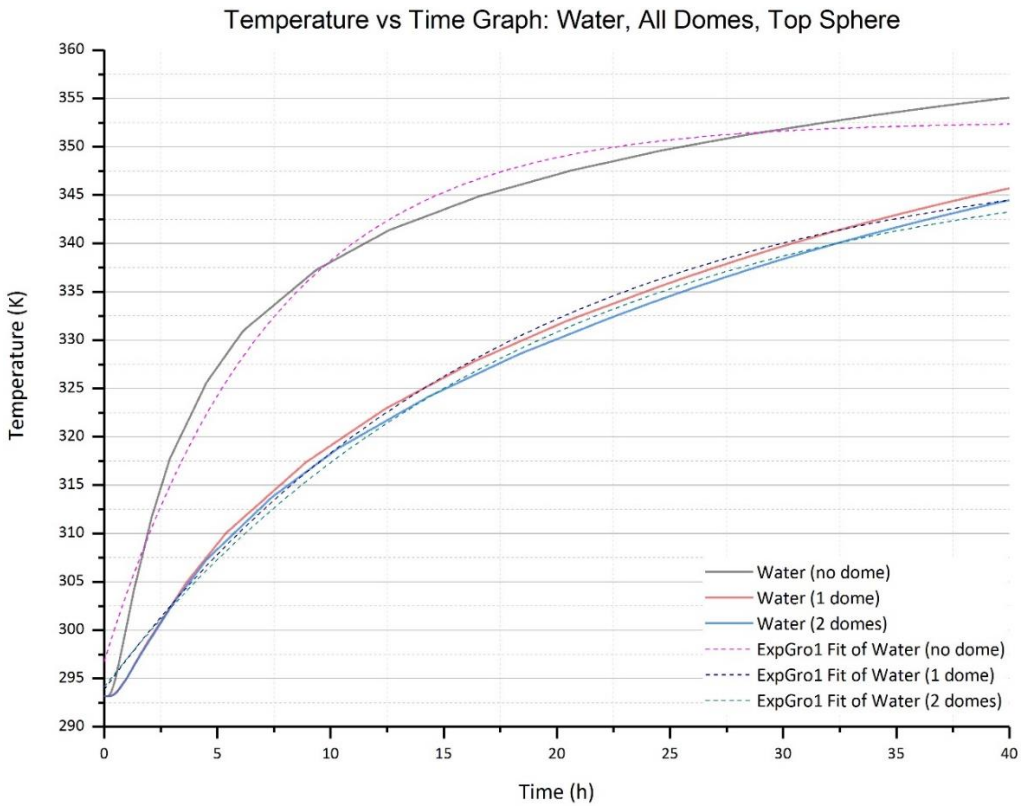

Figure 5.9: Temperature vs time graph of water, all domes, top sphere

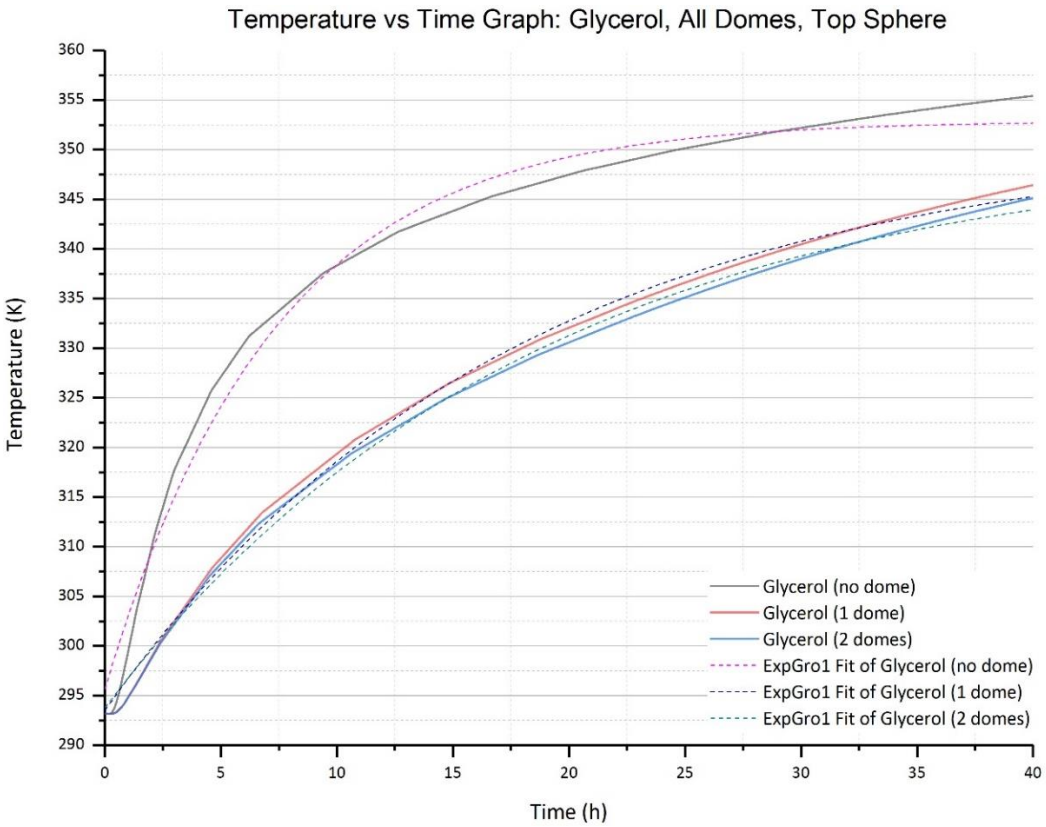

Figure 5.10: Temperature vs time graph of glycerol, all domes, top sphere

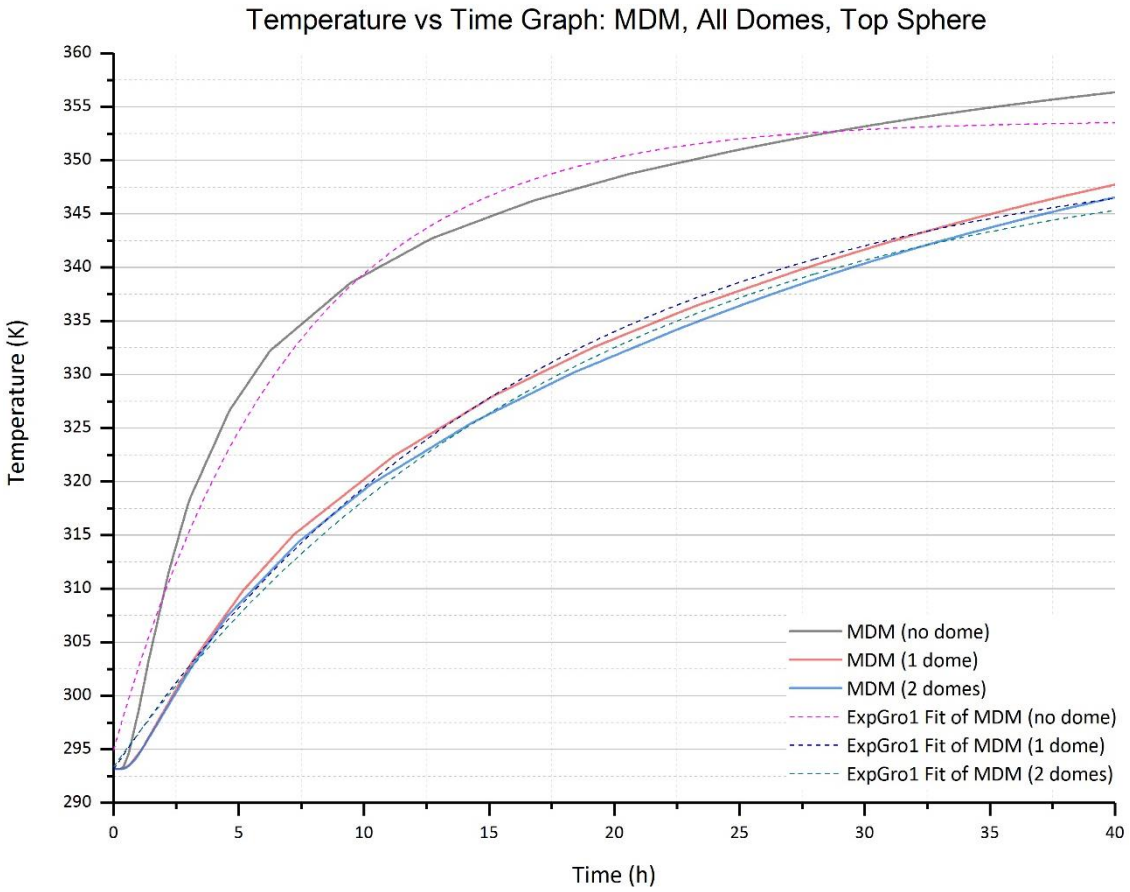

Figure 5.11: Temperature vs time graph of MDM, all domes, top sphere

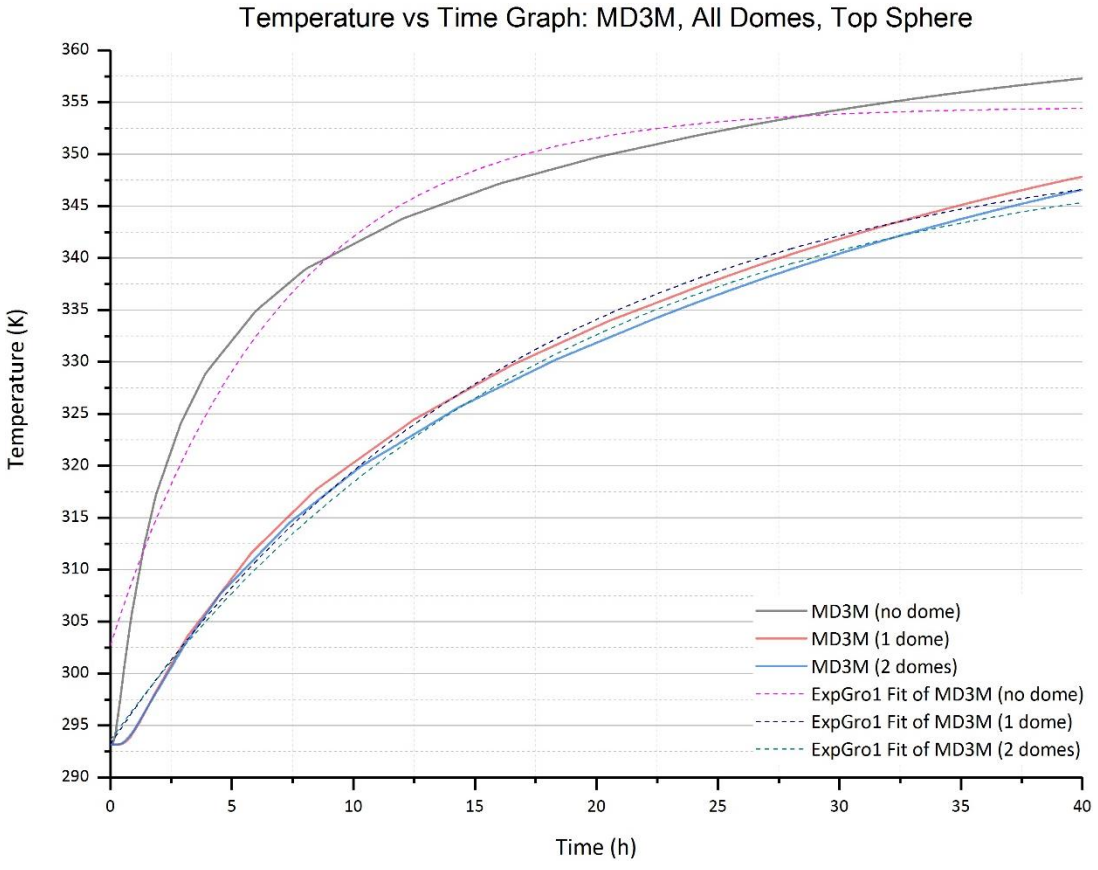

Figure 5.12: Temperature vs time graph of MD3M, all domes, top sphere

5.4.2 Bottom Sphere Fittings (Equation 5.4)

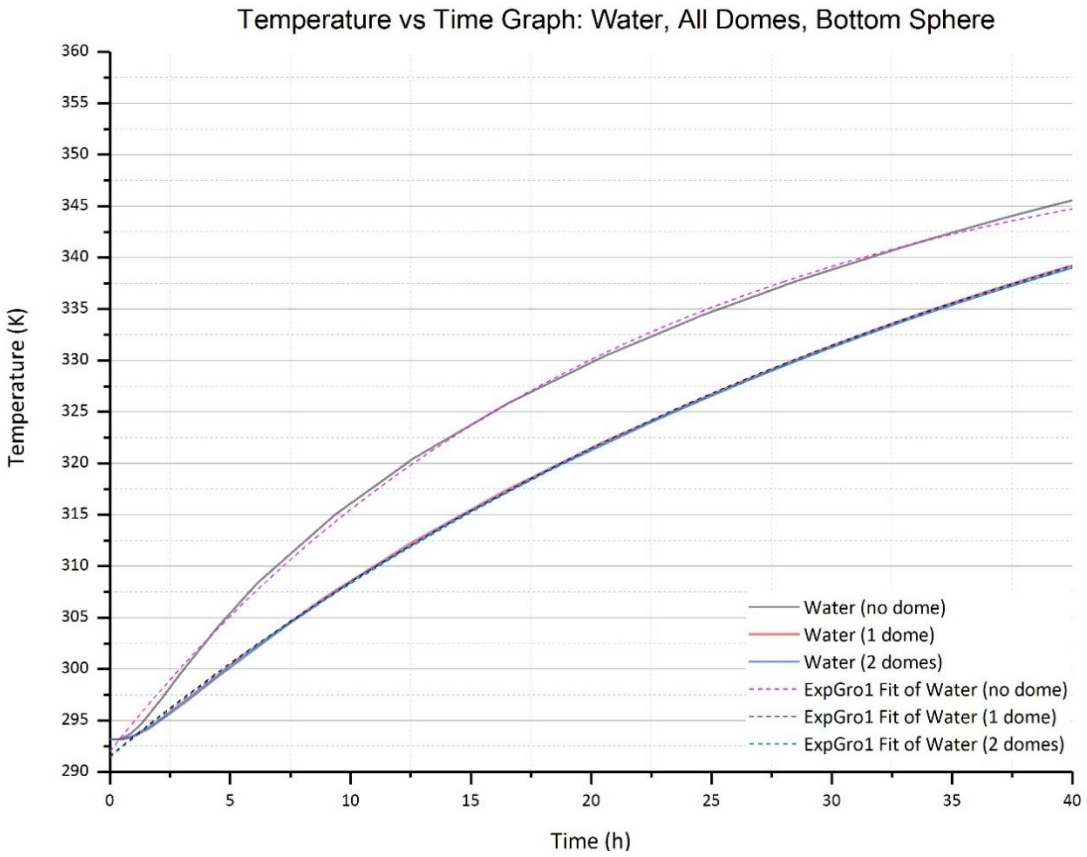

Figure 5.13: Temperature vs time graph of water, all domes, bottom sphere

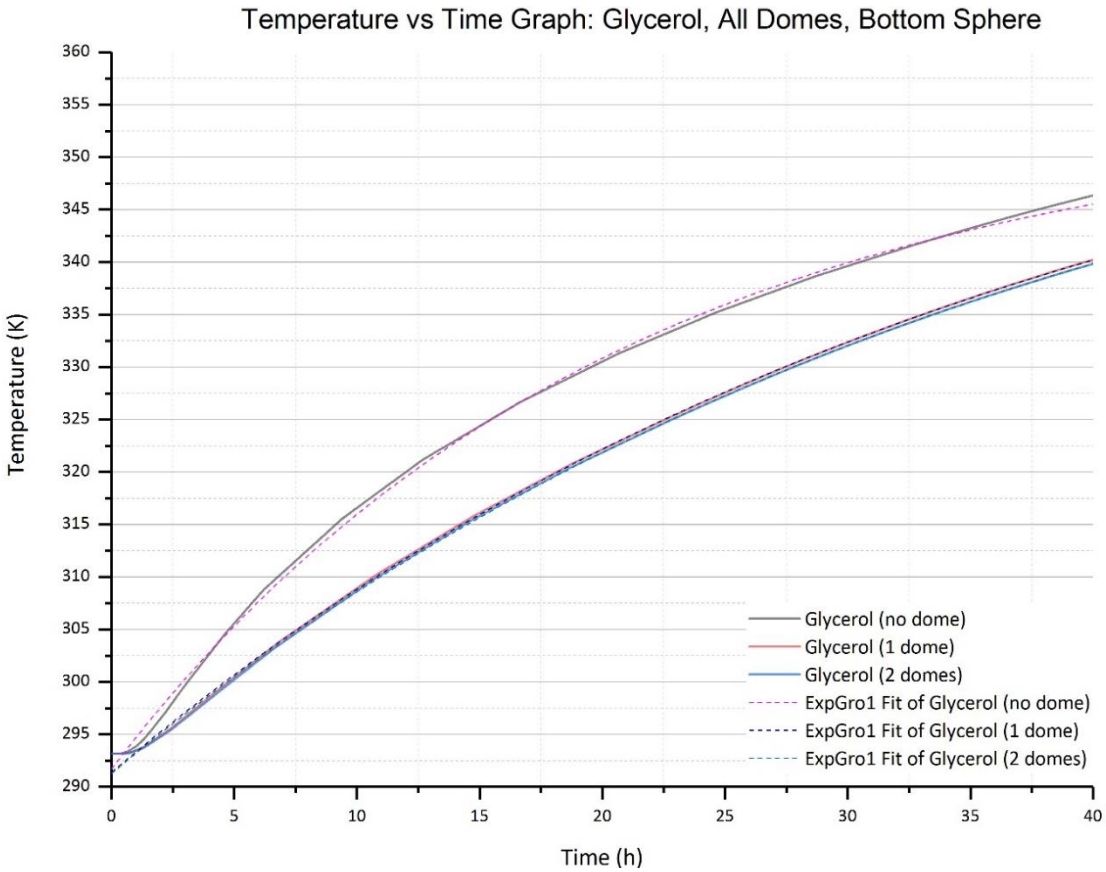

Figure 5.14: Temperature vs time graph for glycerol, all domes, bottom sphere

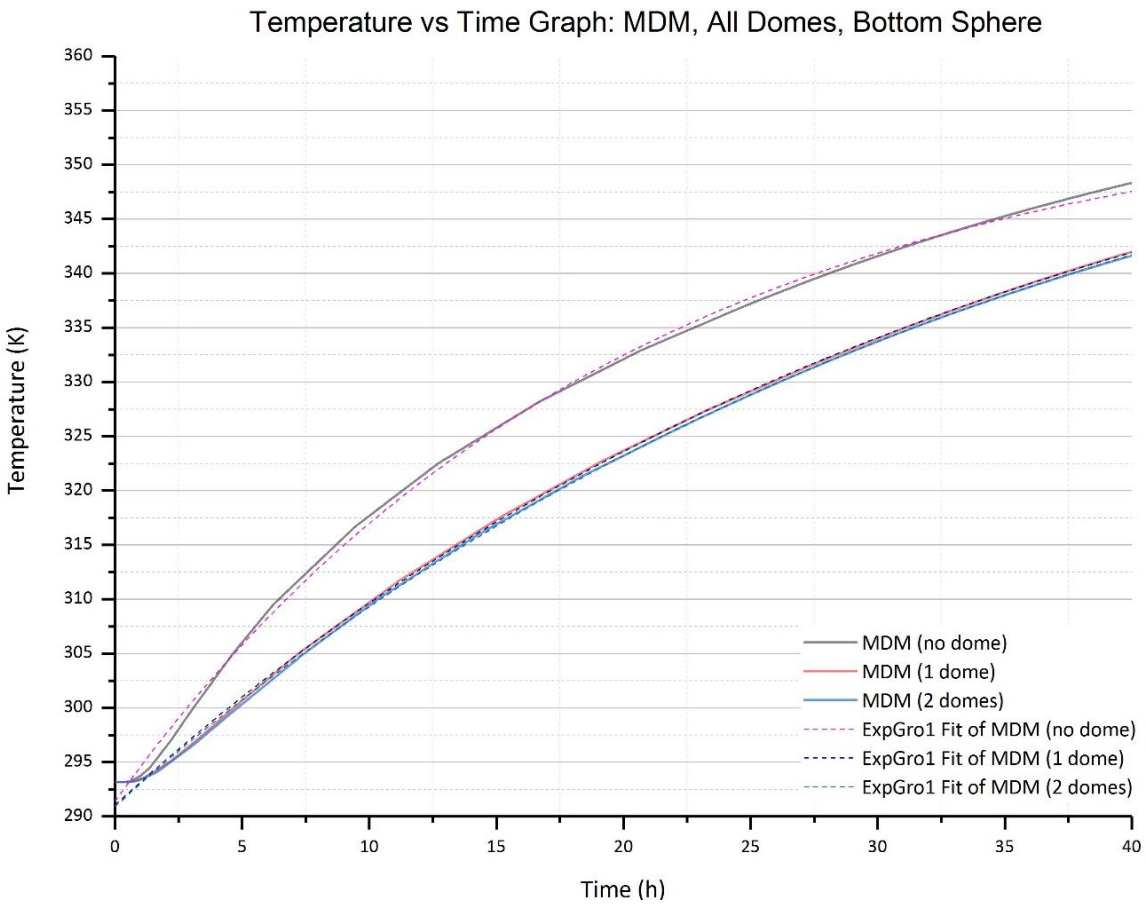

Figure 5.15: Temperature vs time graph of MDM, all domes, bottom sphere

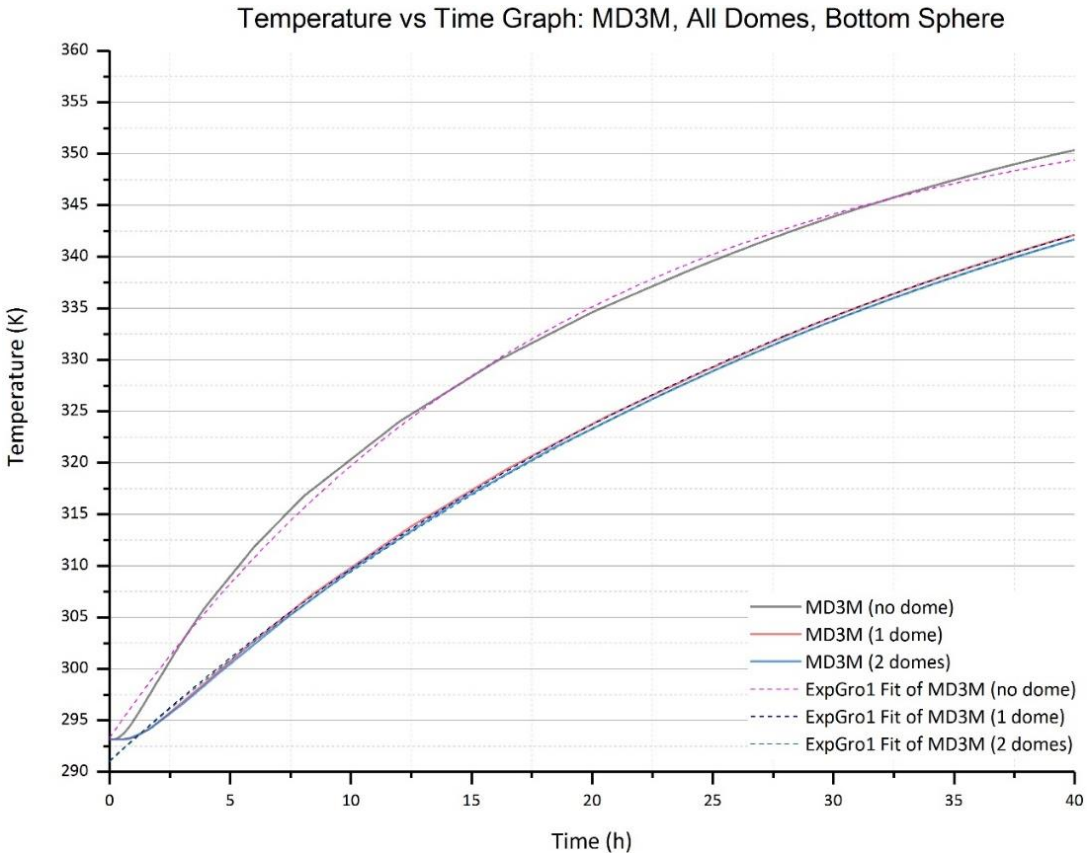

Figure 5.16: Temperature vs time graph of MD3M, all domes, bottom sphere

5.5 Discussion

5.5.1 Graphs

The fits for the top spheres do not match as well as the ones for the bottom spheres do, especially for the no dome top sphere. From the graphs, it is seen that there is a considerably large temperature difference in the final temperatures between the no dome design and the other two design's result. Percentages for the differences were calculated in Table 5.9:

Table 5.9: Percentage difference between tank designs (temperature)

	TOP SPHERES			BOTTOM SPHERES		
Material	**No Dome Tf - 1 Dome Tf**	**No Dome Tf - 2 Domes Tf**	**1 Dome Tf - 2 Domes Tf**	**No Dome Tf - 1 Dome Tf**	**No Dome Tf - 2 Domes Tf**	**1 Dome Tf - 2 Domes Tf**
Water	2.64%	2.99%	0.35%	1.83%	1.90%	0.07%
Glycerol	2.53%	2.90%	0.38%	1.77%	1.88%	0.11%
MDM	2.42%	2.75%	0.34%	1.82%	1.92%	0.11%
MD3M	2.64%	3.00%	0.36%	2.35%	2.48%	0.13%

Even though the final temperatures are different for each material, the difference in percentages between the tank designs is consistent and follow the same pattern. For all the tested substances, the difference now as a percentage between the 1 dome design and the 2 domes design can be classified as negligible. Furthermore, the top spheres show larger percentage differences than the bottom spheres, suggesting the bottom spheres have more similar heating dynamics than the top ones.

5.5.2 Equations and fitting coefficients

The coefficients for each material for each situation were extracted in order to compare them. These values are presented in Table 5.10 and Table 5.11. The extra parameter R^2 shows how well the equation fit with the original COMSOL plotted values. These values were again scored on a colour scale using the same criteria of red (lowest) to green (highest).

By themselves, these values could not be compared. Therefore, they were separated into top and bottom, and by tank design. Furthermore, the final temperatures that COMSOL simulated were compared to the y0 values in the ExpGro1.

Table 5.10: Values for the fitting equations for four materials, three designs, top sphere

	ExpGro1 Fit - Top Spheres					
Material	**Final temp. (K)**	**y0**	**A1**	**α**	**R^2**	
Water	355.09	352.59449	-55.82995	-7.37244	0.98334	NO DOME
Glycerol	355.43	352.91787	-57.28318	-7.26781	0.98431	
MDM	356.36	353.72658	-58.80356	-7.07918	0.98329	
MD3M	357.30	354.59502	-51.88492	-7.03543	0.9702	
Water	345.71	350.30246	-56.43729	-17.59654	0.99726	1 DOME
Glycerol	346.45	351.13719	-57.61855	-17.50261	0.99742	
MDM	347.74	351.91345	-58.79104	-16.82511	0.99737	
MD3M	347.85	352.13311	-58.90766	-16.90365	0.99736	
Water	344.49	349.64796	-55.51137	-18.48205	0.99683	2 DOMES
Glycerol	345.14	350.43707	-56.65175	-18.44543	0.99715	
MDM	346.55	351.5923	-58.22565	-17.92236	0.99722	
MD3M	346.59	351.54356	-57.94287	-17.87896	0.99705	

Table 5.11 Values for the fitting equations for four materials, three designs, bottom sphere

	ExpGro1 Fit - Bottom Spheres					
Material	**Final temp. (K)**	**y0**	**A1**	**α**	**R^2**	
Water	345.58	353.90309	-61.90682	-20.93478	0.99911	NO DOME
Glycerol	346.36	354.33614	-62.62971	-20.40136	0.99908	
MDM	348.34	356.31224	-64.89345	-19.97471	0.99894	
MD3M	350.37	356.80148	-63.50421	-18.59966	0.99836	
Water	339.25	365.02083	-73.44761	-38.27979	0.9998	1 DOME
Glycerol	340.23	365.73836	-74.35861	-37.40788	0.99976	
MDM	342.00	365.5904	-74.54411	-34.83569	0.99966	
MD3M	342.15	365.89148	-74.80892	-34.89764	0.99969	
Water	339.02	364.83763	-73.39878	-38.30716	0.99976	2 DOMES
Glycerol	339.84	365.58873	-74.32203	-37.70421	0.99973	
MDM	341.64	366.54053	-75.60464	-35.92941	0.99962	
MD3M	341.69	366.17518	-75.14931	-35.61883	0.99966	

The ExpGro1 fits are not that precise, yet work well for a simple equation, especially on the bottom sphere. The final temperatures are significantly different for the 1 dome and 2 dome designs for the bottom sphere (≈25K), yet the lines graphically and visually match up better than the results for the top sphere which are closer to the final temperatures from COMSOL (2K – 5K difference).

In terms of the coefficients, the amplitudes for the top spheres in Table 5.10 are all similar values which range from -55 to -59 approximately. The main variation happens across the different materials. Within the material itself, the ranges for the three amplitudes for the designs varies very little (for example, water remains at an amplitude of -56 ±0.5 approximately). For the bottom spheres, nonetheless, the difference in amplitudes occurs both throughout materials and designs. The largest amplitudes are the ones in the no dome design. The 1 and 2 dome designs for the bottom sphere are

again similar. The difference between the top and bottom amplitudes is significant, again exposing the difference in heating dynamics through the system.

5.5.3 Material analysis

Table with the material results only were produced to evaluate individual performances of the substances and what the effect of changing the design was.

Table 5.12: Key for the colour code and abbreviations in the following tables

Key Colour		Nomenclature
Lowest		**0D**: No Dome
Low		
Average (low)		**1D**: 1 Dome
Average (high)		
High		**2D**: 2 Domes
Highest		

Table 5.13: ExpGro1 fit coefficients for water

Water							
Final Temp. (K)	**Heat Abs. (kJ)**	**y0**	**A1**	**α**	**R^2**	**Design Type**	
355.09	16.71506	352.59449	-55.82995	-7.37244	0.98334	**0D**	**TOP SPHERES**
345.71	14.18379	350.30246	-56.43729	-17.59654	0.99726	**1D**	
344.49	13.85456	349.64796	-55.51137	-18.48205	0.99683	**2D**	
345.58	14.14871	353.90309	-61.90682	-20.93478	0.99911	**0D**	**BOTTOM SPHERES**
339.25	12.44050	365.02083	-73.44761	-38.27979	0.99980	**1D**	
339.02	12.37843	364.83763	-73.39878	-38.30716	0.99976	**2D**	

For water, the highest final temperature is the no dome design for the top sphere, which as expected corresponds to the highest heat absorbed and an average (low) y0 value. The amplitude here is a high value and the decay constant for the no dome design is the highest.

The design which had the lowest temperature and heat absorbed per sphere is the 2 domes design for the bottom sphere. The y0 value for this setup was high, with a low amplitude value and the lowest decay constant.

The design which had the highest y0 value is the 1 dome for the bottom sphere, which in return had the lowest amplitude value. The decay constant, final temperature and heat absorption values were all a low value.

The highest amplitude was reached by the 2 domes design for the top sphere, which had the lowest y0 value assigned to it too. It had average (high) decay constant and heat absorbed values and an average (low) final temperature.

Table 5.14: ExpGro1 fit coefficients for glycerol

Glycerol							
Final Temp. (K)	**Heat Abs. (kJ)**	**y0**	**A1**	**α**	**R^2**	**Design Type**	
355.43	12.26028	352.91787	-57.28318	-7.26781	0.98431	**0D**	**TOP SPHERES**
346.45	10.49250	351.13719	-57.61855	-17.50261	0.99742	**1D**	
345.14	10.23462	350.43707	-56.65175	-18.44543	0.99715	**2D**	
346.36	10.47478	354.33614	-62.62971	-20.40136	0.99908	**0D**	**BOTTOM SPHERES**
340.23	9.26805	365.73836	-74.35861	-37.40788	0.99976	**1D**	
339.84	9.19127	365.58873	-74.32203	-37.70421	0.99973	**2D**	

For glycerol, all sorts and arrangements shown in Table 5.14, match what was previously stated for the water design. If both tables are compared, they are the same in terms of colours. The patterns followed are identical.

Table 5.15: ExpGro1 fit coefficients for MDM

MDM							
Final Temp. (K)	**Heat Abs. (kJ)**	**y0**	**A1**	**α**	**R^2**	**Design Type**	
356.36	6.08264	353.72658	-58.80356	-7.07918	0.98329	**0D**	**TOP SPHERES**
347.74	5.25315	351.91345	-58.79104	-16.82511	0.99737	**1D**	
346.55	5.13863	351.59230	-58.22565	-17.92236	0.99722	**2D**	
348.34	5.31088	356.31224	-64.89345	-19.97471	0.99894	**0D**	**BOTTOM SPHERES**
342.00	4.70079	365.59040	-74.54411	-34.83569	0.99966	**1D**	
341.64	4.66615	366.54053	-75.60464	-35.92941	0.99962	**2D**	

For MDM, the highest final temperature and heat absorbed is also the no dome design for the top sphere. This time, different to the other two materials, the y0 had an average (low) y0 value and the amplitude had an average (high) value. The decay constant was, again, the highest.

The design which had the lowest temperature and heat absorption was also the 2 domes design for the bottom sphere. The y0 value for this setup was the highest, with a low amplitude value and the lowest decay constant.

The highest amplitude was reached by the 2 domes design for the top sphere, which is the same as glycerol and water. The colours are the same as the ones in the other two graphs.

Table 5.16: ExpGro1 fit coefficients for MD3M

MD3M							
Final Temp. (K)	**Heat Abs. (kJ)**	**y0**	**A1**	**α**	**R^2**	**Design Type**	
357.30	6.22804	354.59502	-51.88492	-7.03543	0.97020	**0D**	**TOP SPHERES**
347.85	5.31058	352.13311	-58.90766	-16.90365	0.99736	**1D**	
346.59	5.18825	351.54356	-57.94287	-17.87896	0.99705	**2D**	
350.37	5.55524	356.80148	-63.50421	-18.59966	0.99836	**0D**	**BOTTOM SPHERES**
342.15	4.75719	365.89148	-74.80892	-34.89764	0.99969	**1D**	
341.69	4.71253	366.17518	-75.14931	-35.61883	0.99966	**2D**	

The no dome design for the top sphere for the material MD3M has the highest final temperature, heat absorbed, amplitude and decay constant values. The remaining y0 value is an average (low).

The design which had the highest y0 value is the 2 domes for the bottom spheres. In this one, the material underperformed as it has the lowest final temperature, heat absorbed, amplitude and decay constant values.

Even though all the materials have very different relevant properties (as seen in Table 5.2) which affect the amount of heat absorbed per sphere and the final temperature, they still follow the same heating dynamics which matches the exponential fit. In fact, the difference between final temperature values is approximately ±8K, which only corresponds to a maximum difference of 14% per material if considering that the material has been heated roughly 56K from a starting temperature of 293.15K.

Furthermore, the decay constant values along Tables 5.13 – 5.16 follow the same pattern for all materials. These decrease through the table as the design of the tank changes and can be seen to almost duplicate from top to bottom.

5.5.4 Design analysis

When the results are split between top and bottom and analysed separately, the no dome (for both top and bottom) have highest final temperature and heat absorption. These values decrease along the table, meaning the 1 dome designs carry the average final temperatures and heat absorptions, leaving the 2 dome designs with the lowest.

Looking at the R^2 values in the tables, it is seen that the exponential function for the no dome design does not fit as well as it does for the dome designs. This is probably relevant to the re-circulation that happens when the HTF enters in contact with the spheres at the inlet velocity, as in the no dome design there is barely any space for the fluid to settle. Also, the differences in temperature and heat absorption between having 1 dome and 2 domes are almost negligible. This means the key element in the design which will allow for an effective heat transfer is the inlet of the HTF.

5.5.5 Comparison to natural logarithm analysis

Using Equation 5.5, the natural logarithm of y-y0 was plotted against time t. All the sensible heat materials were evaluated for the no dome design, for the top sphere only, for all time steps. See Figures 5.17 to 5.20:

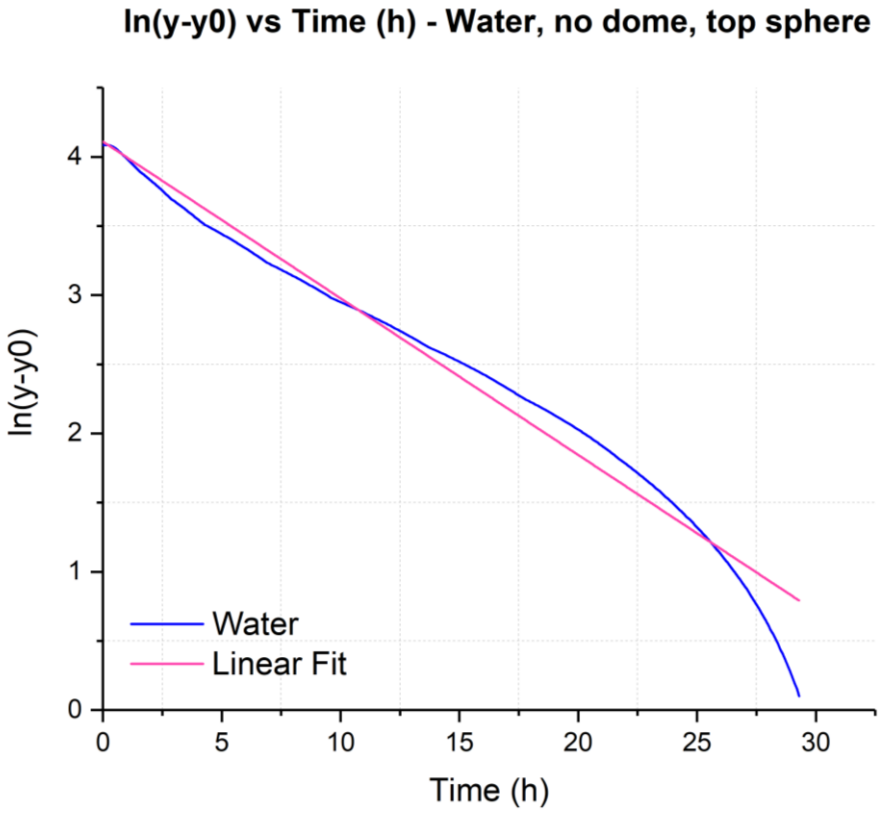

Figure 5.17: ln(y-yo) vs time plot for water, for the no dome design for the top sphere

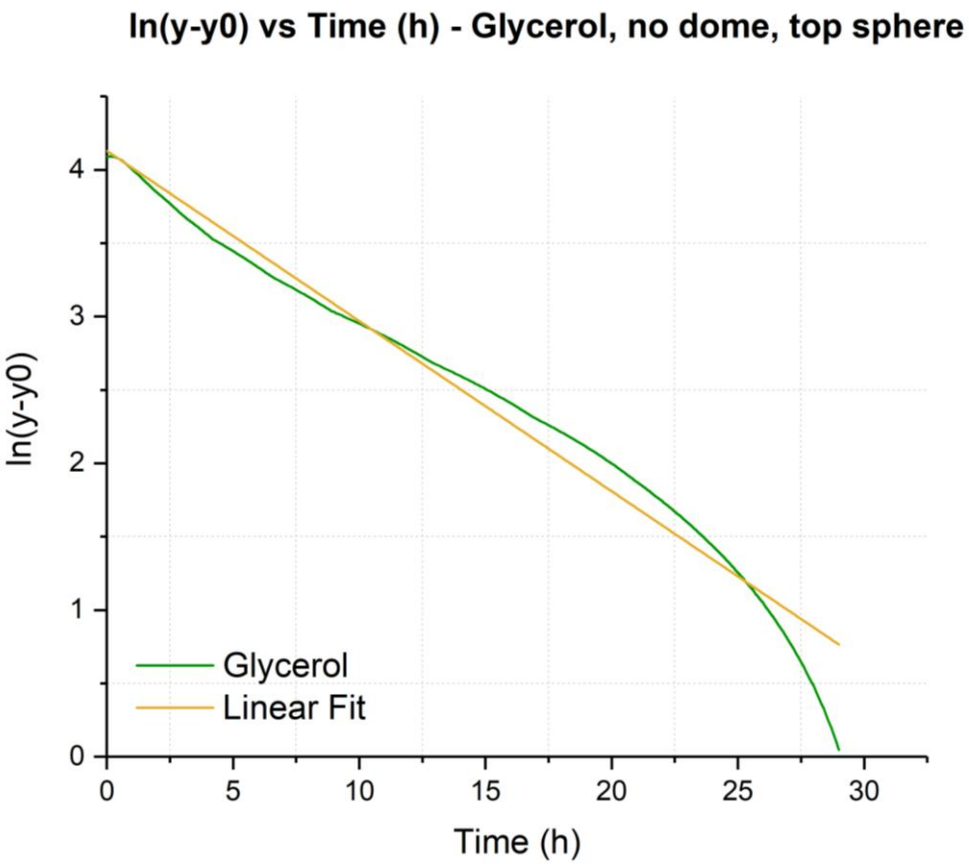

Figure 5.18: ln(y-yo) vs time plot for glycerol, for the no dome design for the top sphere

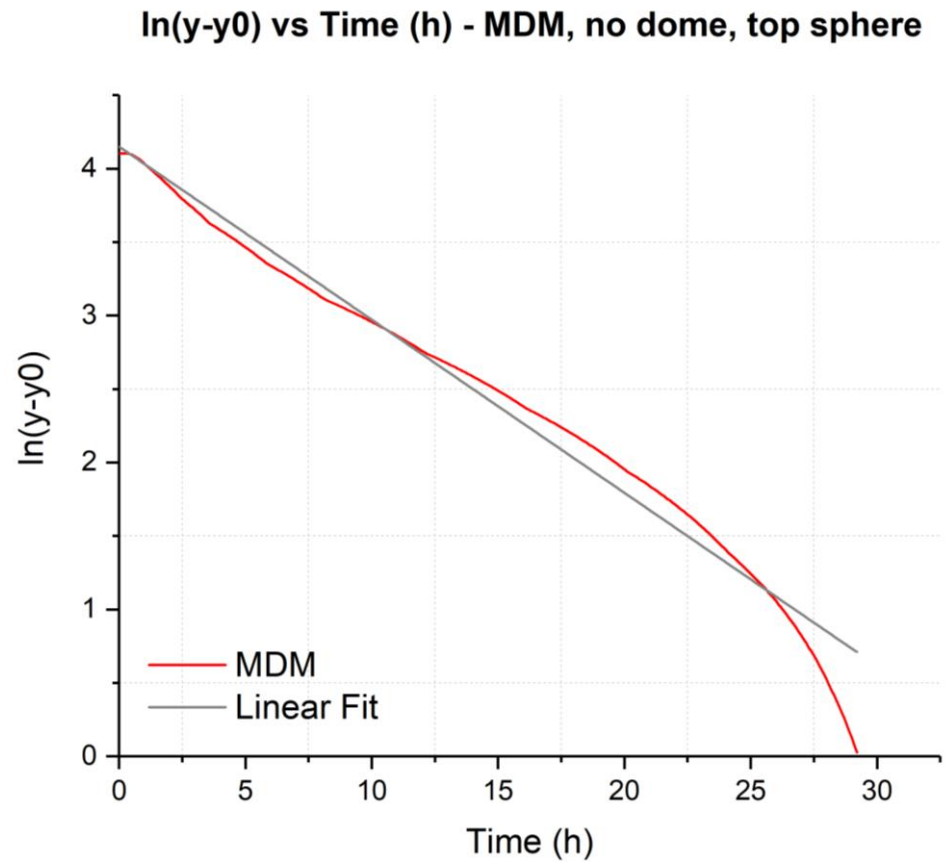

Figure 5.19: ln(y-yo) vs time plot for mdm, for the no dome design for the top sphere

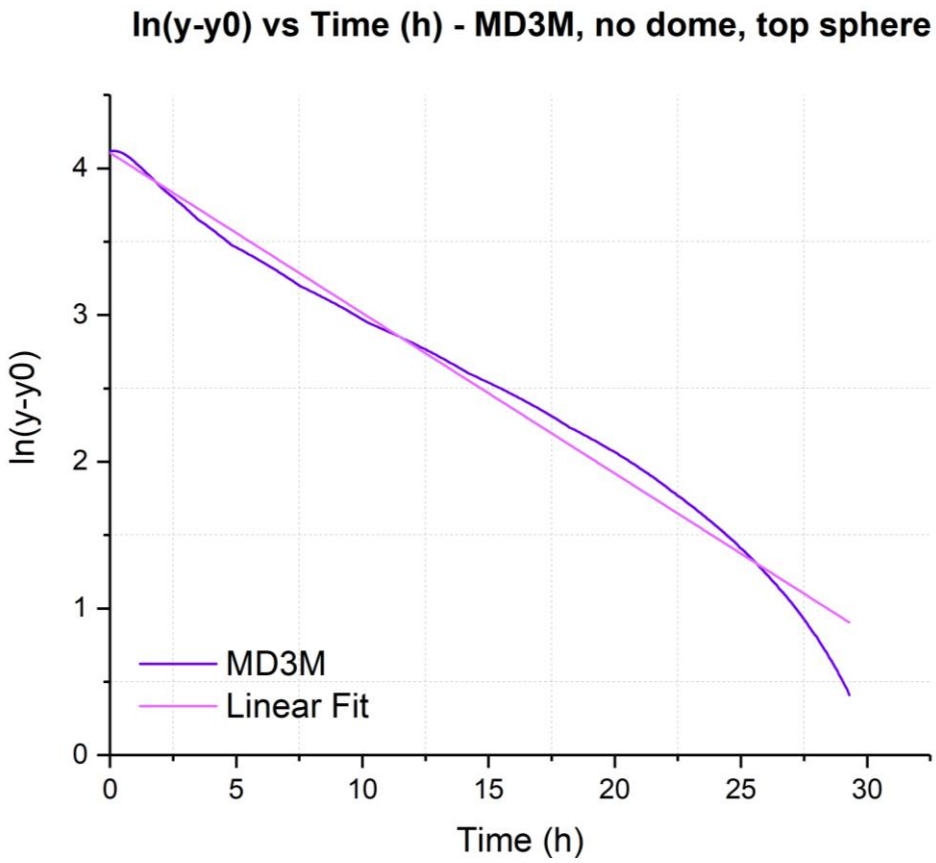

Figure 5.20: ln(y-yo) vs time plot for md3m, for the no dome design for the top sphere

The lny-y0 vs time lines were fitted with a linear fit and the equation for each was found, which gave new values for A1 and alpha. A comparison between Equation 5.4 and 5.5 A1 and alpha values can be found in Table 5.17:

Table 5.17: A1 and alpha values comparison using Equations 5.4 and 5.5

	Equation 5.4		**Equation 5.5**		
Material	**A1**	**alpha**	**A1**	**alpha**	**R^2**
Water	-55.82995	-7.37244	-60.95464	-8.82924	97.450%
Glycerol	-57.28318	-7.26781	-62.15803	-8.61920	97.336%
MDM	-58.80356	-7.07918	-63.44923	-8.48824	97.805%
MD3M	-51.88492	-7.03543	-60.73195	-9.14997	98.397%

Generally, the Equation 5.5 A1 and alpha values are very similar to the 5.4 ones. From the similarity in the linear fit results and the very high R^2 values, it is seen that this method and equation will still give a good approximation. Values for A1 were generally underestimated, with differences of roughly 8% to 15%. Equally, alpha values were also underestimated by a larger margin of approximately 16% to 23%. The values that differ the most for both A1 and alpha happen for the material MD3M. The closest, again for both, is MDM.

VI. Phase Changing Material (PCM) Results

6.1 Graphical Analysis

Paraffin wax, n-Octadecane and Acetic Acid are now being modelled as latent heat parameters for encapsulated spheres. The simulation runs for 5minutes at 1s intervals. Temperature vs Time graphs were plotted for the selected PCMs. These included graphs plotted to see the effect of the design change, velocity change, different sphere position and the different material properties.

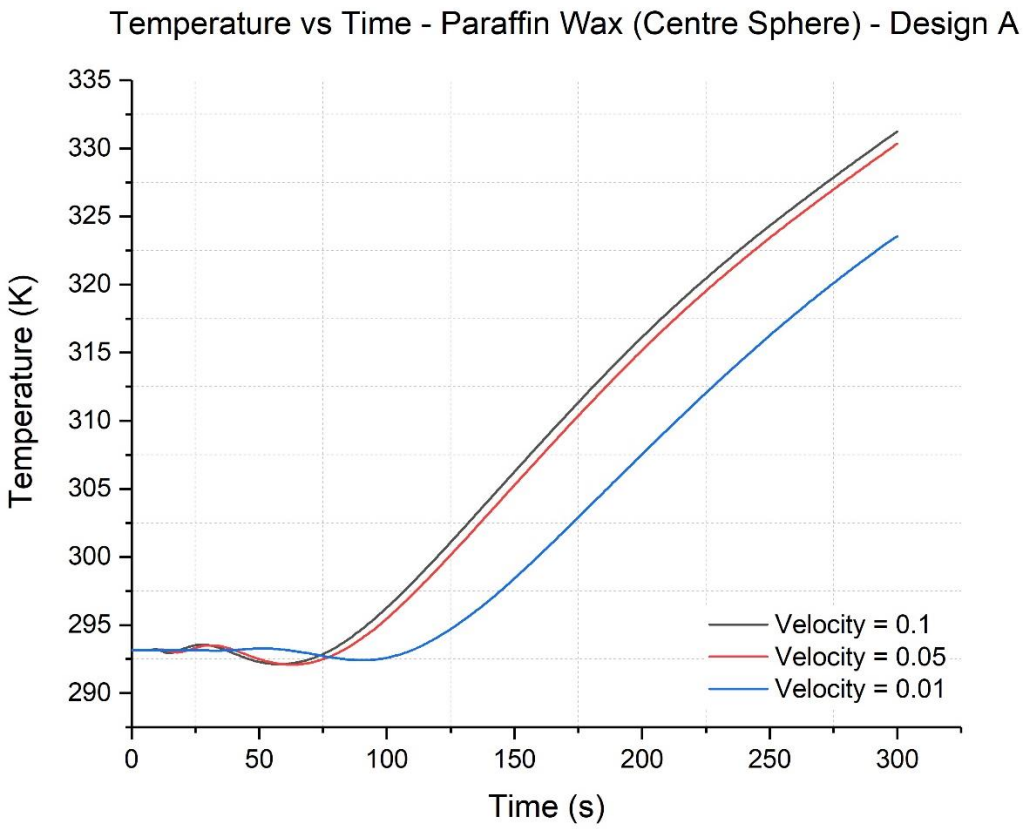

Figure 6.1: Temperature vs Time for paraffin wax for the centre sphere (Design A)

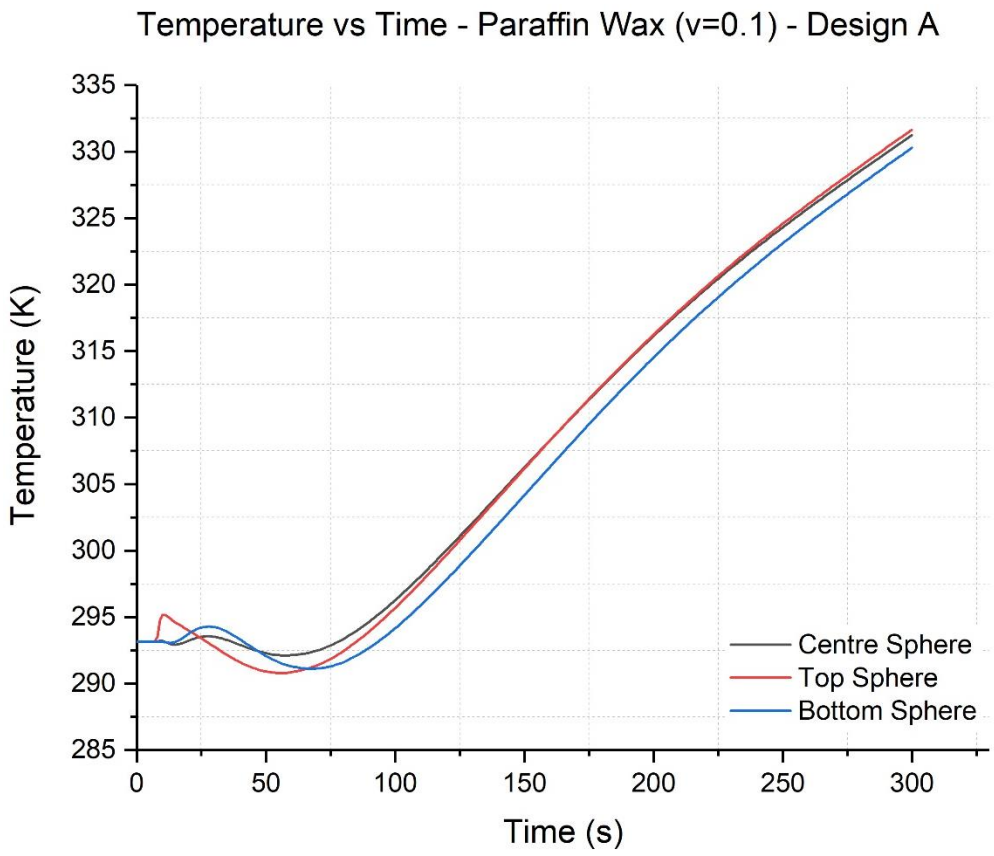

Figure 6.2: Temperature vs time for paraffin wax for a velocity of 0.1m/s (Design A)

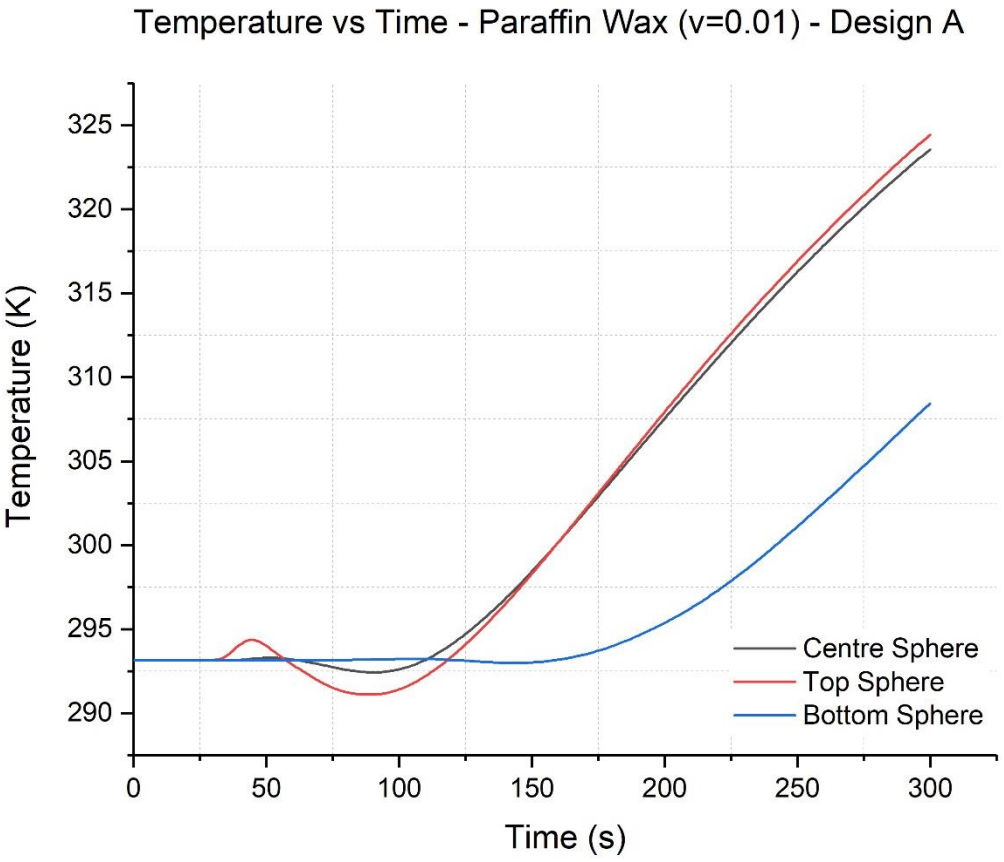

Figure 6.3: Temperature vs time for paraffin wax for a velocity of 0.01m/s (Design A)

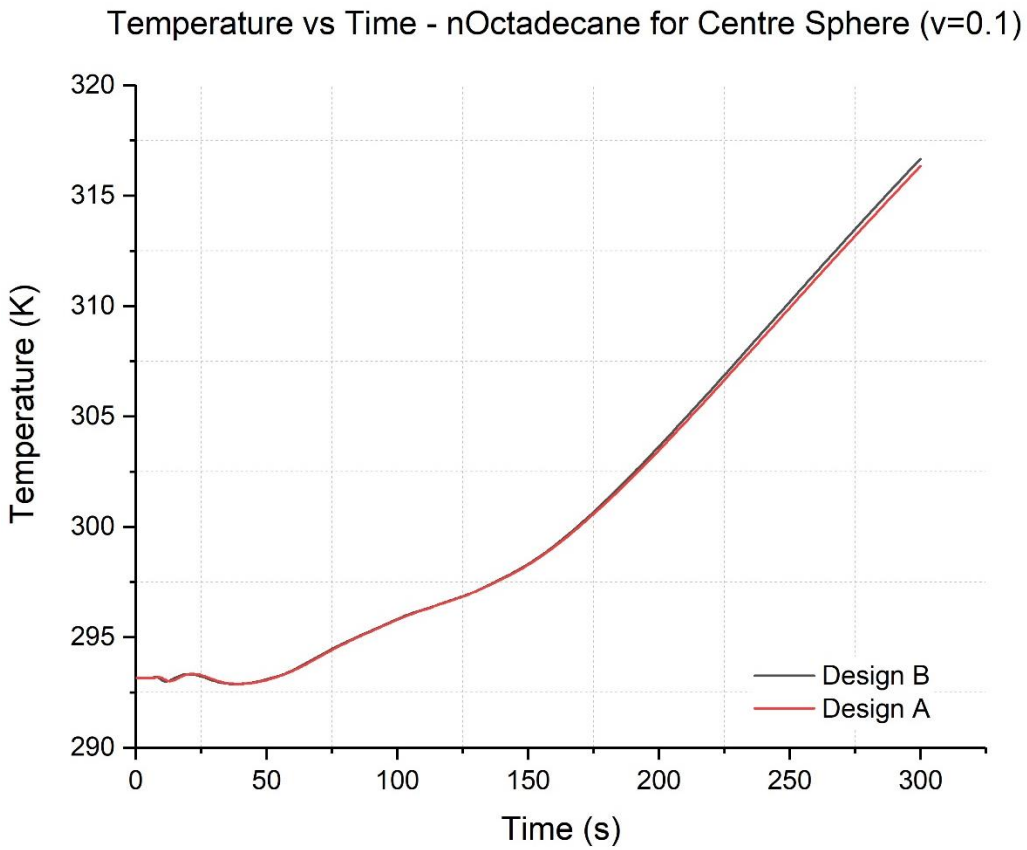

Figure 6.4: Temperature vs time for nOctadecane for the centre sphere, for both designs (v=0.1m/s)

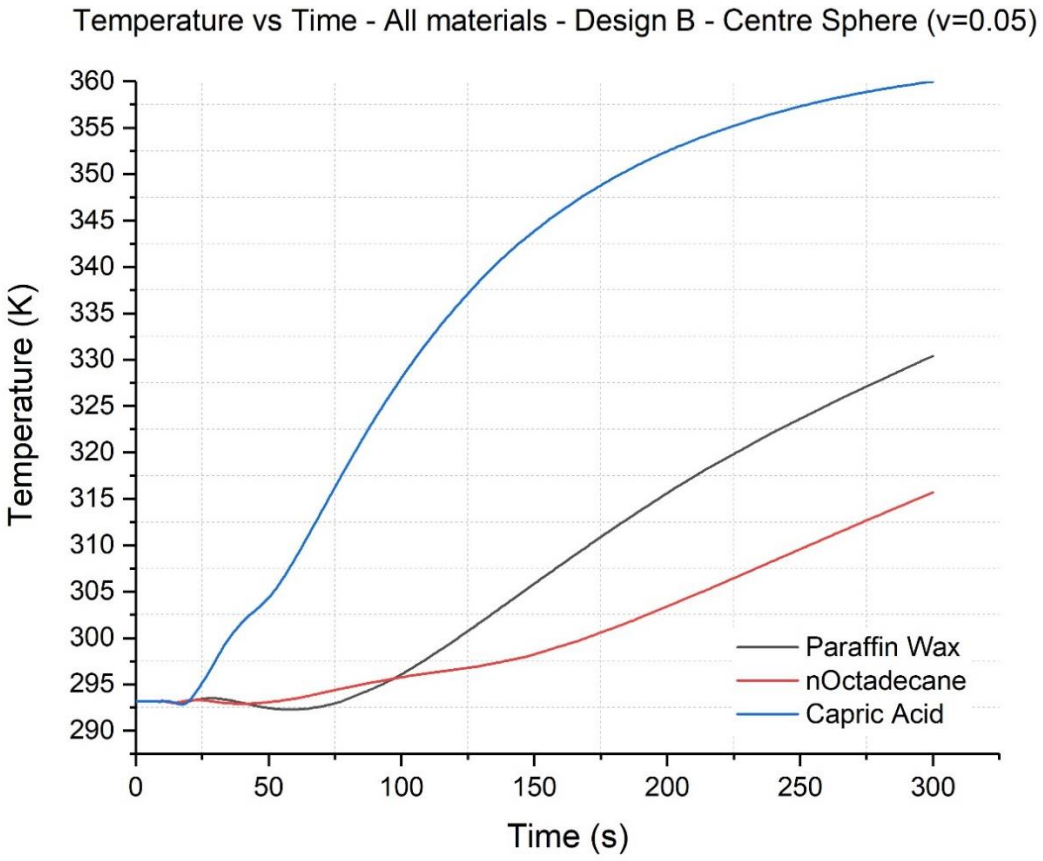

Figure 6.5: Temperature vs time for all materials, for Design B, for the centre sphere (v=0.05m/s)

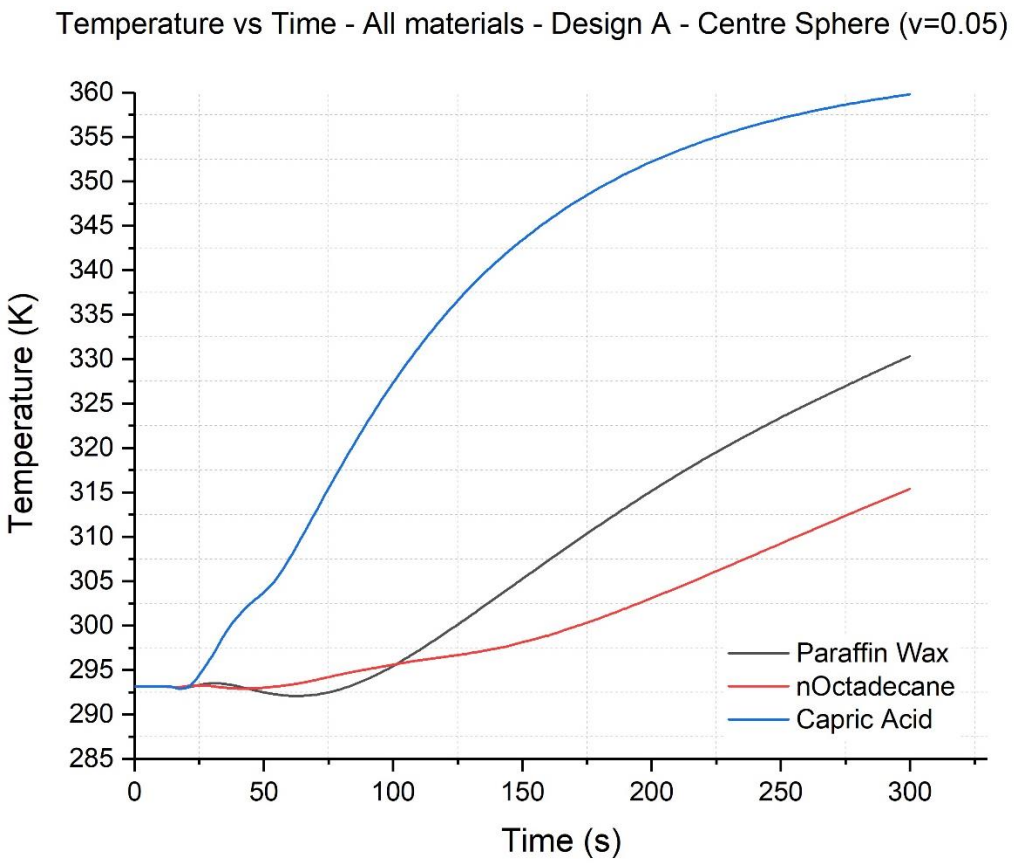

Figure 6.6: Temperature vs time for all materials, for Design A, for the centre sphere (v=0.05m/s)

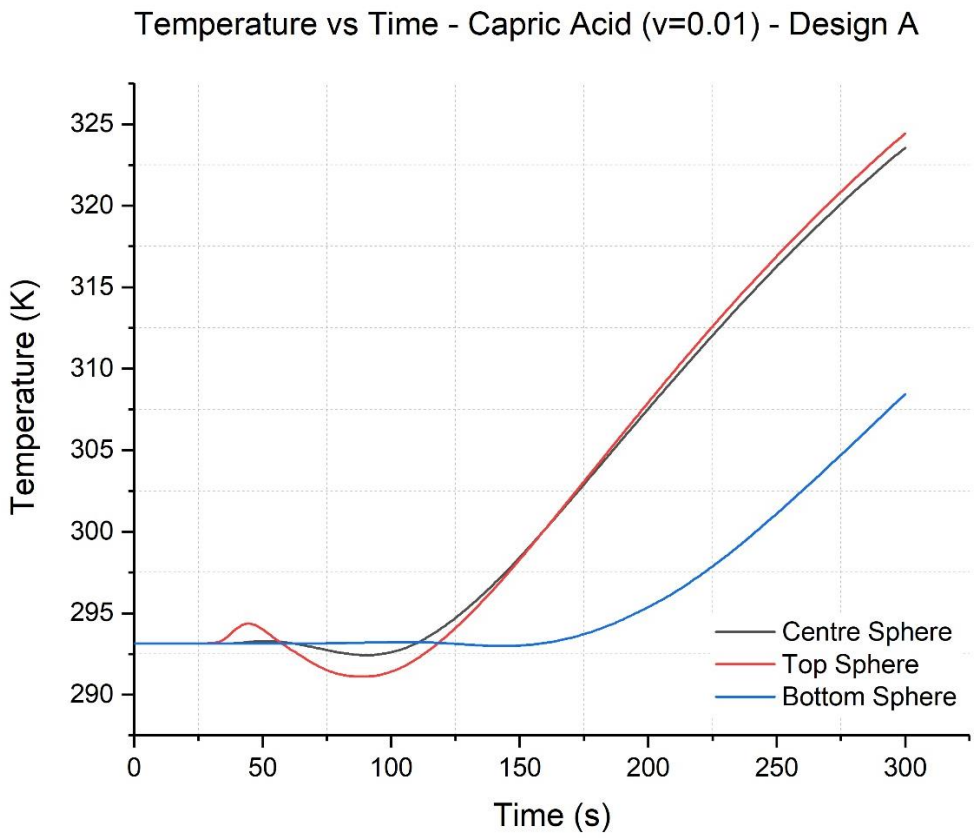

Figure 6.7: Temperature vs time for capric acid for a velocity of 0.01m/s (Design A)

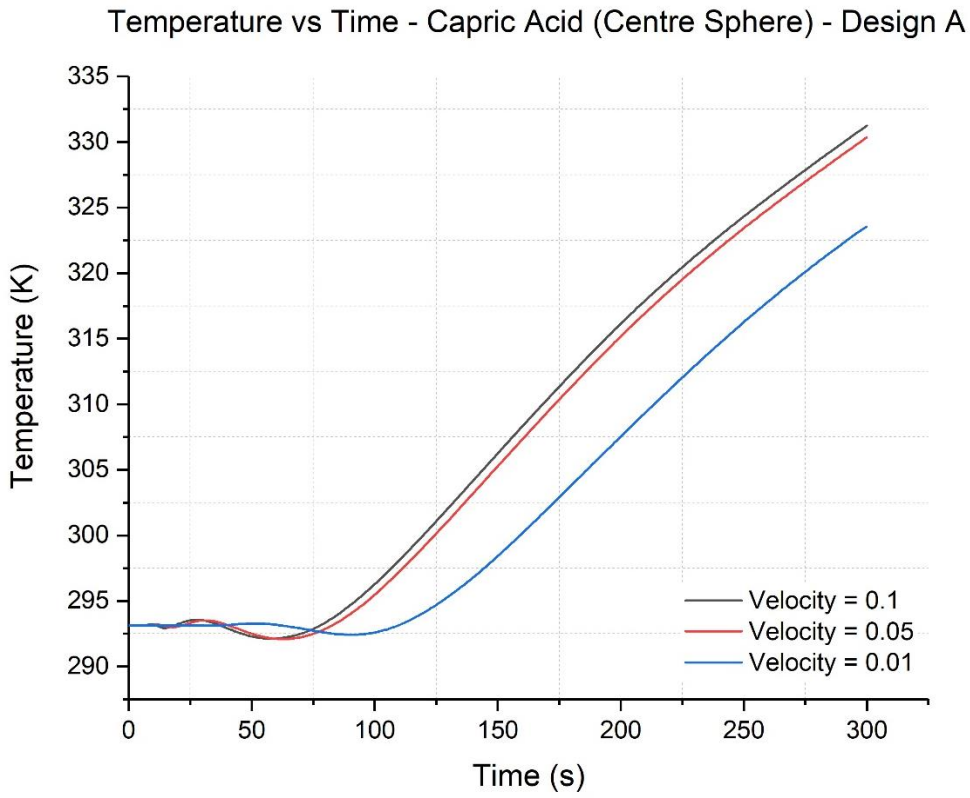

Figure 6.8: Temperature vs Time for capric acid for the centre sphere (Design A)

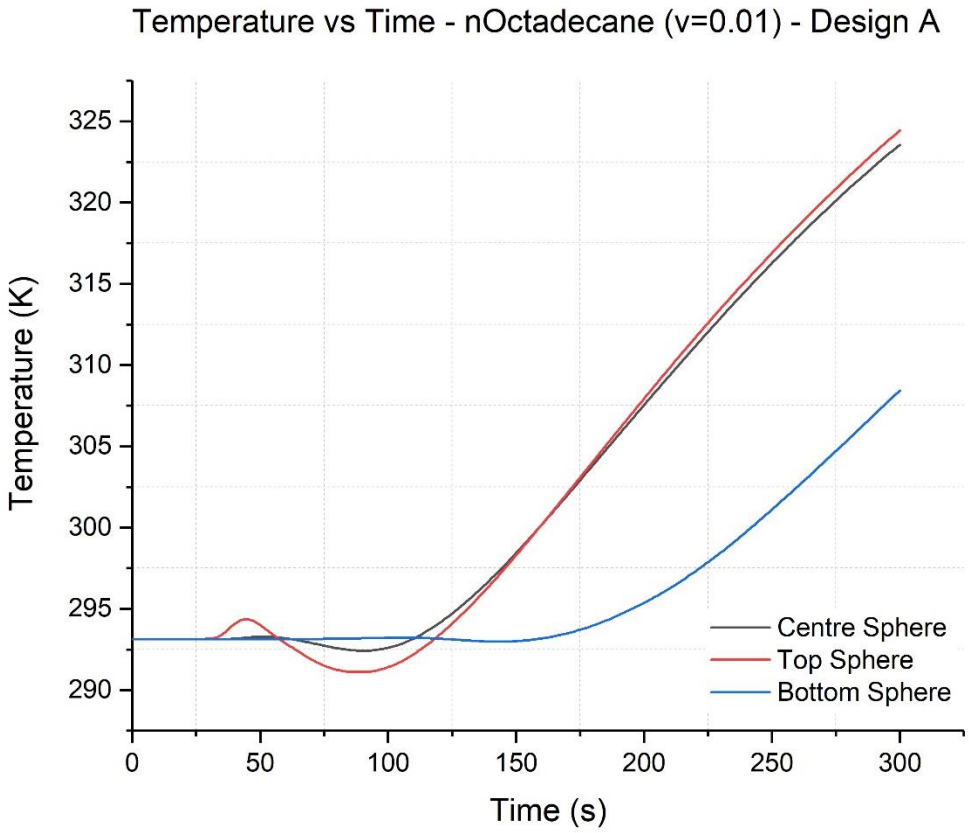

Figure 6.9: Temperature vs time for n-Octadecane for a velocity of 0.01m/s (Design A)

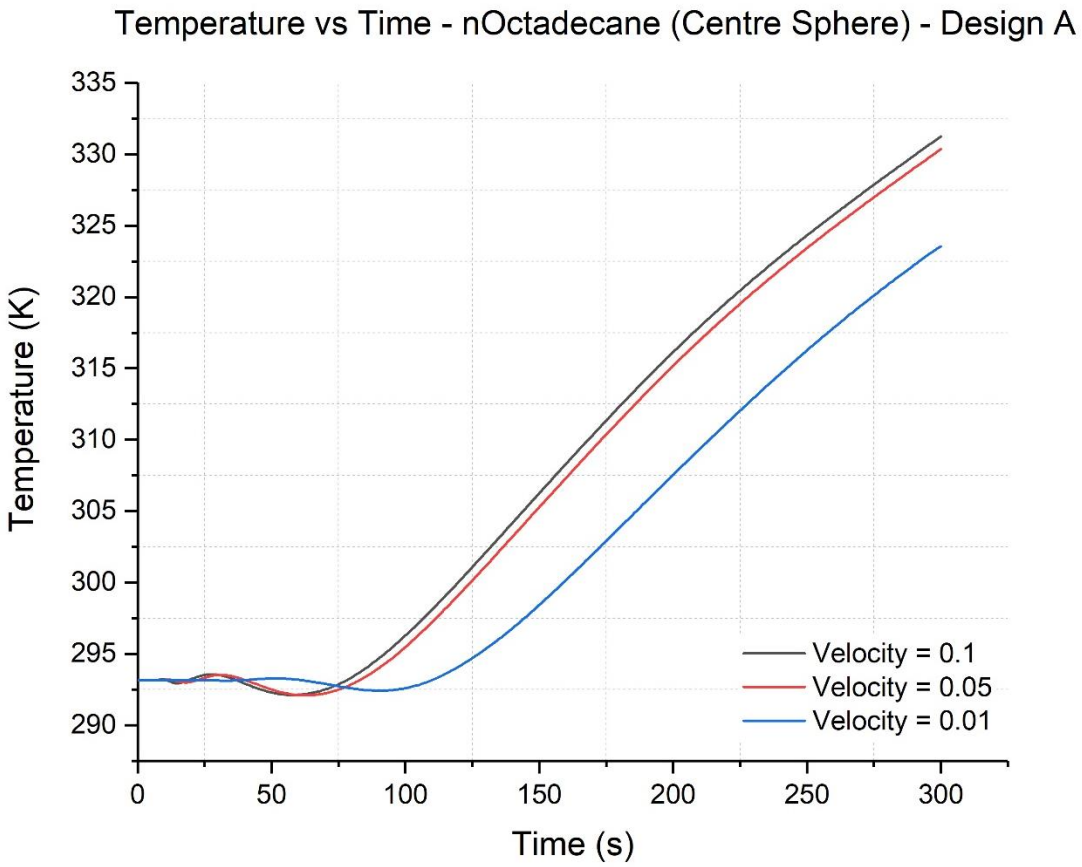

Figure 6.10: Temperature vs Time for n-Octadecane for the centre sphere (Design A)

6.2 Final Temperature and Heat Absorbed

As was done earlier, the final temperatures were recorded and the following equation was used to calculate the heat absorption per sphere for each design, all positions, velocities and materials:

Equation 6.1: $Q = m\,(Cps \cdot (Tm - Ti) + L + (Tf - Tm) \cdot Cpl)$

Where Q is heat absorbed per sphere, m is the mass per sphere, Tm is the melting temperature of the PCM, L is the latent heat, Ti is the initial temperature, Tf is the final temperature, Cps is the specific heat capacity of the solid and Cpl is the specific heat capacity of the liquid.

It is also worth noting that in Figures 6.1 to 6.10 there is a minor fluctuation associated with instability in the simulation during the early time steps. This was only present in version 5.3 of COMSOL Multiphysics and showed that heat was escaping the system rapidly through the outlet even though it was insulated elsewhere. Nonetheless, the residuals and thermal behaviour of the system was not compromised, and the results show the expected behaviour.

Table 6.1: Final temperature and heat absorbed for all materials, all velocities and both designs for the centre sphere

	Centre Sphere					
	Velocity = 0.1m/s		Velocity = 0.05m/s		Velocity = 0.01m/s	
Material	**Final Temp. (K)**	**Heat Abs. (J)**	**Final Temp. (K)**	**Heat Abs. (J)**	**Final Temp. (K)**	**Heat Abs. (J)**
Paraffin Wax Design A	331.24	1790.3413	330.35	1778.1087	323.55	1684.6463
Paraffin Wax Design B	331.82	1798.3131	330.40	1778.7959	326.00	1718.3203
nOctadecane Design A	316.34	1918.2633	315.41	1904.8966	310.54	1834.9011
nOctadecane Design B	316.67	1923.0063	315.71	1909.2084	312.35	1860.9159
Capric Acid Design A	360.24	1208.2522	359.80	1206.8826	357.57	1199.9412
Capric Acid Design B	360.43	1208.8436	359.99	1207.4740	358.28	1202.1512

Table 6.2: Final temperature and heat absorbed for all materials, all velocities and both designs for the top sphere

	Top Sphere					
	Velocity = 0.1m/s		Velocity = 0.05m/s		Velocity = 0.01m/s	
Material	**Final Temp. (K)**	**Heat Abs. (J)**	**Final Temp. (K)**	**Heat Abs. (J)**	**Final Temp. (K)**	**Heat Abs. (J)**
Paraffin Wax Design A	331.64	1795.8391	330.84	1784.8435	324.42	1696.6040
Paraffin Wax Design B	332.58	1808.7589	331.46	1793.3651	330.06	1774.1228
nOctadecane Design A	316.69	1923.2938	315.74	1909.6396	310.89	1839.9316
nOctadecane Design B	317.40	1933.4984	316.63	1922.4314	315.54	1906.7651
Capric Acid Design A	360.32	1208.5012	359.85	1207.0382	356.57	1196.8285
Capric Acid Design B	360.65	1209.5284	360.31	1208.4701	359.73	1206.6647

Table 6.3: Final temperature and heat absorbed for all materials, all velocities and both designs for the bottom sphere

	Bottom Sphere					
	Velocity = 0.1m/s		Velocity = 0.05m/s		Velocity = 0.01m/s	
Material	**Final Temp. (K)**	**Heat Abs. (J)**	**Final Temp. (K)**	**Heat Abs. (J)**	**Final Temp. (K)**	**Heat Abs. (J)**
Paraffin Wax Design A	330.30	1777.4215	328.05	1746.4964	308.43	1476.8300
Paraffin Wax Design B	332.94	1813.7069	331.22	1790.0664	323.71	1686.8455
nOctadecane Design A	315.44	1905.3278	313.33	1875.0012	300.26	1687.1489
nOctadecane Design B	318.32	1946.7214	317.02	1928.0368	311.08	1842.6624
Capric Acid Design A	360.04	1207.6296	359.06	1204.5791	341.41	1149.6395
Capric Acid Design B	360.59	1209.3416	360.09	1207.7853	356.81	1197.5755

6.3 Discussion

6.3.1 Final Temperature Analysis: Velocities

Figure 6.1 for paraffin wax shows the effect the velocity has on the system. The slower the velocity, the more the system lags and the lower the maximum temperature reached. This is also demonstrated in Tables 6.1 to 6.3, where the lower velocity consistently decreases the final temperature for Designs A and B, and for the other materials.

The effect of the velocity in the centre and top spheres is similar, as the differences in temperatures for the highest and lowest velocity results are very close for both designs. Starting with Design A, for paraffin wax, the difference results in 7.69K for the centre sphere (331.24K – 323.55K) and 7.22K for the top sphere (331.64K – 324.42K). For nOctadecane, the difference is coincidentally 5.8K for both centre and top positions (316.34K – 310.89K and 316.69K – 310.89K, respectively). Lastly, for capric acid the difference is 2.67K for the centre sphere (360.24K – 357.57K) and 3.75K for the top sphere (360.32K – 356.57K). These differences are approximately 1 – 2% of the final temperatures.

As seen in Figures 6.2 and 6.3, still for Design A, the effect of the velocity starts to become a real issue when looking at how the lag affects the bottom sphere. Whereas the lag for the bottom position at the highest velocity is roughly only 10s, the lag at the lowest velocity has an 100s delay. This reflects on the bottom sphere final temperatures, which are very harshly negatively impacted. For paraffin wax, these fall from 330.30K to 308.43K, a difference of 21.87K. This is applies to the other materials, where nOctadecane decreases from 315.44K to 300.26K by 15.18K, and for capric acid from 360.04K to 341.41K by 18.63K. These differences come up to roughly 4 – 6% of the final temperatures.

Looking now at the Design B, it is noted that the addition of a second inlet allows the fluid to penetrate and heat up the system faster, as seen by the higher temperatures in Tables 6.1 to 6.3. For this design, the differences between the centre and top sphere are not similar and vary significantly. The differences in temperature for Design B also are smaller than for Design A, and this is especially noticeable for the bottom sphere. The harsh decrease that the first design was experiencing is reduced for Design B for all materials. Paraffin wax only experiences a difference of 9.23K (332.94K – 323.71K) as opposed to the 21.87K. For nOctadecane, the difference results in 7.24K (318.32K – 311.08K), as opposed to 15.18K. Lastly, capric acid has the lowest temperature difference, with a value of 3.78K (360.59K – 356.81K), which does not vary that much from the difference at the centre sphere which equated to 2.15K (360.43K – 358.28K).

Thus, paraffin experiences a harsher difference between velocities, followed by nOctadecane and finally capric acid. This applies to both designs and for all positions, except the bottom, where capric acid suffers a higher difference than nOctadecane.

6.3.2 Final Temperature Analysis: Designs

Previously mentioned, the difference between Design B yields higher final temperatures than Design A. For top and centre spheres, the difference in temperatures is less than 1K, so can be classified as negligible. For example, for paraffin wax at a velocity of 0.1m/s the difference between the centre sphere temperatures goes from to 316.34K and 316.67K for design A and B, respectively. This difference is only 0.33K, which equates to 0.1% reduction in temperature. This is further demonstrated in Figure 6.4, where the lines are practically superimposed. Therefore, the only place where the system truly benefits from having a second outlet, is at the bottom sphere position, where the difference goes up to 2.64K (332.94K – 330.30K) for paraffin wax and 2.88K (318.32K – 315.44K) for nOctadecane. Nevertheless, these differences are still minimal as they equate to less than 1% of the final temperature. Therefore, the addition of an extra outlet is not worth the results.

6.3.3 Final Temperature Analysis: Materials

Out of all the materials, the highest final temperature was reached by capric acid (Farid et al. 2004) (Saeed et al. 2016), for Design B, top sphere, at the highest velocity of 0.1m/s with a value of 360.65K. The lowest was reached by nOctadecane, for Design A, at the slowest velocity of 0.01m/s with a value of 300.26K. The difference between highest and lowest temperature for all tests was 60.39K, a reduction of roughly 16%. Overall, nOctadecane took the longest to charge the system, whereas capric acid had a steep gradient and charged the fastest. Paraffin wax performed well and achieved temperatures ranged approximately between the ones for the other two materials (Rolka et al. 2021) (Sun et al. 2018), with a highest temperature of 332.58K and a lowest of 308.43K. Nonetheless, all materials show different heating dynamics, seen in Figure 6.5.

6.3.4 Heat Absorbed Analysis: Velocity

In terms of heat absorption per sphere, the lower the velocity of the heat transfer fluid, the lower the heat absorbed. Similarly to the pattern for the final temperatures, the heat absorbed in the top and centre sphere has values which do not differ significantly one from another, but drops for the bottom sphere.

6.3.5 Heat Absorbed Analysis: Design

Once again, Design B shows to have a higher heat absorption per sphere than Design A for all materials. However, the difference is very small for all materials, all velocities and all positions. For example, for a velocity of 0.05m/s, for the centre sphere, nOctadecane has a difference of 4.31J (1909.21J – 1904.90J) which corresponds only to a 0.2% difference. For the setup, but focusing on the top sphere now, the difference is 12.79J (1922.43J – 1909.64J) at roughly 0.7%, which is slightly higher, but still negligible. Even the biggest difference that occurs for the bottom sphere that equates to 53.4J at 2.8% (1928.04J – 1875.00J) is still relatively small.

6.3.6 Heat Absorbed Analysis: Materials

The material which absorbed the highest amount of heat was nOctadecane, for Design B, for the bottom sphere, at the highest velocity 0.1m/s with a value of 1946.72J. The material which absorbed less heat was capric acid, for Design A, for the bottom sphere, at the lowest velocity with a value of 1149.64J. The difference between the highest and lowest heat absorbed was 796.82J, a reduction of roughly 41%. This difference is very significant. Again, overall paraffin wax got values between the ranges of the other two materials, but the heat absorption values were much closer to the nOctadecane than capric acid. For example, the difference between the Design A, velocity 0.1m/s, top sphere between nOctadecnae and paraffin wax is 127.92J, whereas for the same setup the difference between paraffin wax and capric acid was 582.09J. Out of all the materials, nOctadecane had the highest latent heat (243.5kJ/kg) and capric acid had the lowest (152.7kJ/kg), which indicates the latent heat contributed positively to the heat absorption per sphere. Similarly, a high specific heat capacity contributed positively to the heat absorbed in regards to sensible heat before and after phase change, as capric acid had a very low value of 475.59kJ/kgK (liquid and solid). The other two materials had similar values for specific heat capacity, where paraffin wax excelled in cp of the solid (2200kJ/kgK) and nOctadecane did in cp of the liquid (2196kJ/kgK). This suggests that perhaps the high cp of the liquid positively influenced heat absorption as nOctadecane absorbed the most heat. Although a high density is also an important factor to consider for high sensible heat absorption, capric acid had the highest density with 878kg/m^3, suggesting this that perhaps other factors were more influential. A wider range of densities would be needed to study this further.

In conclusion, even though certain materials performed well, it was unclear and difficult to visualise which material properties were influencing the performance of the system in terms of final temperature and heat absorbed per sphere. From that point, the idea of focusing on varying one parameter to see its unique influence arose. Therefore, the idea of “constructing” materials by making their parameters “user-defined” was the natural progression.

6.4 References for this section:

M. M. Farid, A. M. Khudhair, S. A. K. Razack, S. Al-Hallaj. (2004). A review on phase change energy storage: materials and applications. *Energy and Conversion Management, 45,* 1597-1615. doi: 10.1016/j.enconman.2003.09.015

R. M. Saeed, J. P. Schlegel, C. Castano, R. Sawafta. (2016). Uncertainty of Thermal Characterization of Phase Change Material by Differential Scanning Calorimetry Analysis. *International Journal of Engineering Research & Technology (IJERT), 5,* Issue 01. ISSN: 2278-0181

P. Rolka, T. Przybylinski, R. Kwidzinski, M. Lackowski. (2021). The heat capacity of low-temperature phase change materials (PCM) applied in thermal energy storage systems. *Renewable Energy, 172,* 541-550. doi: 10.1016/j.renene.2021.03.038

X. Sun, K. O. Lee, M. Medina, Y. Chu, C. Li. (2018). Melting temperature and enthalpy variations of phase change materials (PCMs): a differential scanning calorimetry (DSC) analysis. *Phase Transitions, 91*, Issue 6. doi: 10.1080/01411594.2018.1469019

VII. Material Construction Results

The temperatures throughout the 60 minutes were extracted, revealing most cases had reached or been close to reaching the HTF inlet temperature. Furthermore, using Equation 6.1, the heat absorption was calculated for each tested case. All results were then further analysed and plotted in OriginPro, seen in Figures 7.1 to 7.3. Again, the results presented are only for the centre sphere.

Table 7.1: Final temperature and heat absorbed for tested materials

Material Code	Final Temperature Reached [K]	Heat Absorbed (Centre Sphere) [J]
C1	363.14	2,284.05
CL1	363.14	1,040.65
CL2	363.15	4,247.25
CTM1	363.12	2,310.37
CTM2	363.15	2,257.87
CD1	363.15	1,713.14
CD2	363.12	2,854.70
CE1	363.15	780.49
CE2	363.14	1,300.63
CE3	363.15	3,185.76
CE4	362.59	5,299.52

Table 7.2: Final temperature and heat absorbed for specific heat capacity combinations only

Material Code	Final Temperature Reached [K]	Heat Absorbed (Centre Sphere) [J]
CCP1	363.15	2,120.57
CCP2	363.15	1,963.49
CCP3	363.15	2,225.29
CCP4	363.15	1,930.76
CCP5	363.14	2,316.77
CCP6	363.15	1,767.14
CCP7	363.15	2,258.01

Table 7.3: Final temperature and heat absorbed for thermal conductivity combinations only

Material Code	Final Temperature Reached [K]	Heat Absorbed (Centre Sphere) [J]
CK1	363.14	2,284.05
CK2	363.15	2,284.19
CK3	362.31	2,272.10
CK4	363.15	2,284.19
CK5	363.15	2,284.19
CK6	362.26	2,271.38
CK7	363.15	2,284.19
CK8	362.47	2,274.40
CK9	363.15	2,284.19
CK10	363.15	2,284.19
CK11	363.14	2,284.05

7.1 Graphical Temperature Analysis

7.1.2 Melting temperature, Density and Latent Heat

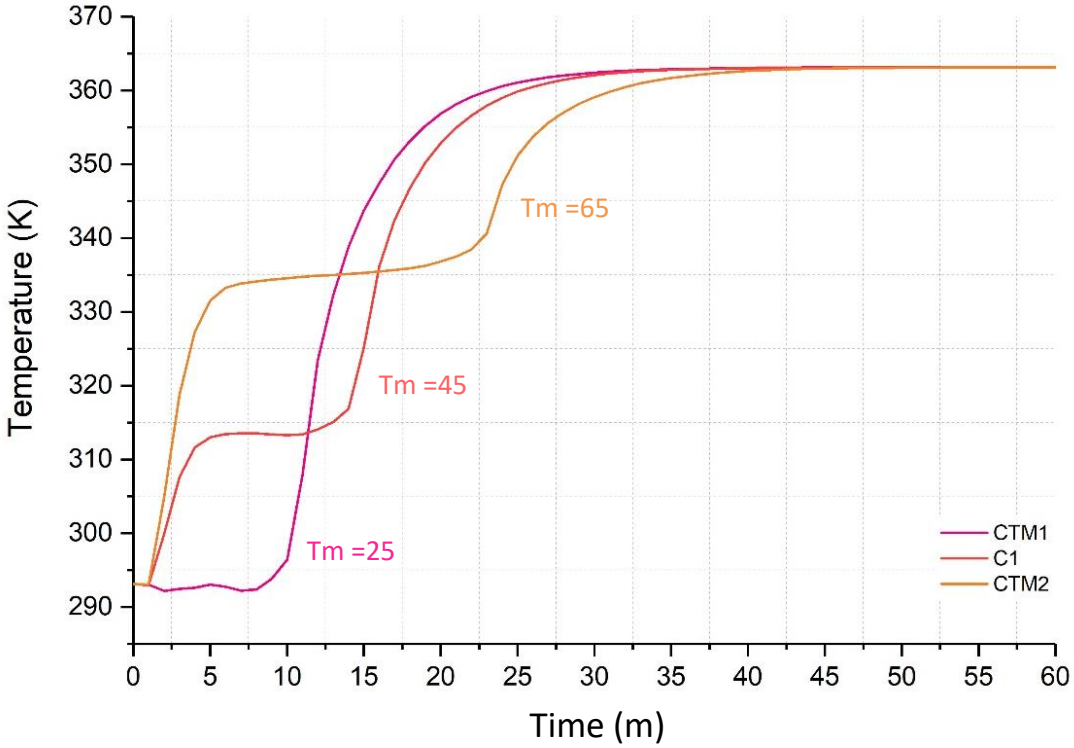

Figure 7.1: The effect of melting temperature on the final temperature

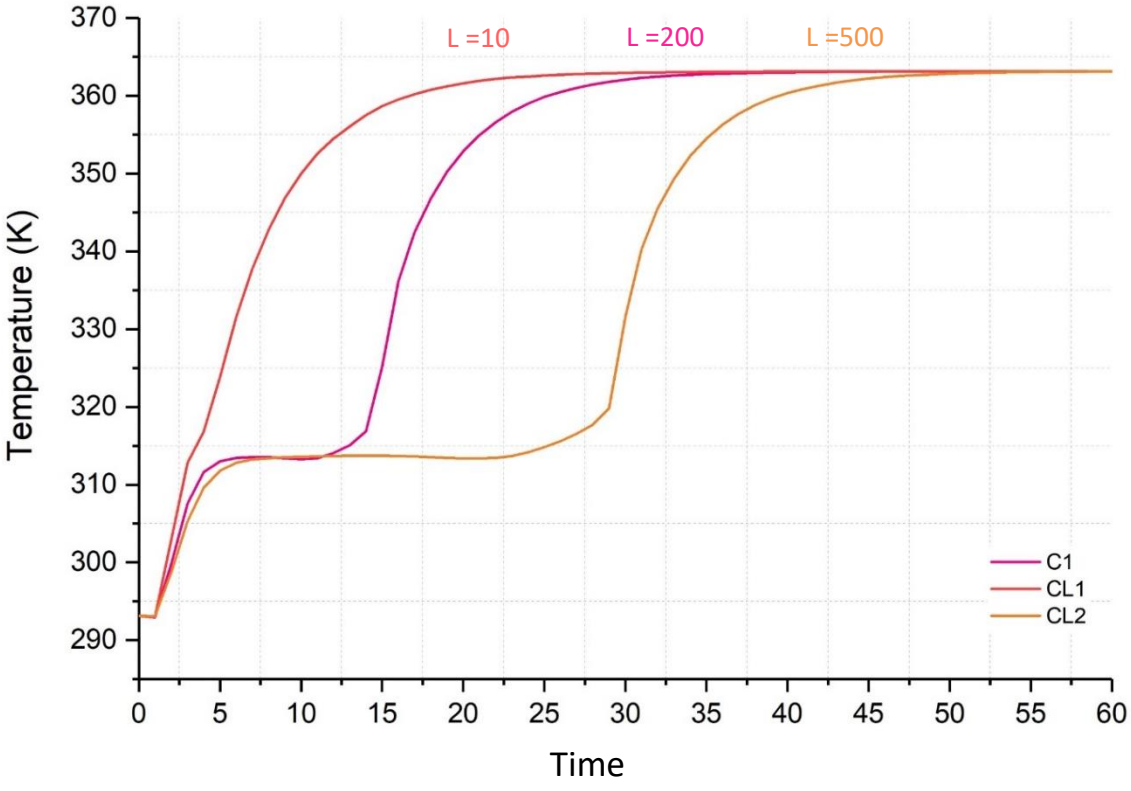

Figure 7.2: The effect of latent heat on the final temperature

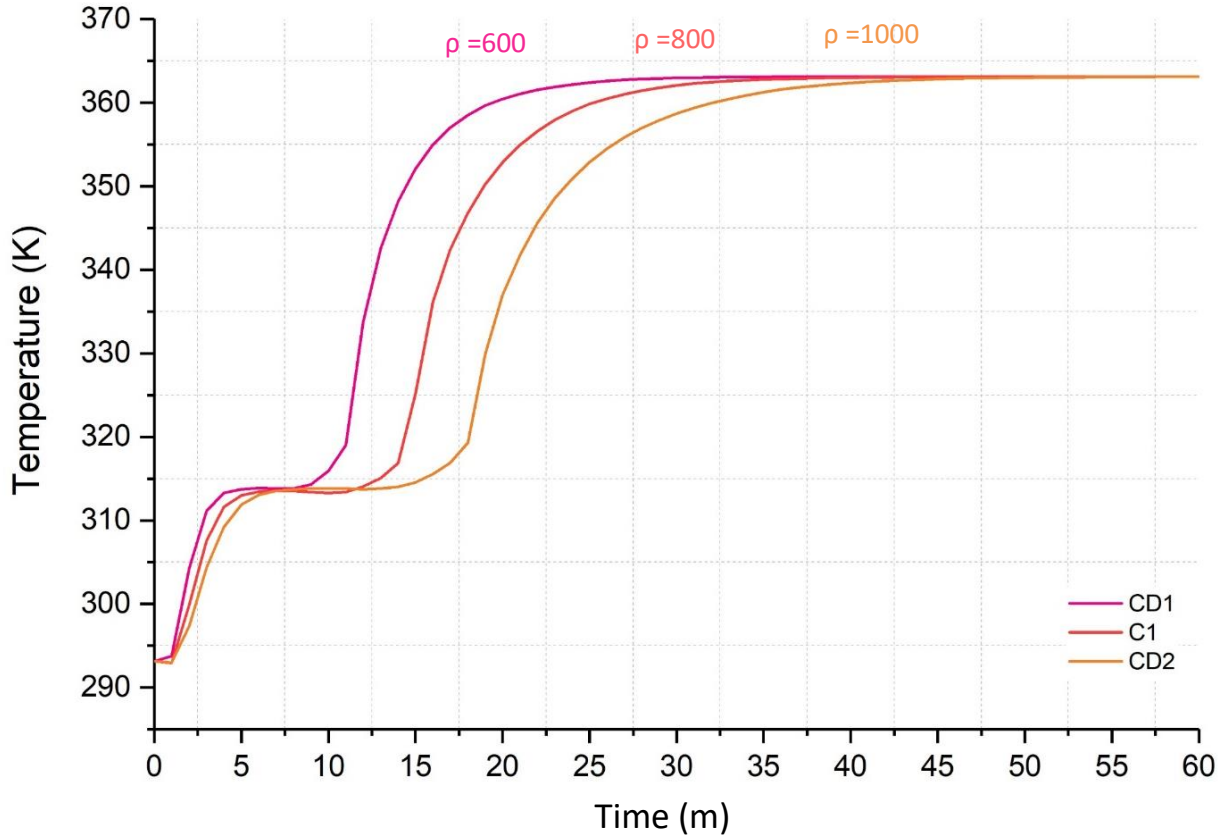

Figure 7.3: The effect of density on the final temperature

7.1.3 Graphical Temperature Analysis: Specific heat capacity and thermal conductivity

For the thermal conductivity and the specific heat capacity, which are properties that vary before and after phase change, another set of graphs were plotted. Due to the amount of cases and nature of the results, these graphs were plotted as contours. These enabled a better visual representation on their effect and an easier distinction in finding the relationship between the final temperature or heat absorbed and the property. The temperatures recorded for the contours are for a time of 20 minutes into the simulation, and again, for the centre sphere only. Find Figures 7.4 to 7.9 below:

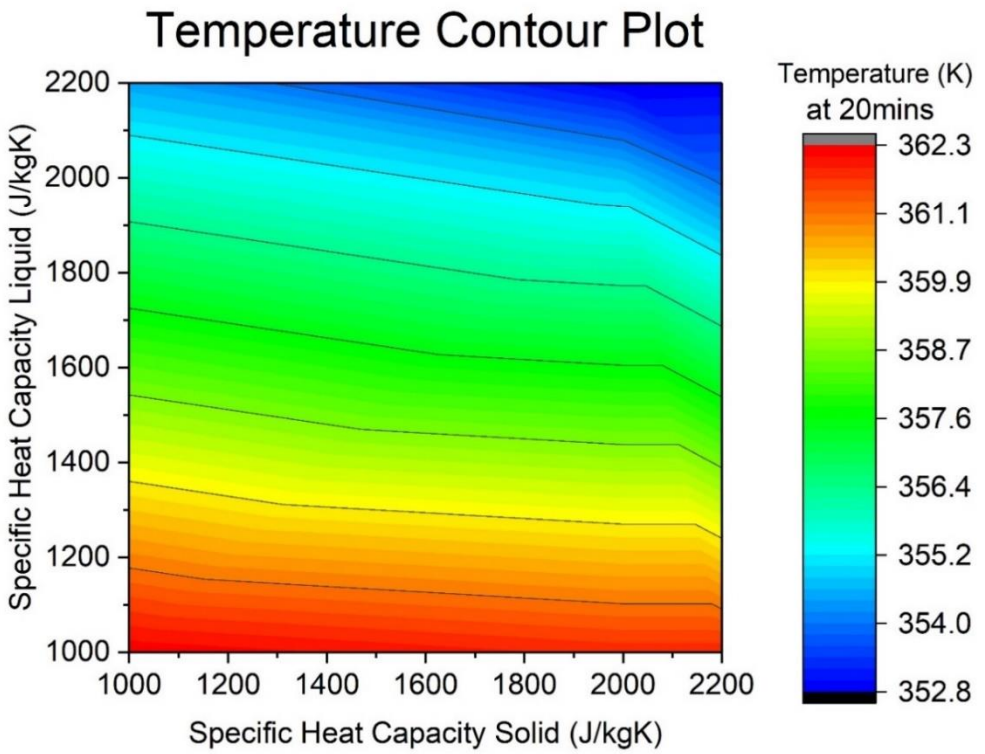

Figure 7.4: Temperature contour plot of specific heat capacity of the solid vs specific heat capacity of the liquid

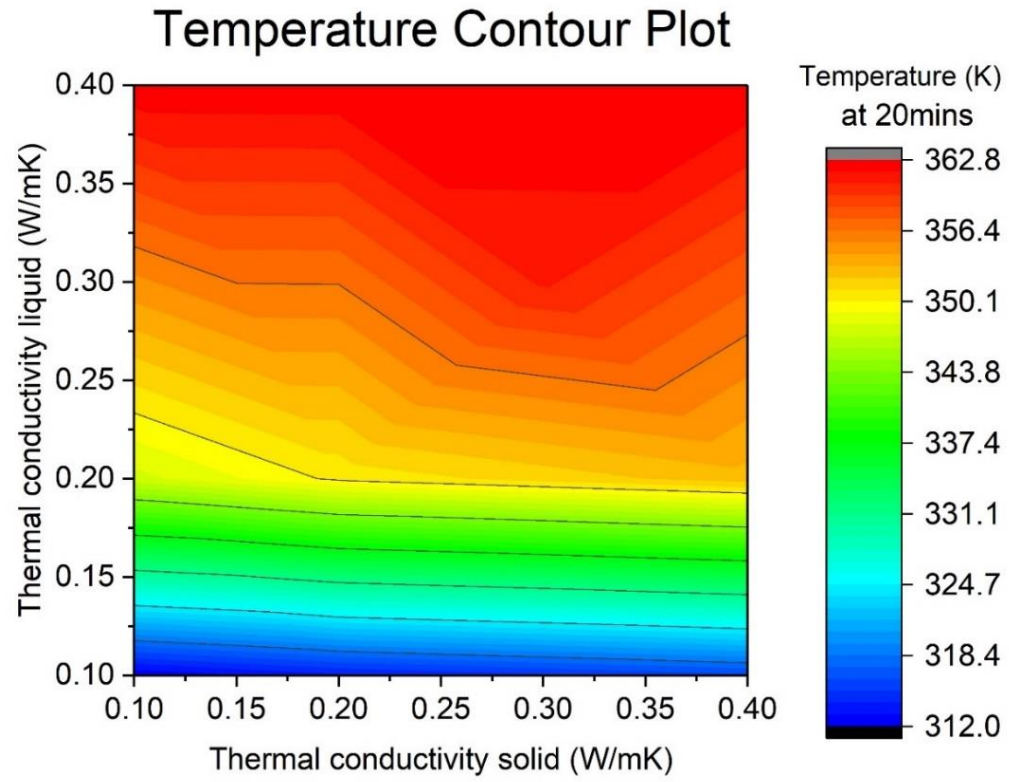

Figure 7.5: Temperature contour plot of thermal conductivity of the solid vs thermal conductivity of the liquid

7.1.4 Temperature and Heat Absorbed Analysis: Combined latent heat and density

The simulations coded CE1 to CE4 were also plotted individually in two separate contours, one for temperature and another for heat absorption. Furthermore, two line plots comparing them both were also plotted.

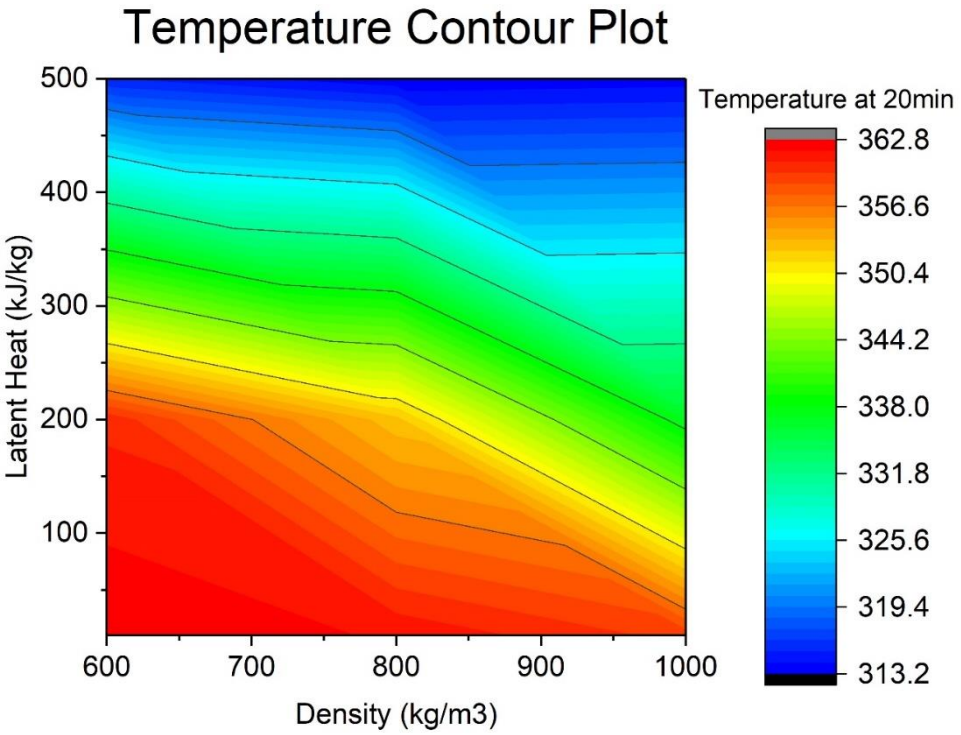

Figure 7.6: Temperature contour plot of latent heat vs density

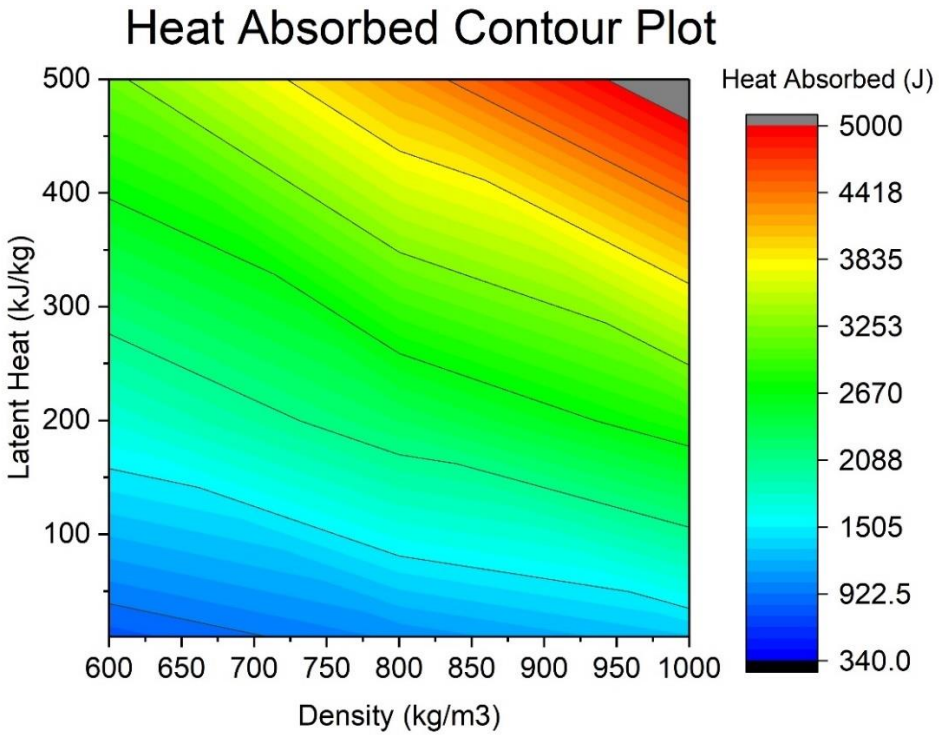

Figure 7.7: Heat absorbed contour plot of latent heat vs density

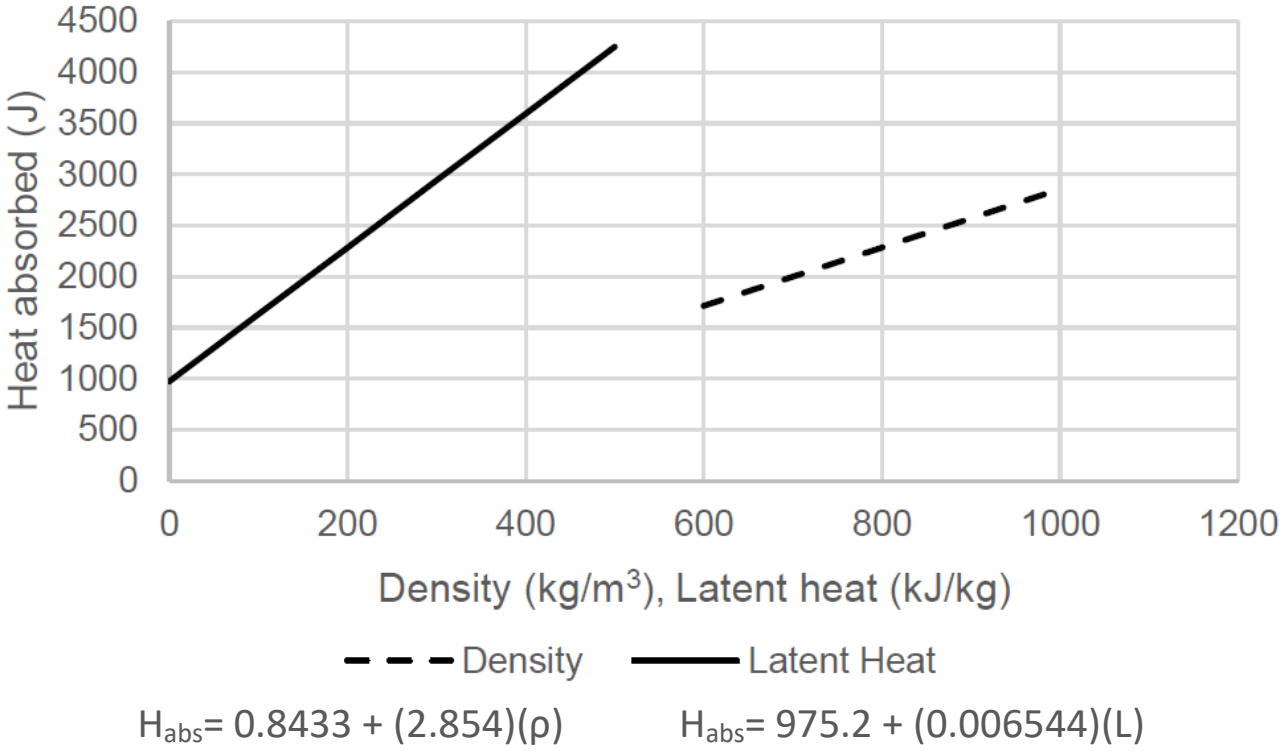

Figure 7.8: Line plot of the heat absorbed (after 60mins) against latent heat and density

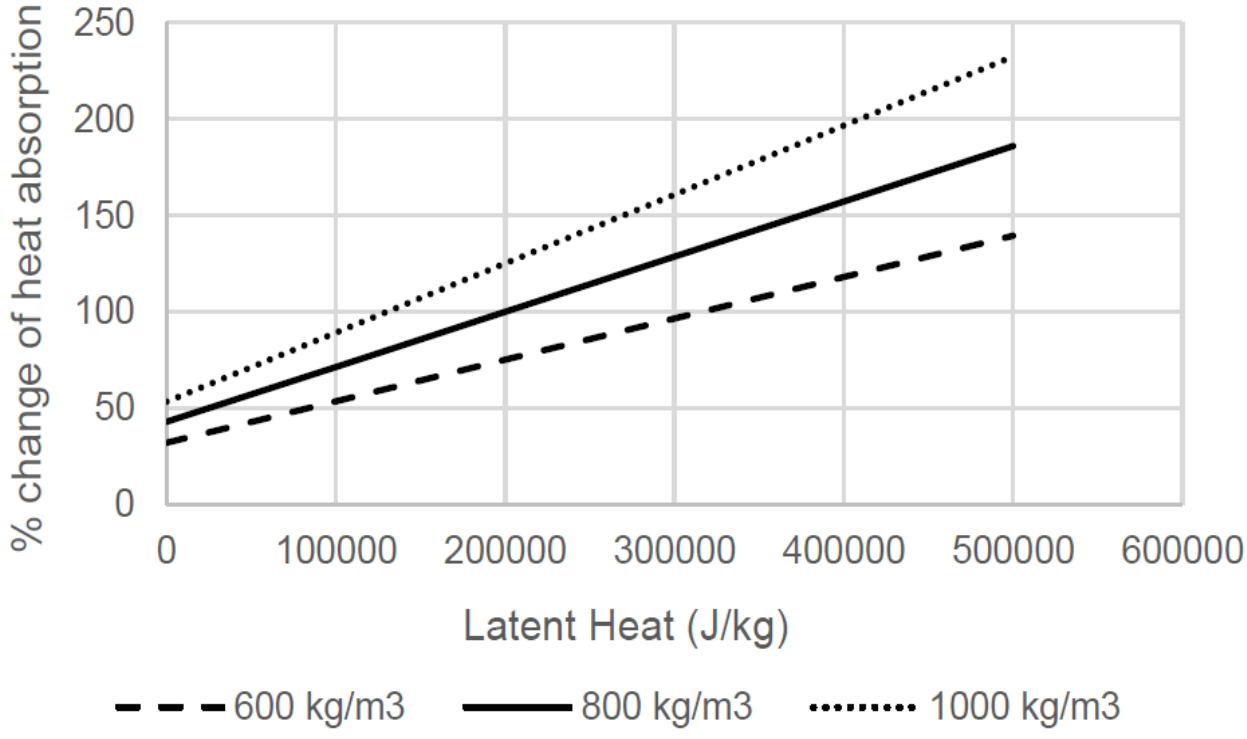

Figure 7.9: Percentage change of the heat absorbed compared to the base case

7.2 User-defined PCM: Discussion

7.2.1 Melting temperature

Trends in Figure 7.1 show different heating dynamics for the melting temperature even if the general shape of the lines is similar. Firstly, code CTM2 with a melting temperature of 65°C, is the fastest one to charge, denoted in the steep gradient. It reaches its phase change temperature of roughly 335K at a time of 5 minutes. The simulation with the second fastest charging time is our base case, C1 with a melting temperature of 45°C, reaching a temperature of 315K at approximately 4 minutes, before commencing phase change. CTM1 with a melting temperature of 25°C, due to having the lowest melting point, exhibits the phase changes almost immediately after just 2 minutes as the simulation starts. As melting takes place at low temperature, the subsequent heating of the liquid is sensible, and therefore linear in nature.

Furthermore, materials CTM1 and C1 take approximately 10 minutes and 7 minutes, respectively, to phase change from solid to liquid, a difference of 3 minutes. This is not the case for CTM2 that takes twice as much time at 20 minutes (from 5 minutes to 25 minutes) which is a considerable amount. Additionally, all materials heat up until they are in thermal equilibrium with the heat transfer fluid, at a temperature of 363K; however charging times are different. The fastest one to reach the maximum temperature is CTM1 at 30 minutes, followed by C1 at 35 minutes and finishing with CTM2 at 42 minutes. This suggests that the material with the lowest melting temperature reached maximum temperature the fastest. Looking at the previous Table 7.1, CTM1 also had the highest heat absorption value per sphere, with a value of 2,310.37J. The lowest heat absorption was found for CTM2, which reached a value of 2,257.87J, a difference of 52.5J. This implies that the higher the melting temperature, the slower the charging time and the less heat absorbed. Also, it indicates that in materials with similar latent heat, the dominant amount of heat absorption occurs as sensible heating of the liquid phase.

7.2.2 Specific Heat Capacity

Exploring the specific heat capacity considers different properties before and after phase change. Therefore, a contour graph was plotted showcasing the effect of both specific heat capacity of the solid and the liquid on the final temperature and charging time. Figure 7.4 suggests that the higher the value of the specific heat capacity of the liquid leads to the lower the final temperatures. The system will charge faster when the specific heat capacity liquid value is lower. Hence, the liquid thermal parameters have a heavier influence over the system behaviour, denoted in near to horizontal lines and the high temperature area at the bottom of the graph. Maximum temperatures reached are

approximately 361K, with the minimum values around 350K. The difference of 11K was observed between the maximum and minimum specific heat capacity cases.

7.2.3 Thermal Conductivity

The effect of thermal conductivity, like specific heat, was analysed on a contour graph as the material property changes before and after phase change. Figure 7.5 indicates that, opposite to the specific heat capacity, the higher the thermal conductivity of the liquid, the higher the final temperature reached. This is denoted in the almost horizontal lines in the contour diagram and the low temperature section at the bottom of the chart, which show that the effect of the thermal conductivity of the solid plays a limited part in the final temperature outcome. Nonetheless, it is worth noting that the specific heat contour grey lines in Figure 7.4 show a more visible negative gradient as opposed to the near horizontal thermal conductivity ones. This portrays the idea that the specific heat capacity of the solid is more influential over the final temperature than the thermal conductivity of the solid is for its counterpart (Figures 7.4 and 7.5), since it has a larger effect over the shape of the contour graph. The highest temperatures reached are approximately 360K, whereas the minimum values were around 330K. This 30K difference proves that the thermal conductivity of the liquid greatly influences the outcome of the final temperature and can lead to longer charging time if material has low thermal conductivity value. However, looking at the thermal conductivity of the solid, the maximum difference found was more than 5K. Cases with high liquid thermal conductivity values were close to reaching the temperature of the HTF, where the temperature increase of the centre sphere was fond to be 66.85K. Yet high solid thermal conductivity values led to a smaller increase of 36.85K. This difference of 30K, as opposed to the 11K found in the variation of the specific heat capacity, suggests thermal conductivity has greater influence on the charging time of the system.

7.2.4 Density and Latent Heat

In Figure 7.2, it is obvious that increasing the latent heat has a negative impact on the final temperature and leads to higher charging time. For CL1, with a latent heat of 10kJ/kg, the charging time is approximately 27 minutes, and the HTF temperature is reached. This is significantly different to CL2, with a latent heat of 500kJ/kg, where charging takes 52 minutes. This shows that a difference in latent heat of 490kJ/kg result in an increase in charging time of 25 minutes. Focusing on the areas under the graph, which represent the maximum heat absorption, it is clear though that CL2 shows higher heat absorption, denoted in the long horizontal line representing the material undergoing phase change. Where CL1 only takes 2 minutes to phase change, CL2 takes roughly 25 minutes. This is reflective of the data in Table 7.1, where the highest heat absorption value was 4,247.25J for CL2, followed by 2,284.05J for C1 and finishing at 1,040.65J for CL1. The difference between the maximum

and minimum value is 3,206.60J. Lastly, in terms of heating dynamics they remain mostly unchanged with similar growth gradients.

The effect of density, in Figure 7.3, reveals similar trends. As the density increases, the system charging rate decreases and it takes for the spheres to reach the inlet temperature of the HTF. This is seen by CD2, which has the largest density with a value of 1000kg/m^3. The increase in density has a negative impact on the final temperature and charging time. The heat absorption increases with density as shown in Table 7.1, with the highest heat absorption being 2,854.70J for CD2, followed by 2,284.05J for C1 and lowest 1,713.14J for CD1. The density appears to have lesser influence on the heat absorption compared to the latent heat on the system, denoted in the smaller difference between maximum and minimum values. CD1 reaches maximum temperature at roughly 27minutes, and CD2 reaches maximum temperature at approximately 42 minutes, a difference of 15minutes. Previously, the difference between latent heat extremes (10kJ/kg to 500kJ/kg) was 25minutes, which is significantly larger. This is visible by the proximity of the lines in Figure 7.3. Furthermore, the difference between the heat absorptions per sphere is 1,141.56J for the density range (600kg/m^3 to 1000kg/m^3), which is almost a third less than the difference for the latent heat range (3,206.60J). The overall heating dynamics remain unchanged as the lines in Figure 7.3 appear to be almost parallel and follow the same charging shape.

Examining both parameters side by side in the contour plots Figure 7.6 and 7.7, helped in visualising the direct influence of the thermal parameters regarding the studied outputs. They demonstrate that both high latent heat and density will positively influence the heat absorption per sphere, denoted in the red top right corner in Figure 7.7. However, there will be a compromise to the charging time, denoted by the top right corner in Figure 7.6 which shows the low temperature area. A wide range of values from 340J to 5,000J in the legend on Figure 7.7 denotes the importance of these parameters. This is in line with the underlying theory, as high density values positively influence all the sensible heat absorption, and high latent values exert the same effect for the latent heat.

Using the heat absorbed calculated data, a line of best fit with preliminary equations were found (Figure 7.8). The relationship between the plotted parameters (density and latent heat) and heat absorbed is linear for both and gives insight on how thermal parameters quantitatively affect heat absorption. The change in latent heat shows a wider range in values in terms of heat absorption, compared to the density's data range. This again helps that idea that the latent heat value exerts the most influence in this system. However, the y-intercept is much larger on the latent heat (975.2), indicating that if the parameter is set to zero, the system could still absorb heat independently, whereas for the density if the value is set to zero the heat absorbed value drops drastically (0.8433).

This is due to the system studied does not only consider latent heat absorption, since in the model studied the material first absorbs heat sensibly until it reaches the phase change temperature.

The percentage change of heat absorption values tested compared to the base case was calculated and plotted in Figure 7.9. The highest percentage change from the base case was roughly 230%, where the values for density and latent heat were highest. The lowest percentage change, with the lowest density and latent heat values, was 34%. The largest percentage difference for a fixed density was 175% for the 1000kg/m^3 test. Equally, the largest percentage difference for a fixed latent heat was 92%. Consequently, even though the latent heat appears more dominant factor, the density does not fall far behind as a key parameter. To better understand the extent of the influence of thermal properties on heat absorbed and charging temperatures, a detailed regression analysis was performed.

7.3 User-defined PCM: Regression Analysis

The regression analysis is a mathematical method which establishes a best fit relationship between the output, which in this system is temperature or heat absorption, and the inputs, which are melting temperature, thermal conductivity (solid and liquid), specific heat capacity (solid and liquid), density, latent heat and time. This type of analysis is invaluable in evaluating which input has the largest effect on the system and if they are any relevant interactions between the predictors and the output. A predictor is the independent variable linked to the output. Additionally, it provided an equation relating them both which gives insight on how much variation in the output is related to the predictors. The software used for this was MiniTab and there are two methods employed to develop mathematical equations for the model. The first is a step regression “assistant” model, which allows for a maximum of five predictors for each output. The other method used was the “fitted” one, where there is no limit on the number of predictors yet creates a linear fit for the dataset.

Outputs, inputs and combinations for the regression analysis are presented in Table 7.4. R^2 and p-values are shown. The R^2 value is a measure which expresses the deviation in the dependant variable explained by the independent variables in the regression model. A high R^2 value usually indicates that the model fits the studied data well. A p-value tests the null hypothesis, which determines if the output has any correlation to the predictors. A low p-value indicates evidence against the null hypothesis, meaning the relationship between output and inputs is significant (Agrawal, 2018).

All equations were tested by inputting the user-defined material parameters and compared the results to the heat absorbed and temperature simulation results. Although some of the equations have high R^2 values, not all were an adequate fit. Likewise, some equations that had lower R^2 values,

presented significantly accurate temperatures which were close to the original ones. These R^2 values were calculated automatically by the software and were not always an accurate measure of how well the equations fit. Depending on how accurately they represented the original COMSOL model, the equations were classified as “Excellent”, “Good” or “Poor”. This was based on the percentage error between the original results and the equation ones. If the error was up to 5%, the equations were classified as excellent, if they were up to 25% they were classified as good and if they values exceeded 50% they were classified as Poor and deemed unusable. Equations are showcased for Excellent and Good fits only.

Table 7.4: Output and inputs for the regression analysis combinations, alongside their R^2 and p values

Output	Inputs	Data Set	Method	Equation	R^2 value	P value	Results
Heat Absorbed	k (solid), k (liquid), Density, Latent heat, Melting temperature	All	Fitted	7.1	94.41%	< 0.001	Excellent
Heat Absorbed	Cp (solid), Cp (liquid), Latent Heat, Density, Melting temperature	All	Fitted	7.2	96.46%	< 0.001	Excellent
Temperature	Time, Cp(solid), k(solid), Latent heat, Density	All	Assistant	N/A	83.45%	< 0.001	Poor
Temperature	Time, Cp(liquid), k(liquid), Latent heat, Density	All	Assistant	N/A	86.59%	< 0.001	Poor
Temperature	Time, Cp(solid), k(solid), Latent heat, Density	All	Fitted	N/A	66.56%	< 0.001	Poor
Temperature	Time, Cp(liquid), k(liquid), Latent heat, Density	All	Fitted	7.3	68.64%	< 0.001	Good
Temperature	Time, Cp(liquid),Cp(solid),Latent heat, Melting temperature, k(liquid), k(solid), Density	All	Fitted	7.4	69.34%	< 0.001	Good
Temperature	Time, Cp(solid), k(solid), Melting temperature, Density	Before melting	Assistant	7.5	83.05%	< 0.001	Good
Temperature	Time, Cp(solid), k(solid), Melting temperature, Density	Before melting	Fitted	7.6	63.05%	< 0.001	Excellent
Temperature	Time, Cp(solid), k(solid), Melting temperature, Density, Latent Heat	Before melting	Fitted	7.7	65.33%	< 0.001	Excellent
Temperature	Time, Cp(liquid), k(liquid), Melting temperature, Density	After melting	Assistant	N/A	53.45%	< 0.001	Poor
Temperature	Time, Cp(liquid), k(liquid), Melting temperature, Density	After melting	Fitted	7.8	34.93%	< 0.001	Good
Temperature	Time, Cp(liquid), k(liquid), Melting temperature, Density, Latent Heat	After melting	Fitted	7.9	37.93%	< 0.001	Good

The relevant equations for each combination case that were extracted:

Equation 7.1: $Q = -1599 + 0.006581(L) + 3.146(\rho)$

Equation 7.2: $Q = -2259 + 0.3238(Cpl) + 0.006541(L) + 3.146(\rho)$

Equation 7.3: $T = 336.66 - 0.01957(\rho) - 0.000038(L) + 1.0456(t) - 0.003915(Cpl) + 47.37(kl)$

Equation 7.4: $T = 326.70 + 52.50(kl) + 19.50(ks) - 0.01957(\rho) - 0.000040(L) - 0.002665(Cpl) + 1.0456(t)$

Equation 7.5: $T = 151.0 - 0.01475(Cps) + 70.9(ks) - 9.35(t) - 0.01341(\rho) + 0.4900(Tmelt) + 0.000004(Cps^2) - 86.8(ks^2) - 0.06481(t^2) - 0.983(ks)(t) + 0.001249(t)(\rho) + 0.03466(t)(Tmelt)$

Equation 7.6: $T = 52.2 + 16.33(ks) + 0.8087(Tmelt) - 0.01059(\rho) - 0.00220(Cps) + 0.7873(t)$

Equation 7.7: $T = 61.3 + 20.54(ks) + 0.7809(Tmelt) - 0.01064(\rho) - 0.00175(Cps) + 0.8824(t) - 0.000013(L)$

Equation 7.8: $T = 353.96 - 0.00890(\rho) + 0.3363(t) - 0.002957(Cpl) + 26.52(kl)$

Equation 7.9: $T = 356.94 - 0.01006(\rho) + 0.3560(t) - 0.000014(L) - 0.003021(Cpl) + 27.09(kl)$

All cases show that the relationship between heat absorbed and/or charging temperature and thermal parameter values is statistically significant due to the low p value ($p < 0.1$). Furthermore, the R^2 values for the heat absorption are high, over 90%, with the temperature ones being lower yet still over 60% for all data and before phase change. Even though the post phase change equations had very low R^2 values of 30% to 40%, they still yielded satisfactory numbers. This demonstrates that the equations, except the ones tagged as "Poor", are a good fit for the model.

All tested equations for temperature as an output are presented in Tables 7.5. The material, code, C1, was tested for every time interval of 1 minute for the total simulation time of 60 minutes.

Table 7.5: Tested equation results deviation for code C1 for all times (only for temperature as an output)

	Tested Equations						
Deviation	**7.3**	**7.4**	**7.5**	**7.6**	**7.7**	**7.8**	**7.9**
RMS	3.61%	3.61%	1.38%	2.00%	1.93%	1.75%	1.74%
Minimum	-5.49%	-5.16%	-2.05%	-1.89%	-1.67%	-1.77%	-1.83%
Maximum	7.63%	8.02%	2.18%	3.74%	3.84%	7.88%	7.73%
Closest	0.08%	0.11%	0.05%	-0.47%	-0.05%	0.00%	-0.03%

Furthermore, all material codes were tested for temperature as an output for specific times (10minutes and 40minutes), and collected in Table 7.6:

Table 7.6: Tested equation results deviation for all material codes (only for temperature as an output)

	Tested Equations								
Code	**7.3 @10mins**	**7.3 @40mins**	**7.4 @10mins**	**7.4 @40mins**	**7.5 @10mins**	**7.6 @10mins**	**7.7 @10mins**	**7.8 @40mins**	**7.9 @40mins**
C1	3.64%	-1.91%	4.01%	-1.59%	0.09%	-0.73%	-0.37%	-1.08%	-1.08%
CL1	-5.16%	0.05%	-4.72%	0.48%	-10.40%	-11.14%	-10.10%	-1.11%	-0.37%
CL2	-0.09%	-4.34%	0.09%	-4.18%	0.00%	-0.82%	-1.70%	-0.34%	-1.50%
CTM1	9.55%	-1.92%	9.94%	-1.60%	0.15%	-0.53%	0.05%	-1.09%	-1.09%
CTM2	-2.95%	-1.81%	-2.60%	-1.49%	-1.27%	-2.21%	-2.03%	-0.98%	-0.98%
CCP1	3.44%	-1.90%	3.81%	-1.59%	0.76%	-0.22%	0.00%	-1.08%	-1.07%
CCP2	5.10%	-0.65%	4.99%	-0.75%	0.18%	-0.91%	-0.52%	-0.14%	-0.12%
CCP3	3.76%	-1.71%	4.05%	-1.46%	-0.04%	-0.86%	-0.49%	-0.94%	-0.93%
CCP4	5.08%	-0.65%	4.97%	-0.75%	0.03%	-0.79%	-0.42%	-0.14%	-0.12%
CCP5	3.49%	-1.90%	3.86%	-1.58%	0.08%	-1.01%	-0.62%	-1.07%	-1.07%
CCP6	5.01%	-0.65%	4.90%	-0.75%	0.82%	-0.16%	0.07%	-0.14%	-0.12%
CCP7	3.78%	-1.70%	4.06%	-1.45%	0.11%	-0.98%	-0.59%	-0.92%	-0.92%
CK1	4.09%	-1.88%	3.21%	-2.64%	-0.05%	-1.34%	-1.25%	-1.06%	-1.05%
CK2	-1.80%	0.66%	-1.17%	1.25%	-7.85%	-8.61%	-8.27%	0.34%	0.38%
CK3	2.13%	-1.37%	1.10%	-2.27%	-0.49%	-1.78%	-1.68%	0.06%	0.05%
CK4	0.45%	0.66%	-0.09%	0.17%	-6.29%	-7.50%	-7.41%	0.34%	0.38%
CK5	5.07%	-1.89%	3.56%	-3.18%	-0.24%	-0.94%	-0.98%	-1.06%	-1.06%
CK6	3.57%	-0.93%	1.90%	-2.39%	-0.21%	-0.91%	-0.95%	0.50%	0.49%
CK7	3.57%	0.66%	2.41%	-0.36%	-4.46%	-5.13%	-5.17%	0.34%	0.38%
CK8	1.71%	-1.74%	1.93%	-1.55%	-0.32%	-1.14%	-0.77%	-0.32%	-0.33%
CK9	4.52%	-0.64%	4.42%	-0.72%	-0.52%	-1.84%	-1.61%	-0.38%	-0.37%
CK10	4.96%	-0.64%	4.24%	-1.26%	-0.67%	-1.95%	-1.86%	-0.38%	-0.37%
CK11	3.72%	-1.89%	4.52%	-2.11%	0.16%	-1.17%	-0.94%	-1.07%	-1.06%
CD1	4.02%	-0.86%	4.38%	-0.54%	-0.68%	-0.89%	-0.52%	-0.62%	-0.55%
CD2	2.22%	-2.81%	2.58%	-2.49%	-0.14%	-1.58%	-1.21%	-1.39%	-1.45%
CE1	-5.78%	1.12%	-5.35%	1.54%	-11.98%	-12.16%	-11.14%	-0.63%	0.17%
CE2	-4.53%	-1.00%	-4.09%	-0.57%	-8.79%	-10.10%	-9.05%	-1.57%	-0.90%
CE3	1.12%	-3.94%	1.29%	-3.79%	0.02%	-0.19%	-1.06%	-0.56%	-1.65%
CE4	-1.28%	-1.35%	-1.11%	-1.19%	-0.01%	-1.44%	-2.32%	3.43%	2.15%
RMS	4.09%	1.77%	3.94%	1.85%	3.96%	4.41%	4.10%	1.02%	0.92%
MIN	-5.78%	-4.34%	-5.35%	-4.18%	-11.98%	-12.16%	-11.14%	-1.57%	-1.65%
MAX	9.55%	1.12%	9.94%	1.54%	0.82%	-0.16%	0.07%	3.43%	2.15%
CLOSEST	-0.09%	0.05%	±0.09%	-0.36%	-0.01%	-0.16%	0.00%	0.06%	0.05%

7.3.1 Heat Absorbed regression analysis

Two regression analyses with heat absorbed as an output were run, one focusing on the inputs excluding specific heat capacity and the other excluding thermal conductivity. From the equations, it is seen that the relationship of the heat absorbed to its predictors was simpler for the cases with thermal conductivity (Equation 7.1) than it was for the specific heat capacity (Equation 7.2). Nonetheless, they are both still linear in nature. Furthermore, in Equation 7.1, the thermal conductivity was excluded completely from the equation and treated as an irrelevant parameter to the heat absorbed, meaning the equation only had latent heat and density. However, for Equation 7.2, the specific heat capacity, specifically the liquid one, was included into the equation. This reinforces the idea that the liquid parameters are more influential in the system than its solid counterpart for this system since the melting point was closer to the initial temperature and the material spends most of its time at its liquid state. Melting temperature does not feature in any of the two equations. Nonetheless, melting temperature dictates how much charging time the material spends in its solid and/or liquid state.

In terms of coefficients, both equations share great similarities in the preceding multiplying numbers. The density coefficient is the same (**3.146**) in both equations. Latent heat has two similar terms, whose differences could classify as minimal. Equation 7.1 has a term of **0.006581** and Equation 7.2 has **0.006541**, a difference of **0.00004**. The negative terms **-1599** for Equation 7.1 and **-2259** for Equation 7.2, is much lower for Equation 7.2, as the regression included specific heat capacity and therefore is more accurate. This is due to specific heat capacity being an influential parameter in the material sensible heating stage.

Two heat absorbed equations are tested, using the base case C1's values as an example, the results are the following using Equation 7.1 and 7.2 respectively:

$$\mathrm{Q} = -1599 + (0.006581)(200{,}000) + (3.146)(800) = \mathbf{2{,}234.00J}$$

$$\mathrm{Q} = -2259 + (0.3238)(2200) + (0.006541)(200{,}000) + (3.146)(800) = \mathbf{2{,}278.36J}$$

Compared to the original value of **2,284.05J** from Table 7.1, these yield differences of **50.05J** (2.19%) and **5.69J** (0.25%). Although Equation 7.1 still provides a good estimate and can inform on the range expected for the heat absorption to fall into, it is not as reliable when comparing materials that have only subtle differences in their thermal parameters and the user wishes for a more exact calculation. However, for a more precise approach, Equation 7.2 offers an accurate method and the differences between values is minimal. Using this approach, the user can focus on two to three thermal parameters if their application is regarding heat absorption, allowing a much more amiable material

selection process, excluding thermal parameters of limited impact and the need for a lengthy numerical or experimental simulation.

7.3.2 Temperature regression analysis - Equations

The temperature regression proved to be significantly more complicated. Aside from having lower R^2 values, several more tests were run trying to find the most adequate combination of predictors and equation. It was not possible to determine a general equation to describe the overall charging dynamics of the system due to the complex shape of the graph. Another approach was employed where the regression analysis was carried out before and after melting and independent equations were found and assigned separately.

In Table 7.4 all combinations that were tried, including ones which failed, are shown. Using the same fitting method, Equation 7.3 was modelled using only liquid parameters in terms of specific heat capacity and thermal conductivity. Similarly, one of the failed cases used only solid parameters, yet the equation did not give correct results, which is interesting and helps support the thought that temperature for this model depends on and is affected most by its liquid parameters. However, none of the assisted regression methods worked when analysing the whole dataset, not even for the liquid parameters, independently of the high R^2 values.

Starting with equations that encompass the full dataset, Equations 7.3 and 7.4, many similarities are seen even though the latter has a larger amount of input parameters. The time coefficient is the same in (**1.0456**), as is the one for the latent heat (**0.000038** vs **0.000040**). Equation 7.3 features all the inputs, whereas Equation 7.4 does not and excludes melting temperature and specific heat capacity of the solid. This supports the idea that the liquid counterparts are mainly influencing the temperature output of the system. Seeing how the attempt to fit the model using the inputs time, Cp(solid), k(solid), latent heat and density failed, it demonstrates that the model cannot accurately represent all data without its liquid parts. Overall, both equations are simple, linear, and similar in terms of structure and coefficients.

Before phase change data, as opposed to data which only features post phase change or the entire range, had three functional equations instead of two. The assistant regression method gave a good fit, which included all inputs, and Equation 7.5 had significantly more complex, terms including squared values, compared to the other two equations (Equation 7.6 and 7.7). The term that appears the most frequently in Equation 7.5 is time (four times) followed by the thermal conductivity of the solid (three times) and lastly the rest of the parameters (twice). Looking at Equation 7.6, which had the same inputs as Equation 7.5 but used a different method, the differences are considerable. The

first term is significantly lower (**52.2** vs **151.0**) and the equation structure generally resembles previous ones (Equations 7.3 and 7.4). Introducing latent heat as an input in Equation 7.7 changes the coefficients, to compensate for the subtraction of the latent heat coefficient. The density coefficients (**0.01059** vs **0.01064**) and melting temperature (**0.8087** vs **0.7809**) are slightly different. Notable change is coefficients are observed for time (**0.7873** vs **0.8824**), thermal conductivity (**16.33** vs **20.54**) and specific heat capacity (**0.00220** vs **0.00175**). The equation structure remains the same.

After phase change equations are interesting, as the model was not fitted adequately in failed attempts (Table 7.4) using the almost the same inputs all the dataset yet managed a good fit for the post phase change data. The R^2 value for the fit was also very low, yet the differences are not extreme. The difference between Equation 7.8 and 7.9, is the addition of latent heat as an input. Evaluating coefficients, similar values can be found, such as **353.96** (Equation 7.8) and **356.94** (Equation 7.9). Others with smaller differences include specific heat capacity of the liquid (**0.002957** vs **0.003021**). Larger differences include time (**0.3363** vs **0.3560**), density (**0.00890** vs **0.01006**) and thermal conductivity (**26.52** vs **27.09**).

7.3.3 Temperature regression analysis - One material

Looking at the results for C1 in Table 7.5, the maximum deviation from the original value of 292.97K is **8.02%** in Equation 7.4 at the simulation time of 1minute. For both Equations 7.3 and 7.4 the biggest discrepancy occurred early in the initial time range of 0 to 2minutes. For Equation 7.3, however, the maximum discrepancy was lower at **7.63%**. Other higher maximum deviations include Equations 7.8 and 7.9 where values were **7.88%** and **7.73%**, respectively. These refer to the time just after the material phase change, 15minutes into the simulation, for both. Equations for before phase change provided a great fit, and maximum deviations include lower values of **2.18%, 3.74%** and **3.84%** for Equations 7.5, 7.6 and 7.7, respectively. For Equation 7.5 this happens at a time of 4minutes, whereas for the other two, they happen at 1minute for both.

Minimum divergence values in C1 are lower than the maximum ones for all equations. The lowest again occurred for Equations 7.3 and 7.4, with values of **-5.49%** and **-5.16%**, respectively. These both happened at a time of 23minutes. After these, the lowest in order are Equations 7.5, 7.6, 7.9, 7.8 and 7.7. Equations 7.5 to 7.7 had derivations of **-2.05%, -1.89%** and **-1.67%** happening at times 4minutes, 5minutes and 5minutes, respectively. Equation 7.8 and 7.9 had discrepancies of **1.77%** and **-1.83%**, that were the same percentage at both 28 and 29minutes into the simulation for both equations. Consequently, it is seen that before and after phase change equations are more accurate and a better fit than the equations which try to encompass all datasets.

Furthermore, values closest to the original simulated ones for C1 are all under 1%. The temperatures calculated from the extracted equations are compared to the COMSOL temperatures simulated for a given time, which can be any time in the simulated range (0minutes to 60minutes). In order, from Equation 7.3 to 7.9, the simulation times at which these values are closest are 47minutes and 46minutes (for the whole dataset), 10minutes, 12minutes and 12minutes (for before phase change only), and lastly 52minutes and 51minutes (for after phase change only). This suggests the equations for all data set model the final part of the charging more accurately. Similarly, before phase change it models the data approaching phase change more precisely. For after phase change data this is different as it models the data approaching the final temperature of the HTF most accurately.

7.3.4 Temperature regression analysis - All materials

Temperature regression models were applied to all material cases and tested for a set time. Selected times before and after phase change (10minutes and 40minutes), were chosen because they represent good points for all materials that are not on the verge of phase change (10minutes) or just after phase change (40minutes), where irregularities may occur. Results are gathered in Table 7.6.

Maximum divergence occurred in Equations 7.3 and 7.4 for the set time of 10minutes (**9.55%** and **9.94%**, respectively). The material code for these values is CTM1, where the melting temperature was 25°C, as opposed to 45°C. This is logical as if the material phase change happens earlier in the charging process, the equation struggles to capture the nature of the after phase change linear gradient. Other deviations are within the expected range.

The minimum deviations occurred in Equations 7.5 to 7.7 which represent the before phase change equations (**-11.98%, -12.16%** and **-11.14%,** respectively), and all coincided with the same material code which was CE1. CE2 and CL1 also give a high percentage deviation, like CE1. All these have in common that the latent heat was 10kJ/kg, as opposed to a more realistic value of 200kJ/kg or 500kJ/kg, so the system struggles to model such a low latent heat. However, this was a relatively extreme value, so the equation will function adequately for more realistic materials. The other equations do not struggle with these particular codes.

To summarise, a set of equations functional equations which provide accurate estimates for two set of outputs: charging temperature and heat absorbed per sphere. These equations are unique to this system, but can serve as a methodology and help other users to model their system equations as a quick approach that saves both computational costs and time. Furthermore, this allows a faster material selection process for this system and can inspire new materials to be used in situations where they were before discarded for their properties.

7.3.5 Temperature regression analysis – Equation Validation

The way researchers could utilise these equations would be to input the parameters of the relevant materials they wish to use for this tank design. This would allow an accurate calculation of the temperature at a point in time without needing to run a simulation, or the amount of heat absorbed per sphere for the particle size utilised in this thesis.

Which equation to use would depend mainly on the melting temperature of the PCM, since some equations are split between before and after phase change, but every equation is useful and should be utilised when calculating the results. This way, a range of temperatures and heat absorbed values would be available and the user can create the average plus/minus the error of what the expected result can be.

An example on how to utilise the aforementioned Equations 7.1 to 7.9 is to test them utilising parameters that have been reported in literature as opposed to user-defined ones, confirming the validity of these. The materials to be utilised in the test are the ones in methodology section 4.3 and results section 6; nOctadecane, Paraffin Wax and Capric Acid. However, since these materials do not reach phase change, Equations 7.8 and 7.9 will not be valid and are, therefore, excluded.

The material's results obtained using COMSOL Multiphysics found in Table 6.1 will be the values compared to when using Equation 7.1 and 7.2 for the heat absorption calculation.

Table 7.7: Tested heat absorption equations on previously analysed latent heat materials

	Tested Equations for Heat Absorption		
Material	**COMSOL Heat absorbed (J)**	**Equation 7.1 Heat absorbed (J)**	**Equation 7.2 Heat absorbed (J)**
Paraffin	1684.6463	2026.62	2071.38
nOctadecane	1834.9011	2444.7695	2401.2587
Capric Acid	1199.9412	2168.1067	1655.994742

These equations did not fit the previous results as accurately since they are meant to be for a latent heat system. Seeing as the materials did not phase change in the allocated simulation time, it is logical that the equation struggles to capture only the first sensible heating phase.

In terms of temperature, all materials are tested for temperature (at all times), for the corresponding Design A, for the centre sphere and for an HTF velocity of 0.01m/s. The same method as the one in section 7.1 is used. Results are presented in Tables 7.8 to 7.10:

Table 7.8: Tested equation results deviation for Paraffin Wax for all times (only for temperature as an output)

	Tested Equations for Paraffin Wax				
Deviation	**7.3**	**7.4**	**7.5**	**7.6**	**7.7**
RMS	5.71%	6.05%	2.56%	3.21%	3.22%
Minimum	-1.25%	-0.90%	-5.14%	-5.09%	-4.88%
Maximum	8.02%	8.41%	2.79%	4.08%	4.20%
Closest	0.00%	-0.01%	0.01%	-0.02%	-0.02%

Table 7.9: Tested equation results deviation for nOctadecane for all times (only for temperature as an output)

	Tested Equations for nOctadecane				
Deviation	**7.3**	**7.4**	**7.5**	**7.6**	**7.7**
RMS	5.45%	5.77%	2.68%	3.24%	3.23%
Minimum	-1.58%	-1.23%	-5.45%	-5.40%	-5.20%
Maximum	7.87%	8.27%	2.58%	3.95%	4.06%
Closest	-0.01%	0.00%	0.01%	-0.01%	-0.02%

Table 7.10: Tested equation results deviation for Capric Acid for all times (only for temperature as an output)

	Tested Equations for Capric Acid				
Deviation	**7.3**	**7.4**	**7.5**	**7.6**	**7.7**
RMS	8.48%	8.32%	11.02%	10.68%	10.57%
Minimum	-11.45%	-11.13%	-14.94%	-14.89%	-14.71%
Maximum	7.47%	7.86%	1.89%	3.62%	3.71%
Closest	0.02%	0.00%	-0.05%	0.08%	-0.03%

Looking at the tables, very good results are showcased. The percentages presented do not exceed 15% and are particularly accurate for nOctadecane, followed by Paraffin Wax. Although Capric Acid is not captured as precisely as the other two, the results are still considered valid and appropriate.

7.4 References for this section:

Shubham Agrawal. (2018). *P value and R squared*. RPubs. url: https://www.rpubs.com/shubh2565/pvalue-rsquared Accessed: 1st March 2021.

VIII. Conclusions

This thesis focused on materials and their suitability for TES, specifically for low grade applications. From sensible heat storage materials, to phase changing latent materials, to a more in depth analysis on user-defined materials, the goal was to assess their suitability by understanding how the thermal parameters affect the outputs in a quantitative analysis. The objectives set have been successfully achieved and the research question has been clearly answered. The overall key findings are summarised below.

8.1 Sensible Heat Storage

The sensible heat storage materials (Water, Glycerol, MDM and MD3M) were studied. Heating dynamics and heat absorption in a square tank (ratio 1/1) for low grade TES systems aimed for domestic usage were studied and three different tank designs were evaluated. The findings are:

- Changing the inlet design significantly affects the heating dynamics of the system, whereas changing the outlet only affects the results marginally and can be classified as negligible.
- Water, Glycerol, MDMA and MD3M as sensible heat materials with very different characteristics and properties will still perform approximately only 3% below or above the final temperature of the other materials in the tested time range of 40h in the current system design.

8.2 Latent Heat Storage

The latent heat storage materials (Paraffin wax, nOctadecane, Capric Acid) provided reliable information on their effectiveness as low grade materials in terms of heating dynamics and heat absorption per sphere for a square design tank (ratio 1/1) aimed for domestic usage. The findings are:

- The addition of a second inlet to the system yields higher final temperatures but this change was marginal, considering this unfavourable.
- A higher velocity at the inlet improves the heat transfer rate and allows higher temperatures and higher heat absorption, but the percentage differences are larger for design A (single inlet) than B (two inlets).
- The analysed materials proved to be suitable for low grade TES with favourable properties, with N-octadecane absorbing the most heat, capric acid charging fastest and paraffin being a good all round material.

8.3 Material Construction

The last study focused on “constructed” non-real materials and provide a valuable information on the influence of thermal properties on charging temperature and heat absorbed. There were a total of 28 user-defined materials. The findings are:

- There is a compromise between a fast charging time and high heat absorption per sphere; High density and latent heat are beneficial for maximum heat absorption but slow down charging time.
- Higher latent heat is a more influential parameter on the heat absorption per sphere, although practically the same effect can be achieved with a material with higher density.
- For the study’s low grade TES system, liquid parameters after phase change are more influential to the system than solid ones in terms of positive charging times and heating dynamics. In the material selection process, a material with high specific heat capacity of the solid and low specific heat capacity of the liquid benefits fast charging.
- Thermal parameters, such as melting temperature, thermal conductivity solid/liquid and specific heat capacity of the solid are not involved in the calculation of total heat absorption per sphere and are not featured in the fitted equations. The only property featured in the calculation of heat absorption is the specific heat capacity of the liquid.
- The fitted equations which allow for an accurate calculation of heat absorption per sphere and temperature during charging at any point in time will allow users to be able to effectively input thermal parameters of materials without having to run any simulations for this system design.
- Furthermore, the method of finding equations utilising a regression model with the thermal parameters for the system not only saves computational cost and time, but also allows users to find inspiration and follow the method to model their system equations as a quick approach to estimating the total heat absorbed or temperature of their system.

8.4 System Equations

The study focused on finding equations to express the relationship between the system researched and its materials. Equations were presented for results including the sensible heat analysis (Water, Glycerol, Engine Oil, Transformer Oil, MDM, MD2M, MD3M, n-Hexadecane and Acetic-Acid) and the material construction. The findings are:

- For the sensible heat materials, high R^2 value and accurate exponential growth fits can be approximated to understand the relationship between the final temperature and the coefficients.

- For the sensible heat materials, the fits were more accurate for the bottom spheres in terms of positions, and the one-dome configuration in terms of designs.
- For the material construction, the regression analysis focused on finding what the relationship between the outputs (heat absorbed and charging temperature) and the thermal parameters.
- High R^2 value fits were found for heat absorbed as an output, which consisted of linear equations featuring latent heat, density and specific heat capacity of the liquid.
- Deviations in the values are within acceptable ranges of less than 2.5%.
- Temperature as an output was more complex and equations were found for all the data set, yet also individually for before phase change only and after phase change only. The thermal parameters featured in the equations depended on the phase and fit. These were all linear, except for Equation 7.5.
- Deviations in the values are within decent ranges of less than 8.5% for one material through all times, and 12.5% for all material codes for a specific time.

8.5 Future Work

As future work, it would be interesting to look at the same system type using a different heat transfer fluid and operating temperature range. The current study focuses on water, yet it would be noteworthy to compare what the effect of another HTF is on the absorption, rate of charging and temperatures, and how it is these alter the equations.

Another proposal is to consider different tank sizes, still maintaining the original 1/1 ratio, or looking at a different tank aspect ratio all together. Although different inlet and outlet methods were tested, a larger or smaller tank with the same particle size capsules for the storage material would be interesting for an additional comparison. Furthermore, as mentioned in the literature review, other tank ratios appear frequently yet there is no record of this method being applied to identify what the influence of thermal parameters is. Exploring different ratios and comparing them to the current findings would be an attractive idea.